ELECTRON TEMPERATURE AND PRESSURE AT THE EDGE OF ASDEX UPGRADE PLASMAS

Estimation via electron cyclotron radiation and investigations on the effect of magnetic perturbations

Sylvia K. Rathgeber

SIGILL·UNIVERSITAT·LUDOVIC·MAXIM·

München 2013

ELECTRON TEMPERATURE AND PRESSURE AT THE EDGE OF ASDEX UPGRADE PLASMAS

Estimation via electron cyclotron radiation and investigations on the effect of magnetic perturbations

DISSERTATION
zur Erlangung des akademischen Grades
Doctor rerum naturalium

von
Sylvia K. Rathgeber
geboren in Erlangen

an der Fakultät für Physik
der Ludwig-Maximilians-Universität München

Abgabe der Arbeit:	28.02.2013
Mündliche Prüfung:	16.05.2013
Erstgutachter:	Prof. Dr. Hartmut Zohm
Zweitgutachter:	Prof. Dr. Gregor Morfill

Für Anne

Zusammenfassung

Verständnis und Kontrolle des Plasmarandverhaltens sind für den Erfolg von ITER und zukünftigen Fusionsanlagen unerlässlich. Dies erfordert die Verfügbarkeit geeigneter Methoden zur Bestimmung der Randparameter und zuverlässige Verfahren im Umgang mit verschiedenen Randphänomenen, z.B. zur Abschwächung von 'Edge Localized Modes' (ELMs) — einer möglicherweise schädlichen Plasmarand-Instabilität.

Die vorliegende Arbeit stellt eine neue Methode zur Bestimmung hochaufgelöster Randprofile der Elektronentemperatur mittels Vorwärtsmodellierung des Elektronen-Zyklotron-Strahlungstransportes vor und demonstriert deren erfolgreichen Einsatz, um die Wirkung magnetischer Störfelder zur ELM Mitigierung auf die kinetischen Randdaten zu untersuchen.

Für den Plasmakern von ASDEX Upgrade ist eine direkte und lineare Auswertung des gemessenen Elektronen-Zyklotron-Intensitätsspektrums basierend auf der Annahme eines optisch dichten Plasmas üblicherweise gerechtfertigt. Dagegen beruht eine verlässliche Auswertung des steilen und optisch dünnen Randbereiches auf der vollständigen Behandlung des Strahlungstransportes unter Berücksichtigung verbreiterter Emissions- und Absorptionsprofile. Dies wird mit Hilfe der integrierten Datenanalyse verwirklicht, die im Rahmen der Bayesschen Wahrscheinlichkeitstheorie eine gemeinsame Auswertung der Elektronendichte und -temperatur aus Daten unterschiedlicher unabhängiger und komplementärer Diagnostiken ermöglicht.

Die Methode offenbart, dass in Plasmen mit verbessertem Einschluss ('High-confinement modes' (H-moden)) der Randgradient der Elektronentemperatur den der Strahlungstemperatur um ein Vielfaches übersteigen kann. Außerdem erlaubt das Modell die Reproduktion des 'shine-through' Peaks — der Beobachtung erhöhter Strahlungstemperaturen für Frequenzen mit kalter Resonanz außerhalb des eingeschlossenen Plasmas. Dieses Phänomen wird von hochenergetischen Elektronen aus dem Randbereich von H-Moden mit stark frequenzverbreitertem Emissionsursprung verursacht und beinhaltet daher wertvolle Informationen über den Gradienten der Elektronentemperatur.

Dank der genauen Kenntnisse über die Randprofile und -gradienten der Elektronentemperatur und — unter Einbezug der Dichteinformation — des Elektronendrucks sind detailierte Untersuchungen von Plasmarand-Phänomenen wie den ELMs oder dem Übergang von der 'Low-confinement mode' (L-mode) zur H-mode möglich. Es wird gezeigt, wie sich die Anwendung nicht-axisymmetrischer magnetischer Störfelder auf die Randprofile von Elektronentemperatur, -dichte und -druck in H-Moden mit Typ-I und mitigierten ELMs und während des L-H Übergangs auswirkt.

Mitigierte ELMs treten verstärkt auf, wenn der Plasmarand gegenüber Typ-I ELM Regimes erhöhte Dichten und verringerte Temperaturen und Druckgradienten aufweist.

Dieser Parameterbereich kann durch starke Neutralgaszufuhr erreicht werden. Magnetische Störfelder fördern die ELM Mitigierung möglicherweise, indem sie den Schwellwert zwischen Typ-I und kleinen ELMs zu etwas höheren Randtemperaturen verschieben.

Die Anwendung der Störspulen in L-Moden bewirkt eine Absenkung des Druckgradienten aufgrund eines zunehmenden Wärmetransportes. Am L-H Übergang scheinen der Druckgradient und die Verscherung des radialen elektrischen Feldes mit und ohne Störspulen den gleichen Wert aufzuweisen, während die dafür notwendige Heizleistung in Gegenwart des Störfeldes erhöht ist.

Abstract

Understanding and control of the plasma edge behaviour are essential for the success of ITER and future fusion plants. This requires the availability of suitable methods for assessing the edge parameters and reliable techniques to handle edge phenomena, e.g. to mitigate ‘Edge Localized Modes’ (ELMs) — a potentially harmful plasma edge instability.

This thesis introduces a new method for the estimation of accurate edge electron temperature profiles by forward modelling of the electron cyclotron radiation transport and demonstrates its successful application to investigate the impact of Magnetic Perturbation (MP) fields used for ELM mitigation on the edge kinetic data.

While for ASDEX Upgrade bulk plasmas, straightforward analysis of the measured electron cyclotron intensity spectrum based on the optically thick plasma approximation is usually justified, reasonable analysis of the steep and optically thin edge region relies on full treatment of the radiation transport considering broadened emission and absorption profiles. This is realized in the framework of integrated data analysis which applies Bayesian probability theory for joint analysis of the electron density and temperature with data of different independent and complementary diagnostics.

The method reveals that in regimes with improved confinement (‘High-confinement modes’ (H-modes)) the edge gradient of the electron temperature can be several times higher than that of the radiation temperature. Furthermore, the model is able to reproduce the ‘shine-through’ peak — the observation of increased radiation temperatures at frequencies with cold resonance outside the confined plasma region. This phenomenon is caused by strongly down-shifted radiation of Maxwellian tail electrons located in the H-mode edge region and, therefore, contains valuable information about the electron temperature edge gradient.

The accurate knowledge about the edge profiles and gradients of the electron temperature and — including the density information — the electron pressure allows a detailed study of plasma edge phenomena like ELMs or the transition from ‘Low-confinement mode’ (L-mode) to H-mode. It is shown how the application of non-axisymmetric MP fields acts on the edge profiles of electron temperature, density and pressure in H-modes with type-I and mitigated ELMs and during the L-H transition.

Compared to type-I ELMs, mitigated ELMs tend to occur at higher edge densities, lower edge temperatures and reduced edge pressure gradients. This parameter regime can be achieved by strong gas fuelling. MP fields might support ELM mitigation by shifting the threshold between type-I and small ELMs towards slightly higher edge temperatures.

The application of MPs in L-modes results in a degradation of the pressure gradient due to increased heat transport. At the L-H transition, the pressure gradient and the radial electric field shearing seem to exhibit the same value with and without MPs, while its required heating power is increased in the presence of MPs.

Publication list

Journal publications as first author

Rathgeber S K, Barrera L, Eich T, Fischer R, Nold B, Suttrop W, Willensdorfer M, Wolfrum E and the ASDEX Upgrade Team 2013 **Estimation of edge electron temperature profiles via forward modelling of the electron cyclotron radiation transport at ASDEX Upgrade** *Plasma Physics and Controlled Fusion* **55** (2) 025004 (15pp) doi:10.1088/0741-3335/55/2/025004

Rathgeber S K, Fischer R, Fietz S, Hobirk J, Kallenbach A, Meister H, Pütterich T, Ryter F, Tardini G, Wolfrum E and the ASDEX Upgrade Team 2010 **Estimation of profiles of the effective ion charge at ASDEX Upgrade with Integrated Data Analysis** *Plasma Physics and Controlled Fusion* **52** (9) 095008 (16pp) doi:10.1088/0741-3335/52/9/095008

Journal publications as co-author

Fischer R, Fuchs J C, McDermott R, Rathgeber S K, Suttrop W, Willensdorfer M, Wolfrum E and the ASDEX Upgrade Team 2012 **Spatiotemporal response of plasma edge density and temperature to non-axisymmetric magnetic perturbations at ASDEX Upgrade** *Plasma Physics and Controlled Fusion* **54** (11) 115008 (12pp) doi:10.1088/0741-3335/54/11/115008

Kallenbach A, Dux R, Fuchs J C, Fischer R, Geiger B, Giannone L, Herrmann A, Lunt T, Mertens V, McDermott R, Neu R, Pütterich T, Rathgeber S K, Rohde V, Schmid K, Schweinzer J, Teutterer W and the ASDEX Upgrade Team 2010 **Divertor power load feedback with nitrogen seeding in ASDEX Upgrade** *Plasma Physics and Controlled Fusion* **52** (5) 055002 (17pp) doi:10.1088/0741-3335/52/5/055002

Lunt T, Feng Y, Bernert M, Herrmann A, de Marné P, McDermott R, Müller H W, Potzel S, Pütterich T, Rathgeber S K, Suttrop W, Viezzer E, Wolfrum E, Willensdorfer M and the ASDEX Upgrade Team 2011 **First EMC3-Eirene simulations of the edge magnetic perturbations at ASDEX Upgrade compared to the experiment** *Nuclear Fusion* **52** (5) 054013 (7pp) doi:10.1088/0029-5515/52/5/054013

Ryter F, Rathgeber S K, Barrera L, Bernert M, Conway G D, Fischer R, Happel T, Kurzan B, McDermott R M, Suttrop W, Viezzer E, Willensdorfer W and the ASDEX Upgrade Team **Survey of the H-mode power threshold and transition physics studies in ASDEX Upgrade** submitted to *Nuclear Fusion*

Ryter F, Rathgeber S K, Viezzer E, Suttrop W, Burckhart A, Fischer R, Kurzan B, Potzel S, Pütterich T and the ASDEX Upgrade Team 2012 **L-H transition in the presence of magnetic perturbations in ASDEX Upgrade** *Nuclear Fusion* **52** (11) 114014 (7pp) doi:10.1088/0029-5515/52/11/114014

Sauter P, Pütterich T, Ryter F, Viezzer E, Wolfrum E, Conway G, Fischer R, Kurzan B, McDermott R, Rathgeber S K and the ASDEX Upgrade Team 2012 **L- to H-Mode transitions at low density in ASDEX Upgrade** *Nuclear Fusion* **52** (1) 012001 (5pp) doi: 10.1088/0029-5515/52/1/012001

Schweinzer J, Sips A C C, Tardini G, Schneider P A, Fischer R, Fuchs J C, Gruber O, Hobirk J, Kallenbach A, McDermott R M, Neu R, Pütterich T, Rathgeber S K, Stober J, Vincente J and the ASDEX Upgrade Team 2011 **Confinement of "Improved H-modes" in the All-Tungsten ASDEX Upgrade** *Nuclear Fusion* **51** (11) 113003 (7pp) doi: 10.1088/0029-5515/51/11/113003

Suttrop W, Barrera L, Herrmann A, McDermott R M, Eich T, Fischer R, Kurzan B, Lang P T, Mlynek A, Pütterich T, Rathgeber S K, Rott M, Vierle T, Viezzer E, Willensdorfer M, Wolfrum E, Zammuto I and the ASDEX Upgrade Team 2011 **Studies of ELM-mitigation with new in-vessel saddle coils at ASDEX Upgrade** *Plasma Physics and Controlled Fusion* **53** (12) 124014 (8pp) doi:10.1088/0741-3335/53/12/124014

Tardini G, Fischer R, Jenko F, Kallenbach A, McDermott R, Pütterich T, Rathgeber S K, Schneller M, Schweinzer J, Sips A C C, Told D, Wolfrum E and the ASDEX Upgrade Team 2013 **Core transport analysis of nitrogen seeded H-mode discharges in ASDEX Upgrade** *Plasma Physics and Controlled Fusion* **55** (1) 015010 (6pp) doi:10.1088/0741-3335/55/1/015010

Willensdorfer M, Wolfrum E, Scarabosio A, Aumayr F, Fischer R, Kurzan B, McDermott R M, Mlynek A, Nold B, Rathgeber S K, Rohde V, Ryter F, Sauter P, Viezzer E and the ASDEX Upgrade Team 2012 **Electron density formation after L-H transitions and the L-H/H-L cycle in ASDEX Upgrade** *Nuclear Fusion* **52** (11) 114026 (10pp) doi:10.1088/0029-5515/52/11/114026

Wolfrum E, Sauter P, Willensdorfer M, Ryter F, Aumayr F, Barrera Orte L, Burckhart A, Fable E, Fischer R, Kurzan B, Pütterich T, Rathgeber S K, Suttrop W, Viezzer E and the ASDEX Upgrade Team 2012 **Recent progress in understanding the L-H transition physics from ASDEX Upgrade** *Plasma Physics and Controlled Fusion* **54** (12) 124002 (6pp) doi:10.1088/0741-3335/54/12/124002

Conference contributions as first author

Rathgeber S K, Barrera L, Fischer R, Suttrop W, Willensdorfer M, Wolfrum E and the ASDEX Upgrade Team 2012 **Investigations on kinetic edge profiles of magnetically perturbed ASDEX Upgrade plasmas** In *39th EPS Conference on Plasma Physics (Stockholm, Sweden)* **36F** P5.059

Conference contributions as co-author

Burckhart A, Dunne M, Wolfrum E, Fischer R, Rathgeber S K and the ASDEX Upgrade Team 2012 **Effect of experimental uncertainties on the calculation of the peeling-ballooning instability boundary** In *38th EPS Conference on Plasma Physics (Stockholm, Sweden)* **36F** P2.006

Fischer R, Fuchs C J, Kurzan B, McDermott R M, Pütterich T, Rathgeber S K, Suttrop W, Viezzer E, Willensdorfer M and the ASDEX Upgrade Team 2011 **Effect of non-axisymmetric magnetic perturbations on profiles at ASDEX Upgrade** In *38th EPS Conference on Plasma Physics (Strasbourg, France)* **35G** P1.072

Fischer R, Rathgeber S K, Fietz S, Hobirk J, Kallenbach A, Meister H, Pütterich T, Ryter F, Tardini G, Wolfrum E, Zohm H and the ASDEX Upgrade Team 2010 **Effective ion charge Zeff from integrated data analysis of multiple diagnostics at ASDEX Upgrade** In *37th EPS Conference on Plasma Physics (Dublin, Ireland)* **34** A P5.107

Hobirk J, Challis C D, Fischer R, Fuchs J C, Gude A, Joffrin E, Kallenbach A, Kurzan B, Maraschek M, McDermott R, Rathgeber S K, Schweinzer J, Stober J K, Tardini G, the ASDEX Upgrade Team and JET EFDA contributors 2011 **Comparison of different improved H-mode scenarios on ASDEX Upgrade and JET** In *38th EPS Conference on Plasma Physics (Strasbourg, France)* **35G** O5.129

Ryter F, Sauter P, Suttrop W, Viezzer E, Willensdorfer M, Wolfrum E, Bernert M, Conway G D, Fischer R, da Graca S, Kurzan B, McDermott R M, Potzel S, Pütterich T, Rathgeber S K, Vicente J and the ASDEX Upgrade Team **L-H transition, pedestal development and I-mode studies at ASDEX Upgrade** submitted to *24th IAEA Fusion Energy Conference (San Diego, California)*

Ryter F, McDermott R M, Pütterich T, Vicente J, Viezzer E, Wolfrum E, Angioni C, Bernert M, Boom J C, Fischer R, Geiger B, da Graca S, Kurzan B, Luhmann Jr N C, Park H K, Rathgeber S K, Sauter P, Willensdorfer M and the ASDEX Upgrade Team 2011 **I-Mode studies at ASDEX Upgrade** In *38th EPS Conference on Plasma Physics (Strasbourg, France)* **35G** P5.112

Schweinzer J, Sips A C C, Kallenbach A, Gruber O, Fischer R, Fuchs J C, Hobirk J, Jenko F, McDermott R M, Neu R, Pütterich T, Rathgeber S K, Schneller M, Stober J, Tardini G, Told D and the ASDEX Upgrade Team 2010 **Confinement of "Improved H-modes" in the All-Tungsten ASDEX Upgrade** In *23rd IAEA Fusion Energy conference (Daejon, Rep. of Korea)* **IAEA-CN-180** EXC/P2-07

Suttrop W, Barrera Orte L, Eich T, Fischer R, Fuchs J C, Kocan M, Lunt T, McDermott R, Müller H-W, Pütterich T, Rathgeber S K, Rott M, Ryter F, Vierle Th, Viezzer E, Wolfrum E and the ASDEX Upgrade Team **Mitigation of Edge Localised Modes with small non-axisymmetric magnetic perturbations in ASDEX Upgrade** submitted to *24th IAEA Fusion Energy Conference (San Diego, California)*

Suttrop W, Barrera Orte L, Fischer R, Fuchs J C, McDermott R, Müller H W, Pütterich T, Rathgeber S K, Viezzer E, Wolfrum E and the ASDEX Upgrade Team 2012 **Access conditions for ELM mitigation with non-axisymmetric magnetic perturbations in ASDEX Upgrade** In *39th EPS Conference on Plasma Physics (Stockholm, Sweden)* **36F** P2.092

Tardini G, Jenko F, McDermott R M, Pütterich T, Rathgeber S K, Schneller M, Schweinzer J, Told D and the ASDEX Upgrade Team 2010 **Core transport and pedestal characteristics of nitrogen seeded H-mode discharges in ASDEX Upgrade** In *37th EPS Conference on Plasma Physics (Dublin, Ireland)* **34A** P1.1097

Tardini G, Fischer R, Igochine V, Kallenbach A, Maggi C F, Neu R, Pütterich T, Rathgeber S K, Schweinzer J and the ASDEX Upgrade Team 2009 **Confinement enhancement in ASDEX Upgrade improved H-mode discharges with nitrogen seeding** In *36th EPS Conference on Plasma Physics (Sofia, Bulgaria)* **33E** O2.004

Willensdorfer M, Wolfrum E, Fable E, Ryter F, Aumayr F, Fischer R, Rathgeber S K, Sauter P, Schneider P A, Sieglin B and the ASDEX Upgrade Team 2012 **Transport analysis of the density build-up after L-H transition in ASDEX Upgrade** In *39th EPS Conference on Plasma Physics (Stockholm, Sweden)* **36F** P1.023

Contents

1 Introduction

1.1 The goal: Fusion as energy source

Although it has not yet penetrated widespread public consciousness nor evoked remarkable economical interest, fusion is an important component in long-term energy scenarios [1]. The ambition of a worldwide limitation of CO_2 emission to prevent further climate changes and of an energy supply excluding nuclear fission reactors due to safety and waste issues requires extensive development of new technologies [2]. The current expansion of solar and wind power plants is a promising step towards 'green' energy. However, their natural restriction to weather conditions calls for further concepts regarding energy storage systems, smart electricity grids as well as an additional source of sustainable energy that is capable of supplying the base load [3].

For the latter, fusion proves to be an ideal candidate. With the release of 17.6 MeV during each fusion reaction of the hydrogen isotopes deuterium and tritium to helium and a neutron (cf. Fig. 1.1), it represents a very efficient source of energy; the deuterium stored in one tub of water and the tritium extracted from the lithium of one laptop battery are enough to satisfy the energy consumption of a whole family for 50 years [4]. Thanks to the small amount of fuel present in the reactor — excluding the risk of an uncontrolled chain reaction —, the short lifetime of the involved radioactive elements and the CO_2 emission-free production, fusion energy is likely to meet the future demands for safety and environmental acceptability. Furthermore, the reservoir of the fuel, sea water for deuterium and the lithium in sea water and stones for tritium extraction, is almost endless and widely available. This spares mankind wars for natural resources and enables worldwide energy supply independent of the political or social situation in single countries.

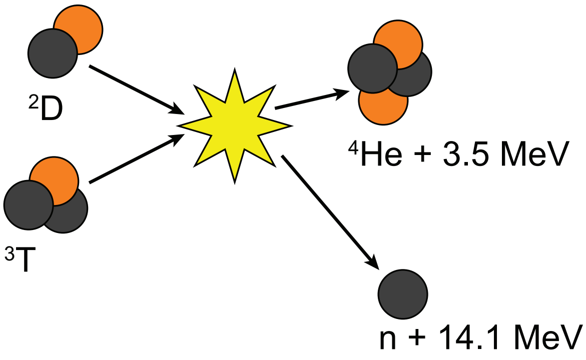

Figure 1.1: Schematic of the fusion reaction.

However, the construction of commercial fusion power plants will not be possible within the first half of this decade because the technical realization of such a reactor is very challenging and fusion research is still facing many open questions. To enable them to fuse, the hydrogen nuclei have to be highly energetic in order to overcome their Coulomb barrier. For a positive energy balance, the fuel has to be in the plasma state which allows the particles to collide several times without losing their energy before the actual fusion collision happens.

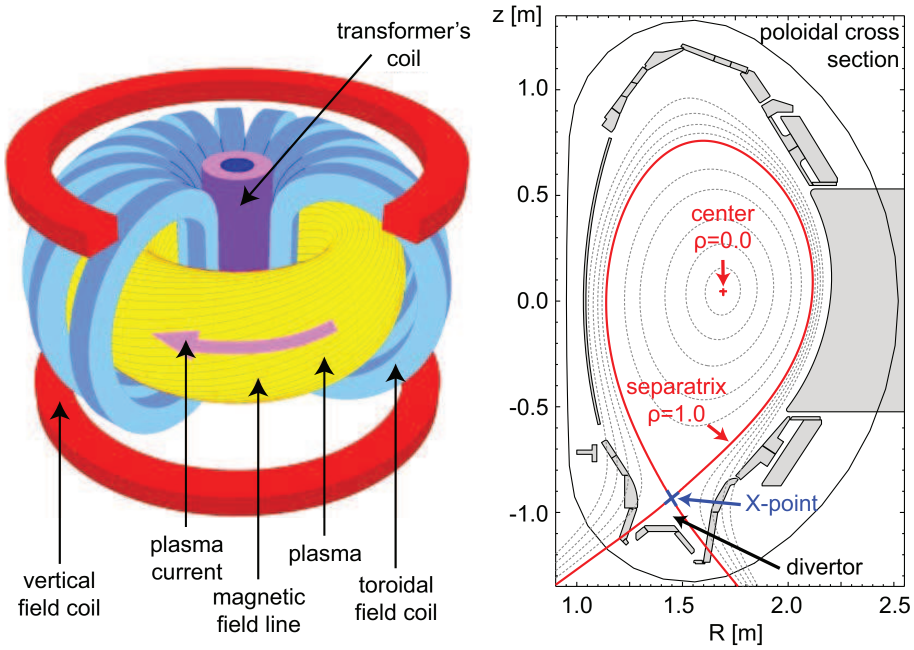

Figure 1.2: Left: Schematic of a tokamak. Right: Poloidal cross section of the ASDEX Upgrade torus with divertor and flux surfaces.

1.2 The concept: Tokamak in high-confinement mode

Such a fusion plasma has to exhibit a temperature of $T \geq 10\,\mathrm{keV} \mathrel{\widehat{=}} 116$ Mio.°C to achieve a sufficiently high fusion rate [5]. This constitutes the major difficulty to handle the plasma: its confinement. There are two concepts according to which the plasma is either confined by its own inertia or by a magnetic field. In a magnetically confined plasma, the charged particles are guided by helically wound magnetic field lines forming a torus-shaped plasma volume. The method of producing the helical magnetic structure distinguishes between the stellarator, which creates both the toroidal and poloidal magnetic components by external coils, and the tokamak.

In tokamaks like ASDEX Upgrade (cf. appendix A) and ITER (Latin: 'the way') — which is currently being built to demonstrate the efficiency of fusion — the toroidal magnetic field component is created by several identical toroidal coils (blue on left-hand side of Fig. 1.2) situated around the torus while the poloidal field is generated via the induction of a toroidal plasma current (purple arrow) [5]. The vertical field coils (red) serve for the elongated plasma geometry and the control of the vertical plasma position.

Additional magnetic coils at the bottom are used to deflect the outer field lines into the so-called 'divertor' [6] as can be seen on the right-hand side of Fig. 1.2. The resulting formation of an X-point (blue) — in toroidal view: an X-line — enables to keep the hottest part of the plasma within the last closed flux surface ('separatrix', red line) and away from the vessel walls. With this configuration it is possible to get access to the 'High-confinement mode' (H-mode) [7].

The H-mode is characterized by an increased energy content ($W \propto \int p \mathrm{d}V$) due to a higher plasma pressure p (red solid line in Fig. 1.3) in the whole plasma volume V compared to the 'Low-confinement mode' (L-mode, blue dashed line). This is enabled by the formation of an Edge Transport Barrier (ETB, grey shaded area) which allows higher pressure gradients at the very edge of the plasma [8]. Apart from that region, the H-mode pressure profile exhibits a similar shape like in L-mode [9], but sits on a so-called 'pedestal'. This demonstrates the importance of the edge physics for the overall plasma performance.

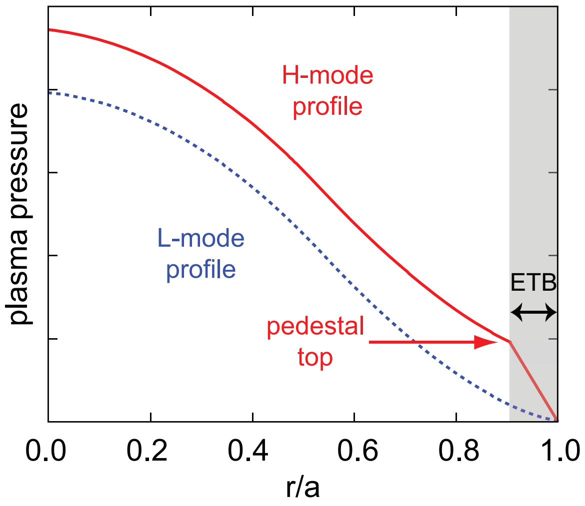

Figure 1.3: Comparison of L- and H-mode pressure profiles.

1.3 The challenge: Understanding and control of the H-mode edge plasma

At present day machines reliable concepts for discharges to enter the H-mode regime have been developed. Nevertheless, the trigger mechanism for the transition from L- to H-mode is not yet completely understood which poses a remaining uncertainty for the accessibility to H-mode in ITER and future fusion plants.

Besides the L-H transition, a very important edge phenomenon is the occurrence of Edge Localized Modes (ELMs) [10] that usually accompany H-mode plasmas and still demand for a complete theoretical description as well as a reliable method to keep them at a tolerable level.

These MagnetoHydroDynamic (MHD) instabilities — supposedly driven by large edge pressure gradients and current densities [11] — frequently expel particles and energy from the plasma edge. The energy exhaust during the most common ELMs of type-I can account for $\sim 10\,\%$ of the whole plasma stored energy. In a large device like ITER and future power plants, the peak heat flux during such a type-I ELM event is likely to cause material erosion of the divertor target plates and first wall components [12, 13]. To avoid unacceptable machine damage and to reduce the plasma contamination with impurities, methods for ELM suppression or mitigation are necessary. On the other hand, ELMs keep the plasma 'clean' by flushing out impurity ions. This enables a higher fusion rate because of less dilution and a stationary H-mode due to lower power losses by radiation [10]. Therefore, a regime with frequent small ELMs or without ELMs but sufficient outward particle transport would be favourable for future reactors.

The application of non-axisymmetric Magnetic Perturbation (MP) fields at the plasma edge by external coils depicts a promising technique to achieve stable H-mode plasmas without or with small ELMs and confinement properties that are comparable to those of type-I ELMy H-modes [14, 15, 16, 17]. However, there is no common theoretical explanation for the effect of MPs on the plasma which is consistent with all the results from the different machines. To improve the understanding of the underlying mechanism in order to assess the possibility of ELM mitigation with MPs at ITER, detailed analysis about their effect on plasmas under diverse conditions is necessary.

Since ELMs are assumed to be driven by large edge pressure gradients, variations in the H-mode edge kinetic data might be relevant for ELM mitigation. Furthermore, the effect of MPs on the L-H transition — which is also related to the edge kinetic parameters — is of great interest, as MPs have been observed to increase the threshold power for the L-H transition [18, 19, 20, 21]. This is important for ITER which is going to be operated close to the L-H power threshold and must ensure the accessibility to H-mode also in the presence of MPs.

Hence, analysis of the edge kinetic data might support to understand and predict the impact of MPs on the plasma. Suitable diagnostics for this study are Electron Cyclotron Emission (ECE) [22] measurements for the reconstruction of electron temperature profiles and LIthium Beam emission spectroscopy (LIB) [23] for the density evaluation. Furthermore, a valuable analysis tool is provided by Integrated Data Analysis (IDA) [24] of different diagnostics for simultaneous evaluation of electron density and temperature and, therefore, also pressure in the framework of Bayesian probability theory.

However, commonly applied IDA is lacking a reliable interpretation of the ECE data in the edge gradient region. It contains the conventional simplification of identifying the electron temperature with the radiation temperature at the cold resonance position of the measured frequency. The underlying assumptions of localized emission and of radiation intensity at black-body level are reasonable in the optically thick core plasma. At the edge, a region of optically thin plasma and steep gradients, they are no longer valid [22, 25]. This is manifested e.g. in the occurrence of the ‘shine-through’ peak of enhanced radiation temperatures with cold resonance in the Scrape-Off Layer (SOL) [26, 27, 28].

1.4 Motivation: Estimation of edge electron temperature and pressure and their response to magnetic perturbations

The objective of this work was to develop a method for a valid interpretation of the edge ECE data to obtain reliable edge electron temperature profiles and gradients and to apply this method to a detailed investigation of the effect of MPs on the electron edge kinetic parameters in ELMy H-modes and at the L-H transition.

Instead of the conventional straight-forward analysis of the ECE data, the new method considers the whole broadened electron cyclotron emission and absorption profiles depending on electron temperature and density and solves the radiation transport equation along the measurement lines of sight through the entire plasma. This is done by forward modelling in the framework of IDA.

The presented approach allows to describe the complex interplay between electron and radiation temperature depending on the optical depth and the gradient length — including the long time unresolved 'shine-through' phenomenon — and to exploit the full information of the ECE data up to the near SOL for a reliable estimation of edge electron temperatures and gradients. For H-mode plasmas, it reveals steeper gradients than conventional IDA. This finding demonstrates the importance of applying a sophisticated model for plasma edge studies based on ECE data.

These reliable and accurate results enable a thorough investigation on edge electron temperature and pressure of discharges with MPs. It is tested whether the results of ASDEX Upgrade show a degradation of the edge pressure gradient with MPs caused by an increased diffusive transport due to field line ergodization [16] ("hypothesis ELM-I") or by an additional particle source cooling the edge [29] ("hypothesis ELM-II") which could explain ELM mitigation by stabilizing the peeling-ballooning mode or whether MPs prevent the plasma from reaching the ballooning limit by clamping the pressure gradient to another stability boundary with lower threshold [30, 31] ("hypothesis ELM-III").

Regarding the effect of MPs on the L-H transition, it is checked whether the heating power needed to trigger the L-H transition is higher because application of MPs flattens the edge pressure gradient — and reduces the radial electric field shearing — via ergodization ("hypothesis LH").

The thesis consists of one 'theoretical' and one methodical chapter, followed by two result chapters and ends with a summary and outlook. The theoretical chapter gives an overview on current knowledge about the L-H transition (section 2.1) and ELMs (section 2.2) and how both these phenomena are affected by the application of MPs. The methodical chapter starts with an introduction on established background information about ECE physics, diagnostic means and IDA (sections 3.1 – 3.3) and continues with a detailed description of the implementation, results, sensitivity, limitations and the validation of the new forward modelling tool. The results part is divided in the examination of the edge kinetic data during ELMy H-modes (chapter 4) and the L-H transition (chapter 5) in the presence of MPs.

2 H-mode characteristics and the effect of magnetic perturbations

This chapter provides the necessary background information about the L-H transition (section 2.1), Edge Localized Modes (ELMs) (section 2.2) and the effect of Magnetic Perturbations (MPs) on both phenomena.

The two sections are structured in the same way. First, some basic information and observations about the respective phenomenon are given and the most popular model to explain its existence is briefly pointed out. This is each followed by a description of the impact of MPs on the event and hitherto existing ideas to explain these effects on the basis of the prementioned models.

2.1 The L-H transition

2.1.1 Phenomenology of the L-H transition

In 1982, it has been discovered at the ASDEX tokamak [7] that strong heating (cf. Fig. 2.1 (a)) enables the plasma to enter a regime with improved confinement. This is induced by the formation of an Edge Transport Barrier (ETB) with reduced energy and particle transport due to a lower level of turbulence [32].

As already indicated in section 1.2, easiest access to the H-mode regime has been found in tokamaks with divertor configuration. Furthermore, it seems that a minimum heating power [33] depending on the electron density, the magnetic field strength and the machine size is necessary to enable the transition to H-mode. This threshold power is thereby given in terms of the net thermal loss power crossing the separatrix [34]:

$$P_{\mathrm{LOSS}} = P_{\mathrm{heat}} - \frac{\mathrm{d}W_{\mathrm{MHD}}}{\mathrm{d}t}, \tag{2.1}$$

which expresses the difference between the total heating power deposited in the plasma and the time derivative of the plasma stored energy W_{MHD}. Sometimes, also the radiation losses from the bulk plasma are considered, leading to the 'conducted' power through the separatrix ($P_{\mathrm{Sep}} = P_{\mathrm{LOSS}} - P_{\mathrm{rad}}^{\mathrm{bulk}}$) [35].

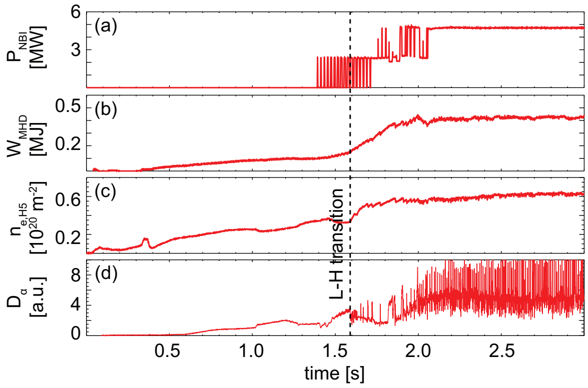

Figure 2.1: Typical time traces of (a) the heating power, (b) the plasma stored energy, (c) the line-integrated edge density and (d) the D_α radiation in L- and H-mode; the transition time is indicated by the vertical dashed line.

The transition from L- to H-mode (vertical dashed line in Fig. 2.1) is, by nature, characterized by an increased energy and particle content confined in the plasma. This is illustrated by the sudden enhancement of the plasma stored energy (b) and the line-integrated edge density $n_{\mathrm{e,H5}}$ (c). The latter is given by the 'H5' channel (whose position is depicted in Fig. 3.3) of the interferometry measurement which is briefly described in appendix A.

The confinement improvement is enabled by strongly steepened edge gradients of density, temperature and, therefore, also the pressure (cf. Fig. 1.3). As a consequence of the steep edge kinetic profiles, also the radial electric field E_{r} exhibits a strong variation at the edge. It can be derived from the radial force balance for each species α [36]:

$$E_{\mathrm{r}} = \underbrace{\frac{\nabla p_\alpha}{n_\alpha Z_\alpha \mathrm{e}}}_{\text{diamagnetic contribution}} \quad \underbrace{-v_{\Theta,\alpha} B_\Phi + v_{\Phi,\alpha} B_\Theta}_{\text{Lorentz contribution}} \tag{2.2}$$

with charge state Z, toroidal and poloidal velocities v_Φ and v_Θ and toroidal and poloidal magnetic field components B_Φ and B_Θ. The radial electric field is driven by the main ions and at the plasma edge — due to the steep gradients and the small rotation — dominated by the first (diamagnetic) term as demonstrated experimentally [37, 38]. The edge ion density and pressure gradients cause a radial electric field well close to the separatrix which is much deeper in H- than in L-mode. Measurements at ASDEX Upgrade indicate that the minimum of this well exhibits a discharge parameter independent value of about $-15\,\mathrm{kVm^{-1}}$ at the L-H transition [39].

Another observation linked to the L-H transition is a reduced level of turbulence at the plasma edge that is seen e.g. in density fluctuation measurements with reflectometry [8]. The suppression of turbulence gives rise to a decreased energy and particle transport across the ETB [8] and, therefore, also to a transiently reduced energy flux into the SOL. This is reflected in the drop in the D_α radiation (cf. Fig. 2.1 (d)) which is typically used to identify the L-H transition time [32].

2.1.2 Model for the L-H transition

In most cases turbulent transport is connected with a poloidally fluctuating electric potential. The associated fluctuating poloidal electric field causes radial plasma flows which take the form of eddies with a poloidal wavelength dictated by that of the potential fluctuation.

As indicated in the schematic in Fig. 2.2, the eddies (black circles) are unperturbed if the background poloidal flow (gyrocentre $\vec{E} \times \vec{B}$ drift, red arrows) exhibits a constant velocity (a) due to a constant radial electric field (blue line) over r. A main cause for the reduction of turbulent transport can be the existence of a shear (radial gradient) in the radial electric field. This causes a variation in the poloidal drift — which is largest

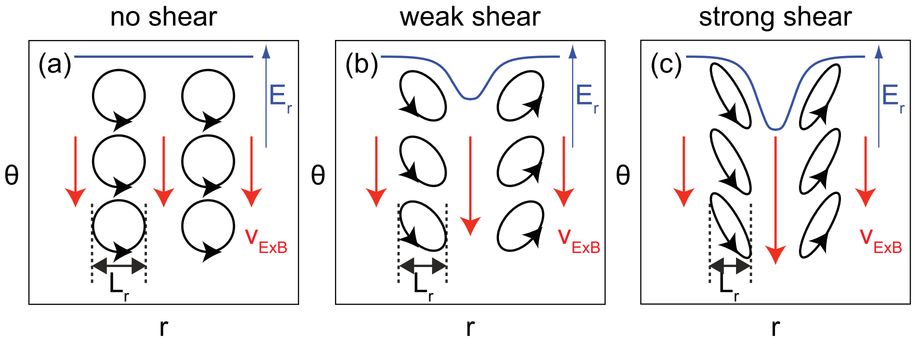

Figure 2.2: Schematic for turbulence suppression by a sheared radial electric field.

at the location of the minimum in the radial electric field profile — and a shearing of the eddies (b) and (c). If the shearing rate becomes faster than the growth rate (in the linear picture) or the lifetime (in the non-linear picture) of the eddies, fluctuations on neighbouring flux surfaces become de-correlated, i.e. the correlation length L_r decreases, and radial flows are reduced [40, 41].

Although the model for the sustainment of the H-mode by turbulence de-correlation via sheared $\vec{E} \times \vec{B}$ flows is widely accepted, it might not be able to explain the triggering of the L-H transition because the latter happens on the turbulence time scale ($\sim \mu$s) while the development of the pressure gradient occurs on a millisecond time scale.

Measurements and theory indicate that the turbulence itself increases the shearing of the background flow by transferring energy from the eddies to large-scale poloidal flows contributing to the background flow — the zonal flows [42, 43]. Due to the toroidal curvature, the zonal flows are compressed at the high field side and reflected which might cause coherent zonal flow oscillations, called Geodesic Acoustic Modes (GAMs) [44]. Once triggered — at a sufficiently high level of turbulence caused by strong heating — these zonal flows or GAMs lower the level of turbulence, which in turn reduces the zonal flows or GAMs. Hence, a predator-prey like behaviour occurs, with inversely phased oscillations in the levels of turbulence and zonal flows or GAMs. During the low-turbulence phases, the edge kinetic gradients steadily increase as long as the mean flow shear itself is strong enough to suppress the turbulence and to sustain the H-mode. This model is still under investigation.

2.1.3 Observations about the dependence of the L-H power threshold on magnetic perturbations

The application of MPs for ELM mitigation can also effect the L-H transition. Experiments from MAST [18], DIII-D [19], NSTX [20] and ASDEX Upgrade [21] demonstrate that the threshold power needed to trigger the L-H transition can rise with MPs.

According to experiments at ASDEX Upgrade with — mostly non-resonant — MPs (cf. appendix B for the coil setup and field configuration), the effect of MPs on the

L-H transition depends on the density [21]. At line-averaged densities below 45 % of the Greenwald density [45], the L-H transition and its required threshold power are not influenced, while applying MPs at line-averaged densities higher than 65 % of the Greenwald density, completely prevents the transition to H-mode — even with twice the heating power that is needed without MPs. At intermediate densities, the L-H transition is delayed by the MPs — compared to an otherwise identical discharge — and occurs at up to 20 % higher power, but at a similar density. These experiments also demonstrate the possibility to sustain H-modes without a single type-I ELM and comparable confinement properties.

From other machines, no density dependence for the impact of MPs on the L-H transition has been reported. At MAST [18], the necessary conditions to affect the L-H transition are a sufficiently high MP-coil current and a large resonant component. In these cases the heating power required for the L-H transition is increased by at least 30 %. The kinetic edge profiles before the L-H transition are unchanged, but the Lorentz component (cf. (2.2)) of the radial electric field is increased. Like at MAST, the L-H power threshold in DIII-D discharges is significantly higher with MP-coil currents above a certain value. However, at DIII-D [19] the L-H power threshold also slightly increases with non-resonant MPs. An experiment at NSTX [20] with a strongly non-resonant MP-field configuration required an L-H transition power that was 65 % higher than without MPs.

There is no general explanation for the impact of MPs on the L-H power threshold. However, since ITER is going to be operated close to its predicted power threshold, investigation of this effect is important to assure the accessibility to H-mode in ITER also with MPs.

2.1.4 Hypothesis for the increase of the L-H power threshold due to magnetic perturbations

As already discussed, the key player for sustaining the H-mode is supposed to be the shearing of the radial electric field. Consequently, considerations on how the L-H power threshold can be affected by MPs are focused on their influence on the radial electric field. Investigation of the Lorentz component of the radial electric field has not been a subject of this thesis. Yet, with the study of the edge kinetic parameters — and the related diamagnetic radial electric field component — the following hypothesis is tested:

"Hypothesis LH": Reduction of the diamagnetic radial electric field shearing via field line ergodization In general, a resonant (field aligned) magnetic perturbation produces magnetic islands at each resonant magnetic surface, with $q = m/n$, where q is the safety factor at this surface which denotes the number of toroidal turns for one poloidal turn of the field lines and m and n are the poloidal and toroidal mode numbers of the perturbation field. If resonant surfaces with different q are close to each other and the perturbation field induced magnetic islands overlap, magnetic field lines in between these surfaces begin to make uncorrelated radial excursions. In this state of field line ergodization [46], magnetic surfaces no longer exist. This causes enhanced diffusive transport. A measure for the transport level is given by the heat diffusivity χ. With the assumption of equal electron and ion density and temperature the effective heat diffusivity $\chi_{\text{eff}} = (\chi_{\text{e}} + \chi_{\text{i}})/2$ [47] is calculated from the total power through the separatrix surface A_{sep}:

$$\frac{P_{\text{LOSS}}}{2A_{\text{sep}}} = \frac{1}{2}\left(q_{\text{e}} + q_{\text{i}}\right) \approx -\chi_{\text{eff}} n_{\text{e}} \nabla T_{\text{e}}, \tag{2.3}$$

independent of the ratio of electron and ion heat flux q.

Field line ergodization and the consequent increase of radial transport might reduce the edge pressure gradient and via (2.2) also the radial electric field. If this effect is stronger in the region of steepest gradients than at the pedestal top, the radial electric field shearing is reduced and the L-H transition may be prevented.

With the assumptions of a dominant diamagnetic contribution at the plasma edge, of equal electron and main ion densities due to low impurity content and equal electron and main ion temperatures for sufficiently high density at the pedestal top [39], the radial electric field at and outside the pedestal top can be determined by the electron edge kinetic data:

$$E_{\text{r}} \approx E_{\text{r,dia}} \approx \frac{\nabla p_{\text{e}}}{n_{\text{e}} \text{e}}. \tag{2.4}$$

This relation will be used to investigate the effect of MPs on the L-H transition in chapter 5.

2.2 Edge localized modes

2.2.1 Basics about edge localized modes

ELMs [10, 48] have been observed for the first time with the discovery of the H-mode [7]. During these frequent (10 – 200 Hz) bursts — detected e.g. by the divertor current I_{polsola} (cf. Fig. 2.3 (a)) —, particles and energy are expelled from the plasma edge on a millisecond time scale. This causes a degradation of density (b), temperature (c) and, therefore, also the pressure in the pedestal region, which leads to energy losses of typically 5 – 10 % — some-

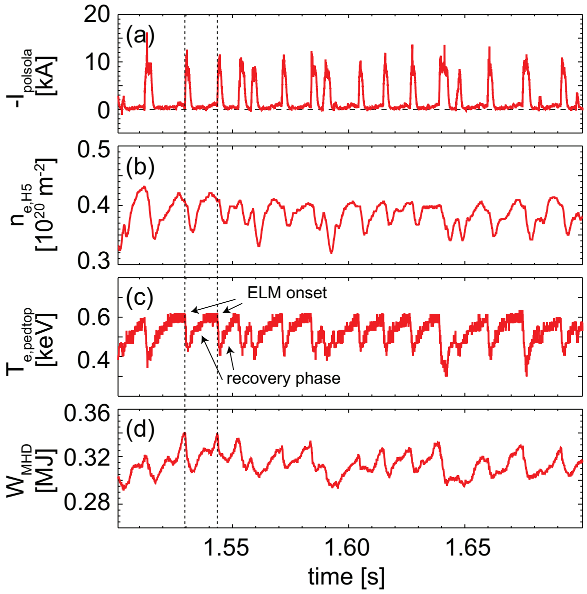

Figure 2.3: Typical time traces of (a) the divertor current, (b) the line-integrated edge density, (c) the pedestal top electron temperature and (d) the plasma stored energy during a type-I ELMy H-mode.

times up to 20 % — of the total plasma stored energy (d). After the ELM crash, the edge kinetic profiles recover until they regain their pre-ELM values.

Besides the most common type-I ELMs with the largest energy and particle losses, several other types of smaller ELMs with different characteristics have been identified [10, 48]. The high frequent type-II ELMs [49] occur at higher triangularity and collisionality compared to type-I ELMs and at close to double null configurations, where the plasma top is near the upper X-point. Type-II ELMs exhibit the characteristic feature of broadband low frequency fluctuations at the edge. Type-III ELMs can be distinguished from type-I ELMs by their existence at lower edge temperatures, their decreasing frequency with increasing heating power and their typical magnetic precursor [50].

In usual H-mode discharges of present day machines ELMs are not harmful. On the contrary, they are desirable to achieve stationary H-modes. In ELM-free phases with high particle confinement, radiation loss from accumulating impurities in the plasma core can cause non-stationarity and a back-transition to L-mode [10]. However, in large devices like ITER or future fusion reactors with higher power fluxes during type-I ELMs, the divertor plates might be damaged. Scalings of the fractional ELM energy loss as a function of pedestal plasma collisionality suggest an energy loss of $\approx 25-80\,\mathrm{MJ}$ for ITER [13] while the tolerable limit for the divertor materials is supposed to be about 10 MJ [51]. ELM mitigation is, therefore, an important issue for the success of ITER.

Various techniques for ELM control have been investigated, but it is not yet obvious which of them is going to meet the ITER requirements. H-mode scenarios with small type-II ELMs, for instance, are achievable in high collisional edge plasmas, whereas ITER will be operated with low edge collisionality [52]. Phases without any ELMs, the 'Quiescent H-modes', have been achieved with neutral beam injection in counter-direction, but their access condition for ITER has not yet been quantified [53]. A possibility to keep type-I ELMs but to actively control them is given by pellet injection. The latter can be used as an ELM trigger and, therefore, allows to set the ELM frequency. With increasing frequency the energy loss per ELM is reduced — but to an extend which might not be sufficient for ITER [54]. Regimes with small type-III ELMs have been observed in discharges with pedestal top electron temperatures below 330 eV [55] provoked either by radiation cooling from intentionally seeded neon impurity or by the application of a very strong gas puff. The latter cools the edge since it consumes energy for the ionization of the neutral atoms. The amount of gas puff necessary for the transition from type-I to type-III ELMs increases with heating power [56]. Yet, this regime is often accompanied by reduced confinement properties which is unfavourable for ITER. Currently, most emphasis is put on investigations of ELM suppression or mitigation via external non-axisymmetric perturbations of the magnetic field which has been discovered on COMPASS-C [14] and JFT-2M [15].

The difficulty to develop a proper tool for ELM control is grounded on the fact that the ELM itself — and its trigger mechanism — is not yet completely understood.

2.2.2 Stability of edge localized modes

Generally, a plasma is in an unstable condition if exposing it to a distortion decreases its potential energy W:

$$\delta W = \delta W_\mathrm{V} + \delta W_\mathrm{S} + \delta W_\mathrm{F} < 0. \tag{2.5}$$

Here, the energy functional has been divided into three components according to different regions — vacuum, surface and fluid — as performed in a fluid picture e.g. in [57]. The vacuum contribution is always stabilizing ($\delta W_\mathrm{V} > 0$). Hence, the crucial contributions for stability analyses when considering a displacement $\vec{\zeta}$ in an ideal (non-resistive) plasma, are given by the surface term

$$\delta W_\mathrm{S} = \frac{1}{2} \int d\vec{S} [\left(\vec{n} \vec{\zeta}_\perp \right)^2 \vec{n} \| \nabla \left(p_0 + \frac{B_0^2}{2\mu_0} \right) \|] \tag{2.6}$$

and the fluid term

$$\begin{aligned} \delta W_\mathrm{F} = \frac{1}{2} \int dV [& \underbrace{\frac{B_{1\perp}^2}{2\mu_0}}_{>0} + \underbrace{\frac{B_{0\perp}^2}{2\mu_0} \left(\nabla \vec{\zeta}_{1\perp} + 2 \vec{\zeta}_{1\perp} \vec{\kappa} \right)^2}_{>0} + \underbrace{\gamma p_0 \left(\nabla \vec{\zeta} \right)^2}_{>0} \\ & - 2 \left(\vec{\zeta}_\perp \nabla p_0 \right) \left(\vec{\kappa} \vec{\zeta}_\perp \right) - \frac{j_\parallel}{B_0} \left(\vec{\zeta}_\perp \times \vec{B}_0 \right) \vec{B}_1], \end{aligned} \tag{2.7}$$

where B denotes the magnetic field with normal vector $\vec{n}$, p the pressure, j the current density, $\vec{\kappa}$ the curvature of the equilibrium magnetic field, γ the adiabatic coefficient and the indices 0 and 1 indicate equilibrium and perturbations, respectively. The first three terms of (2.7) correspond to the torsional Alfvén wave, the compressional Alfvén wave and the plasma compression, respectively, and are always positive. Consequently, the last two terms together with the surface term, which can be positive or negative, decide whether the plasma is stable or unstable. One can therefore distinguish between pressure gradient driven instabilities (fourth term of (2.7) dominant) and current driven instabilities (fifth term dominant).

The most prominent candidate to explain the occurrence of type-I ELMs is the peeling-ballooning model [11] which considers pressure gradient as well as current driven instabilities in the edge region. It predicts the existence of two coupled stability boundaries (blue in Fig. 2.4) formed by the incidences of an ideal ballooning mode which limits the edge pressure gradient and a kink-like peeling mode with the toroidal edge current as driving force.

Ballooning modes [58] are named after their effect of bending the magnetic field lines at the low-field side — the region of unfavourable curvature, where pressure gradient

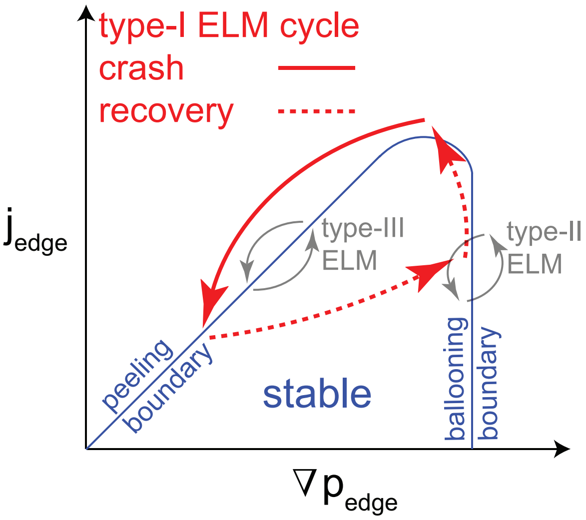

Figure 2.4: Peeling-ballooning stability diagram.

and field line curvature are parallel. This causes a negative contribution to the energy functional by the forth term in (2.7). Ballooning modes have been found to be most unstable for high poloidal mode numbers n and for normalized pressure gradients reaching the ballooning limit [59]:

$$\alpha_{\text{crit}} = \frac{2Rq^2}{B^2}\nabla p, \tag{2.8}$$

calculated for a torus with circular cross section.

Peeling modes [60] are characterized by their non-axisymmetric plasma deformation due to an ideal external kink ($j(a) \neq 0$) with low n. They can become unstable if a resonant surface exists closely outside the separatrix and their stability decreases with higher edge current density. An increasing edge pressure gradient can have a stabilizing effect on the one hand. On the other hand, it increases the edge current density via the bootstrap current [61]. Regarding an arbitrary radial position within the pressure gradient region, a different number of electrons trapped on neighbouring banana orbits is drifting in opposite directions. This causes a net current parallel to the banana traces which is transferred to the free electrons by friction. These then carry the bootstrap current. Peeling modes can be stabilized by increasing the triangularity [10].

According to this model, each type-I ELM cycle (red arrows in Fig. 2.4) consists of three phases: The build-up of the pressure gradient on the fast transport time scale until the ballooning limit is reached. This is followed by an enhancement of the edge current on the lower resistive time scale up to the peeling limit which finally triggers the ELM crash [10, 48]. However, this model does not describe the ELM cycle sufficiently since both the edge pressure gradient as well as the edge plasma current can reach their threshold values several milliseconds before the ELM onset without triggering the ELM immediately [62]. The occurrence of type-II and type-III ELMs might be assigned to pure ballooning or pure peeling [63] modes as indicated by grey lines in Fig. 2.4.

Other models suggest that — at least for type-III ELMs — a finite resistivity is crucial for the stability. One indication therefore is the temperature dependence of type-III ELMs. Their frequency decreases with increasing temperature, i.e. decreasing resistivity, until they are suppressed completely [48].

2.2.3 Observations of ELM mitigation with magnetic perturbations

In typical type-I ELMy H-mode discharges at ASDEX Upgrade, the application of MPs (cf. appendix B) enables mitigation of ELMs in a large variety of MP-coil and discharge settings [64, 17]. The transition from the type-I ELMing to the mitigated regime is always initiated by a decreasing type-I ELM frequency while smaller transport events with higher frequency (hereafter: 'small ELMs') appear in between the remaining large ELMs. At some point the type-I ELMs disappear completely and only small ELMs remain. Like type-I ELMs, they exhibit excursions in temperature and density and a magnetic signature indicating an instability driven by pressure gradient and current density. The ELM energy loss of such a small ELM is typically one order of magnitude lower compared to type-I ELMs. Hence, also the peak divertor power loads on the divertor plates are reduced significantly. The peak values of the line-averaged density are often slightly increased with MPs and tend to be higher in non-resonant compared to resonant phases. The overall plasma confinement is more or less unchanged by the application of MPs. From the unaffected toroidal rotation velocity one might conclude that the penetration of the error fields is low. Last but not least the constant or decreased tungsten and low-Z impurity concentration [65] shows that the plasma cleaning provided by the small ELMs is effective.

The only condition in these discharges for accessing ELM mitigation regimes — apart from a proper MP field configuration — is a threshold in the edge density [64, 17, 31]. With $n = 2$ MPs, ELM mitigation has been achieved with dominant resonant and non-resonant error field contribution in the same way — with a threshold MP-coil current of 350 A and at a peripheral line density $\gtrsim 65\,\%$ of Greenwald density [45]. ELM mitigation with $n = 1$ MPs has been achieved at a slightly lower threshold density ($\approx 60\,\%$ of Greenwald density) in the resonant compared to the non-resonant case. This is in contrast to the different behaviour of non-resonant and resonant MPs with $n = 4$ where only a non-resonant field has been found to suppress type-I ELMs completely. Interestingly, also in the case that only the lower coil row is switched on ELM mitigation can be achieved.

The discovery that ELMs can be affected by non-axisymmetric error fields has been made in COMPASS-C [14] and JFT-2M [15]. Complete ELM suppression with MPs has been observed at DIII-D [66]. This machine provides two sets of six toroidally distributed in-vessel saddle coils creating error fields with toroidal mode number $n = 3$. Full suppression of ELMs is achieved with resonant MPs at low edge collisionality [66]. At high edge collisionality, both resonant and non-resonant MPs only mitigate the ELMs while a small high-frequency MHD activity is remaining [16, 30]. Complete ELM suppression is accompanied with a reduction in the pedestal density ('density pump-out'), while the pedestal temperature is slightly increased. This causes a pedestal pressure gradient below the peeling-ballooning stability threshold [67]. In contrast to this, the edge profiles hardly change with the application of MPs in high collisional edge plasmas. The overall plasma stored energy is in all cases comparable to discharges without MPs.

JET experiments with $n = 1$ and $n = 2$ MP fields produced by four error field correction coils exhibit an enhanced ELM frequency causing a reduced power loss per ELM. A density pump-out has also been found to degrade the edge pressure gradient which moves the operational point in the stability diagram from the peeling-ballooning boundary to the peeling boundary [68, 69]. ELM mitigation has also been observed in MAST discharges with $n = 3$ resonant MPs [18], while at NSTX it has been possible to trigger ELMs and control the ELM frequency with an $n = 3$ error field with strong resonant and non-resonant components [70].

None of these findings can yet be explained by a complete theoretical description of the effect of MPs, i.e. a reliable prediction of ELM control efficiency at ITER is currently not possible.

2.2.4 Hypotheses for ELM mitigation with magnetic perturbations

As the large H-mode edge pressure gradients are believed to be responsible for the occurrence of type-I ELMs, the mechanism for ELM mitigation via MPs might be related to changes in the edge kinetic parameters.

"Hypothesis ELM-I": Peeling-ballooning stabilization due to pressure degradation via field line ergodization Enhanced radial transport due to ergodization may flatten the edge pedestal pressure profile to the point where ELM-related stability limits are no longer reached and ELMs are suppressed. At the same time, diffusive heat and particle fluxes parallel to the magnetic field in radial direction lead to reduced density, impurity content and pedestal top pressure. This mechanism has been invoked to explain the DIII-D ELM suppression experiments from their early days on [16].

A measure for the degree of ergodization is given by the 'Chirikov' parameter [46] which delivers the field line excursions normalized to the distance between the surrounding resonant surfaces. At ASDEX Upgrade, most experiments with MPs exhibit a 'Chirikov' parameter $\sigma > 1$, stating that the islands overlap. However, these calculations are typically based on vacuum perturbation fields and do not include the possibility of helical currents on resonant surfaces, screening the perturbation field [71]. The latter would result in a stronger decaying perturbation field compared to the vacuum approach and the degree of ergodization would be smaller. Hence, it is possible that in contradiction to the calculations, ergodization effects within the confined plasma region are too small as to be able to explain ELM mitigation.

Moreover, even if this hypothesis depicts a possible explanation for the suppression of type-I ELMs, it does not motivate the occurrence of small ELMs. The following hypotheses relate the suppression of the one with the appearance of the other ELM type

— either by shifting the operational point in the stability diagram or by shifting the stability boundary.

"Hypothesis ELM-II": Peeling-ballooning stabilization due to edge cooling It has been mentioned that ELMs can be mitigated via edge cooling with neutral gas. The latter is ionized in the Scrape-Off Layer (SOL) which reduces the local temperature. In the presence of high densities, hence small temperature gradients, this also decreases the pedestal top temperature which can lead to the transition from type-I to type-III ELMs. MPs might act in a similar way by providing an additional source of cold particles. The screening of the perturbation fields in the SOL is much less effective than in the confined plasma due to the higher resistivity of the cold SOL plasma and the target plates. Hence, ergodization of the SOL magnetic field is very likely. In fact, observations of a split power deposition pattern on the target plates ('strike-line splitting') are consistent with vacuum calculations [72]. Furthermore, application of MPs causes a finger-like structure in the edge field lines reaching the SOL and connecting confined and non-confined regions. Additionally with the observation of a high density blob at the high field side [73] it is conceivable that ELM mitigation via MPs is achieved by the creation of field line structures that overlap with the density blob which increases the particle flux from the cold SOL to the edge plasma [29].

"Hypothesis ELM-III": Stability boundary shift Another possibility is that MPs are not effecting the plasma parameters directly but acting on the stability limit of type-I ELMs and/or small ELMs. The decision for the occurring ELM type depends on which stability limit is reached first — i.e. which type of ELM exhibits the lower stability threshold. The presence of that ELM type, prevents the other by clamping the edge density and temperature profiles to the lower stability limit. In the presence of MPs, the stability boundary of either ELM type might be shifted such that small ELMs occur in regimes that are usually — without MPs — dominated by type-I ELMs [30, 31].

In chapter 4 it is tested whether these hypotheses are consistent with the observations of the effect of MPs on the edge kinetic data at ASDEX Upgrade. Therefore, a precise determination of the pedestal profiles and especially the edge gradients is necessary. A method providing this is presented in the next chapter.

3 Edge electron temperature estimation via electron cyclotron emission

(Parts of this work are published in: Rathgeber S K *el al* 2013 *Plasma Phys. Control. Fusion* **55** (2) 025004)

The following chapter is dedicated to the estimation of the electron temperature via Electron Cyclotron radiation Forward Modelling (ECFM). It is demonstrated that this new method delivers — in contrast to commonly applied analysis of Electron Cyclotron Emission (ECE) measurements — reliable electron temperature profiles at the plasma boundary and enables to determine the edge gradient with higher accuracy.

First, the physical principles of radiation emission and transport processes and the applicability of ECE for diagnostic means are introduced in section 3.1. A description of the diagnostic setup and hardware installed at ASDEX Upgrade for electron cyclotron intensity measurements is given in section 3.2. The next two sections are dedicated to the data analysis: An overview about the underlying Bayesian probability theory and its application within preexisting Integrated Data Analysis (IDA) of electron density and temperature at ASDEX Upgrade is given in section 3.3. The ECFM code, which replaces the previous treatment of electron cyclotron intensity within IDA by a more sophisticated one, is described in detail in section 3.4. After the presentation of the electron temperature results obtained with the ECFM method in section 3.5, the relation between the electron temperature and the radiation temperature subject to different plasma characteristics is explained in section 3.6. The sensitivity of the results on program settings and input parameters is studied in section 3.7 and the method is validated and its limitations are pointed out in section 3.8. The chapter ends with a discussion.

3.1 Theoretical background of electron cyclotron radiation

This section provides the basics about the emission and transport processes of electron cyclotron radiation. It is described how to derive the electron temperature at different positions in the plasma from measured electron cyclotron radiation intensities at various frequencies. Thereafter follows a discussion about the assumptions and their insufficiency of conventional ECE analysis and how they are avoided in this work to produce reliable electron temperature profiles also at the plasma edge.

3.1.1 Electron cyclotron frequency

Gyration In a magnetically confined fusion plasma, the electrons gyrate around the magnetic field lines. The equation of motion $\gamma m_{\mathrm{e},0} \mathrm{d}^2\vec{s}/\mathrm{d}t^2 = \vec{F}_{\mathrm{L}} = eB\mathrm{d}\vec{s}/\mathrm{d}t$ with the

Lorentz factor γ and force F_L, the electron mass $m_{\mathrm{e},0}$ and charge e and the magnetic field strength B delivers the gyration or electron cyclotron frequency

$$\omega_\mathrm{ec} = \frac{eB}{\gamma m_{\mathrm{e},0}}. \tag{3.1}$$

Due to their circular acceleration, the electrons emit anisotropic and polarized electromagnetic radiation at their cyclotron frequency and its low harmonics [74, 22].

Resonance position The magnetic field in a Tokamak is dominated by an axisymmetric vacuum toroidal field $B_{\Phi,\mathrm{vac}}$ which decreases strictly monotonically with the major radius R:

$$B_{\Phi,\mathrm{vac}} = \frac{B_0 R_0}{R}, \tag{3.2}$$

where B_0 is the magnetic field at the position of the magnetic axis R_0. For the exact magnetic field strength also the poloidal field component B_Θ and corrections of the vacuum field and the axial symmetry have to be considered:

$$B_\mathrm{tot} = B_{\Phi,\mathrm{vac}} + B_\Theta + B_\mathrm{dia} + B_\mathrm{rip}. \tag{3.3}$$

The necessity for the latter arises from the magnetic field ripple caused by the spacing between the toroidal field coils. Vacuum field correction are required due to the diamagnetic response of the plasma.

According to (3.1) and (3.3) one can infer the localization of the electron cyclotron radiation origin from its frequency [74, 22].

Broadening effects However, the emission at a certain frequency is not discretely localized in the plasma, but is subject to two different broadening effects [74, 55]. As a reference for the frequency broadening the cold resonance frequency of the m^th harmonic, which is caused by unperturbed non-relativistic electrons without any energy contribution parallel to the magnetic field lines, is defined as:

$$\omega_m = m\frac{eB}{m_{\mathrm{e},0}}. \tag{3.4}$$

Regarding high temperatures, relativistic mass increase ($\gamma > 1$ in (3.1)) of the

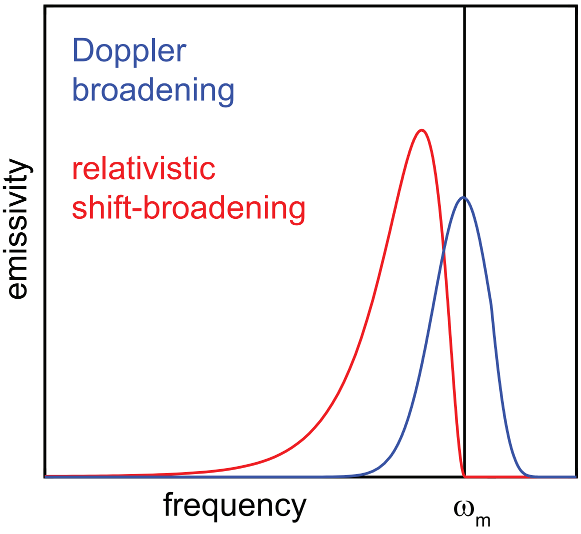

Figure 3.1: Doppler broadened (blue) and relativistic shift-broadened (red) emission profiles relative to the cold resonance frequency (black line).

electrons causes electron cyclotron emission at frequencies smaller than the cold resonance frequency. Together with a Maxwellian electron distribution this leads to a broadened emission profile with down-shifted maximum and an upper frequency limit given by the cold resonance frequency as shown in red in Fig. 3.1. Contrary to this asymmetric relativistic effect, the second important broadening mechanism due to Doppler shift results in a Gaussian-shaped emission profile (blue) around the cold resonance frequency (black). Doppler broadening occurs due to velocity contributions parallel to the magnetic field lines and deviations from perpendicular viewing — caused by oblique viewing lines and the finite acceptance angle of the antenna pattern. Its symmetric shape is justified by the assumption that mean electron movements in a distinguished direction like parallel drifts with velocities of $\sim 10^5\,\mathrm{ms^{-1}}$ are negligible compared to the isotropic thermal movement which is in the order of $10^6 - 10^7\,\mathrm{ms^{-1}}$. Other broadening effects like natural broadening due to radiative energy loss or collision broadening due to energy transfer to the bouncing particle are also negligible.

Cut-off Despite being resonant, the wave might not be able to propagate through some regions of the plasma if the frequency is lower than the cut-off frequency [75]. This cut-off occurs if the refractive index becomes imaginary. Ordinary mode waves ($E \parallel B_0$) with refractive index $N_\mathrm{O} = \sqrt{1 - (\omega_\mathrm{p}/\omega)^2}$ become evanescent for frequencies smaller than the plasma frequency $\omega_\mathrm{p} = \sqrt{(n_\mathrm{e} e^2)/(\epsilon_0 m_\mathrm{e,0})}$. For extraordinary mode waves ($E \perp B_0$) with $N_\mathrm{X} = \sqrt{1 - \omega_\mathrm{p}^2 \left(\omega^2 - \omega_\mathrm{p}^2\right) \left(\omega^2 \left[\omega^2 - \omega_\mathrm{p}^2 - \omega_\mathrm{ec}^2\right]\right)^{-1}}$ the right-hand cut-off frequency is given by $\omega_\mathrm{R} = \frac{1}{2}\left(\omega_\mathrm{ec} + \sqrt{\omega_\mathrm{ec}^2 + 4\omega_\mathrm{p}^2}\right)$. Hence, it is not possible to measure any electron cyclotron emission coming from regions with electron densities larger than the cut-off density

$$\begin{aligned} n_\mathrm{co}^\mathrm{1O} &= \frac{\epsilon_0 m_\mathrm{e,0}}{e^2}\omega_\mathrm{1O}^2 \\ n_\mathrm{co}^\mathrm{2X} &= \frac{\epsilon_0 m_\mathrm{e,0}}{2e^2}\omega_\mathrm{2X}^2 \end{aligned} \tag{3.5}$$

of the mostly observed first harmonic Ordinary mode (1st harmonic O-mode) and second harmonic eXtraordinary mode (2nd harmonic X-mode), respectively.

3.1.2 Electron cyclotron intensity

As discussed in the previous section, the frequency of the measured electron cyclotron radiation contains information about the emission origin. On the other hand, the temperature of the radiating electrons can be deduced from the intensity of the waves emerging the plasma.

Radiation transport equation Due to the broadened resonance region the ray path exhibits a finite length of plasma-wave interaction. Hence, to obtain the measured intensity at angular frequency ω one has to consider the radiation transport through the emitting plasma [22]:

$$\frac{\mathrm{d}}{\mathrm{d}s}\frac{I_\omega(s)}{N^2} = \frac{1}{N^2}\left(j_\omega(s) - \alpha_\omega(s) I_\omega(s)\right). \tag{3.6}$$

The radiation transport equation states that along the ray path s the spectral intensity I_ω — corrected by the refractive index N — increases according to the emissivity j_ω of the respective frequency but at the same time is reduced by a fraction α_ω of the actual intensity due to re-absorption.

Emissivity The emissivity is defined as the rate of emission of radiant energy per unit volume, frequency and solid angle. In free-space approximation for sufficiently tenuous plasma, the emissivity originating from single uncorrelated radiating electrons can be derived from Maxwell's equations, the Lienard-Wiechert potentials for point charges and Poynting's theorem as performed e.g. in [74]. A weakly relativistic plasma ($k_\mathrm{B}T_\mathrm{e} \ll m_{\mathrm{e},0}c^2$) in local thermal equilibrium (Maxwell-distributed electrons) yields for the 2nd harmonic X-mode ($\omega_m = \omega_{2\mathrm{X}} = 2eB/m_{\mathrm{e},0}$) a spectral emissivity of:

$$j_{2\mathrm{X}}(\omega) = \eta_{2\mathrm{X}} j \Phi(\omega) \tag{3.7}$$

with frequency and polarization independent total emissivity

$$j = \left(\frac{e\omega_{2\mathrm{X}}}{4\pi\zeta}\right)^2 \frac{n_\mathrm{e}}{\epsilon_0 c}\sin^2\theta\left(\cos^2\theta + 1\right), \tag{3.8}$$

normalized ($\int \Phi(\omega)d\omega = 1$) shape function

$$\Phi(\omega) = \frac{\zeta^{7/2}}{\sqrt{\pi}}\int \delta\left(\left[1-\beta_\parallel\cos\theta\right]\omega - \sqrt{1-\beta^2}\omega_{2\mathrm{X}}\right)\exp\left(-\zeta\left[\beta_\perp^2+\beta_\parallel^2\right]\right)\beta_\perp^5\mathrm{d}\beta_\perp\mathrm{d}\beta_\parallel \tag{3.9}$$

and the fraction of power that is emitted in X-mode $\eta_{2\mathrm{X}}(= 1 - \eta_{2\mathrm{O}})$. $\beta_\parallel = v_\parallel/c$ and $\beta_\perp = v_\perp/c$ denote the parallel and perpendicular velocity contributions as a fraction of the speed of light c, θ the viewing angle relative to the magnetic field lines and $\zeta = (m_{\mathrm{e},0}c^2)/(2k_\mathrm{B}T_\mathrm{e})$ with Boltzmann constant k_B and electron temperature T_e. Note here that the emissivity depends on the electron temperature as well as the density (cf. (3.8)). From the delta function in (3.9), giving only a contribution to the emissivity if the resonance condition

$$\omega = \frac{\sqrt{1-\beta_\parallel^2-\beta_\perp^2}}{1-\beta_\parallel\cos\theta}\omega_{2\mathrm{X}} \tag{3.10}$$

is fulfilled, one can derive the broadening of the emission region depending on electron velocity and viewing angle. Doppler broadening is dominant if $\beta_\parallel\cos\theta > \beta^2$. Elsewhere the frequency is mainly down-shifted relative to the cold resonance frequency due to relativistic mass increase [74].

Absorption In a local thermal equilibrium the absorption is directly proportional to the emissivity according to Kirchhoff's law

$$\alpha(\omega) = \frac{j(\omega)}{I_{\mathrm{BB}}(\omega)}, \tag{3.11}$$

where the absorption coefficient α is defined as the fractional rate of absorption of radiation per unit path length and I_{BB} denotes the black-body intensity. The latter is given by Planck's radiation formula

$$I_{\mathrm{BB}}(\omega) = \frac{\hbar\omega^3}{8\pi^3 c^2}\left[\exp\left(\frac{\hbar\omega}{k_{\mathrm{B}}T_{\mathrm{e}}} - 1\right)\right]^{-1}, \tag{3.12}$$

which is simplified by the Rayleigh-Jeans approximation for hot plasmas and electron cyclotron radiation in the microwave range ($\hbar\omega < meV \ll k_{\mathrm{B}}T_{\mathrm{e}}$) [74]:

$$I_{\mathrm{BB}}(\omega) = \frac{\omega^2}{8\pi^3 c^2} k_{\mathrm{B}}T_{\mathrm{e}}. \tag{3.13}$$

Optical depth The optical depth [74, 22]

$$\tau_{12} = \int_1^2 \alpha(s)\mathrm{d}s, \tag{3.14}$$

denotes the integration of the absorption along the path s. The plasma is said to be optically thick or opaque if $\tau \gg 1$ and optically thin if $\tau \lesssim 1$.

3.1.3 ECE analysis

On the basis of preceding physical principles, it is possible to judge the validity of commonly applied ECE analysis. In the following, its assumptions, success and failure are pointed out. As a consequence of these limitations, which are especially relevant at the plasma edge, a complete description of the radiation transport is necessary for a correct treatment of the ECE data and reliable edge electron temperatures.

Optically thick plasma approximation In an optically thick plasma, the absorption over a sufficient path length is high enough to fully re-absorb the incident radiation. According to (3.6) and (3.11) and under stationary plasma conditions ($\nabla T_{\mathrm{e}} = \nabla n_{\mathrm{e}} = 0$), the intensity is constant along the path and equal to black-body intensity. As a second effect of the high re-absorption, the actual measured emission region is narrowed and, therefore, becomes localized closer to the position of cold resonance. Common ECE analysis (hereafter: 'classical' ECE analysis) consequently applies the approximation of a plasma emitting electron cyclotron radiation at black-body level from the cold resonance position of the measurement frequency. In this case the analysis is straight-forward since the measured intensity is no longer density-dependent and directly proportional to the electron temperature. The latter is therefore easily obtained without the necessity of a deconvolution according to

$$T_\mathrm{e}(R_\mathrm{res}(\omega)) = T_\mathrm{rad}(\omega) \equiv 8\pi^3 c^2 I_\mathrm{BB}/(k_\mathrm{B}\omega^2), \tag{3.15}$$

with cold resonance position R_res given by (3.4) and (3.3). The choice of proper frequencies, resonant along the whole plasma cross section, then enables to obtain complete electron temperature profiles. However, the assumption of an optically thick plasma is usually valid only in the bulk of a fusion plasma for the 1st harmonic O-mode and the 2nd harmonic X-mode [74, 22].

ECE analysis at the plasma edge In regions of steep temperature gradients and optically thin plasma — typical edge conditions for H-mode plasmas — the 'classical' ECE analysis fails. Strong gradients in the temperature and, therefore, also in the black-body intensity can cause significant variations in the measured radiation temperature already for small deviations of the emission origin from the cold resonance position. Furthermore, in case of optically thin plasma, the radiation along the path is not fully re-absorbed and emission coming from a broad region up to far inside the cold resonance position is collected by the antenna. A direct evidence for the misinterpretation of identifying the radiation temperature with the electron temperature at the position of its cold resonance is given by the so-called 'shine-through' effect. This denotes the occurrence of a peak in the radiation temperature with cold resonance in the Scrape-Off Layer (SOL). The 'shine-through' temperatures can reach several hundred eV and have been observed at different machines [26, 27, 28]. Such high electron temperatures outside the separatrix would cause an immediate plasma extinction due to the strong parallel heat transport ($K_\parallel \propto T^{5/2}$) [76]. This implies that establishing reliable electron temperature profiles at the plasma edge needs complete handling of radiation transport processes and the consideration of all broadening mechanisms. A detailed description of how this was realized at ASDEX Upgrade is given in section 3.4.

3.2 Electron cyclotron emission measurement at ASDEX Upgrade

The optimal radiation range — regarding frequency and polarization — for diagnosing the electron cyclotron intensity is defined by the magnetic field and the electron density determining the resonances and cut-offs. At ASDEX Upgrade, with magnetic field

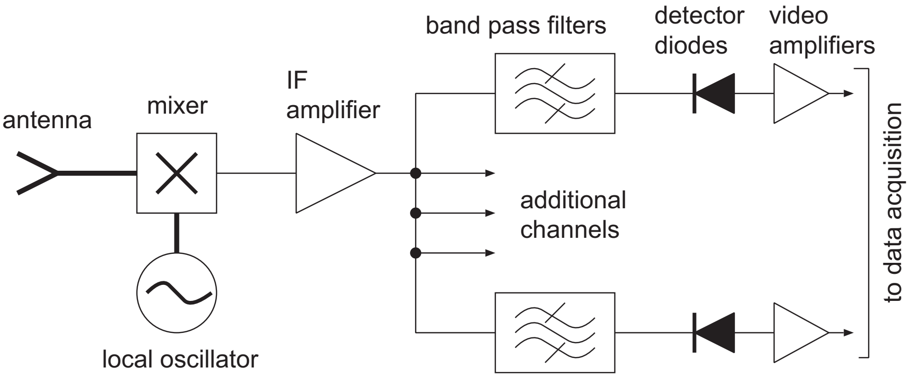

Figure 3.2: Schematic of a broadband multichannel heterodyne radiometer for ECE measurements [77].

strengths in the range of $B_{\mathrm{tot}} = 1-3\,\mathrm{T}$ and electron densities of $10^{19} - 10^{20}\,\mathrm{m}^{-3}$, the 2^{nd} harmonic X-mode in the millimetre or microwave range ($\nu_{2\mathrm{X}} \sim 100\,\mathrm{GHz}$) provides the best measurement conditions. This range is accessible to radio frequency receiver techniques, which is realised at ASDEX Upgrade via a heterodyne radiometer receiver [25].

3.2.1 Heterodyne radiometer

The 60-channel heterodyne radiometer receiver installed at ASDEX Upgrade measures frequencies of $\nu_{\mathrm{ECE}} = 85 - 185\,\mathrm{GHz}$ and exhibits a radial resolution of up to $\approx 5\,\mathrm{mm}$ and a temporal resolution of $32\,\mu\mathrm{s}$ with the standard CAMAC data acquisition system or $1\,\mu\mathrm{s}$ with the recently installed SIO system. The function of a heterodyne receiver is to down-convert the input radio frequency signal by interference with a similar frequency in order to facilitate the amplification and filtering.

The schematic of such a system is shown in Fig. 3.2. At ASDEX Upgrade, there are four antennae, equipped with linear polarizing wire grids to select only the X-mode. The incident radiation is transmitted via waveguides in mono-mode or oversized multi-mode to three of the five available mixers that interfere the input signal with the local oscillator signal at frequencies of $\nu_{\mathrm{LO}} = 95, 101, 128, 133$ or $167\,\mathrm{GHz}$. The resulting intermediate frequency signal is in the range of $\nu_{\mathrm{IF}} = 2-18\,\mathrm{GHz}$ with power proportional to the input power. The selected mixers are connected to three different intermediate frequency chains, consisting of an intermediate frequency amplifier and 36, 12 and 12 channels respectively. In every channel the signal passes a band pass filter where the frequency interval is selected with a bandwidth of 300 MHz for the 36 channel system and 600 MHz for the 12 channel systems — chosen such that they match the resolution limits given by the broadening effects —, an unbiased Schottky diode, a video amplifier and then enters the CAMAC data acquisition system with 31.25 kHz sampling rate [77].

The system is calibrated by measurements of black-body radiation emitted by laboratory hot ($T = 773\,\mathrm{K}$) and cold sources ($T = 77\,\mathrm{K}$) [25].

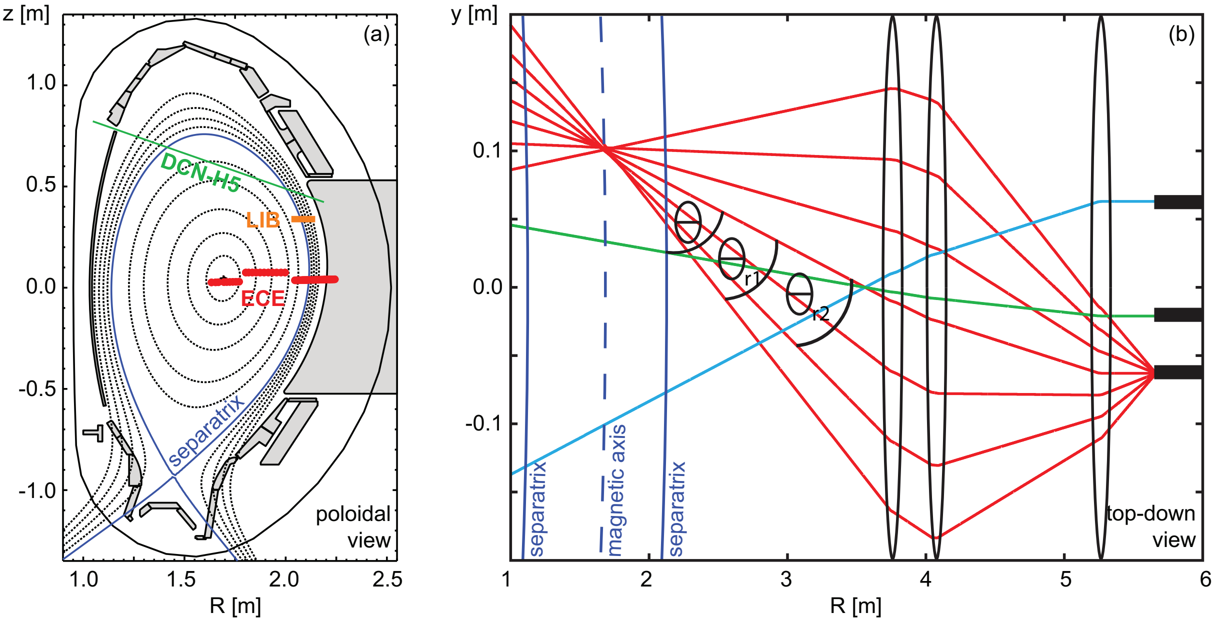

Figure 3.3: (a) Poloidal cross section of the ASDEX Upgrade vessel with the flux surfaces (black, dashed), the separatrix (blue, solid) and the cold resonance positions of the 60 ECE channels (red dots); additionally shown are the positions of the LIB diagnostic (orange) and the 'H5' channel of DCN interferometry (green). (b) Top-down view on the ECE antenna and lens setup (black), the resulting LOS with antenna pattern (red) or central ray only (blue, green) and the positions of the separatrices (dark blue, solid) and the magnetic axis (dark blue, dashed).

3.2.2 Line of sight geometry

The ECE diagnostic is located in sector 9 of the ASDEX Upgrade vessel, viewing the plasma from the low-field side. The red dots in Fig. 3.3 (a) mark the positions of cold resonance of all 60 ECE channels for a typical frequency setting. They are located close to the midplane and mainly at the low-field side. The vertical displacement of the twelve mid channels arises from the different z-position of their antenna.

The Lines Of Sight (LOS) of the different antennae each form approximately a Gaussian beam focussed by a system of three lenses as shown in Fig. 3.3 (b). The blue and green lines represent the central ray of the corresponding antenna only. The red lines illustrate exemplarily the widened viewing area due to the finite antenna pattern with angle θ_rx to the central ray.

3.3 Integrated data analysis

For the estimation of the electron temperature from measured electron cyclotron radiation intensities, the concept of IDA in the framework of Bayesian probability theory was applied. IDA enables the assessment of physical quantities via combined analysis of data from different diagnostics providing complementary information about the quantities of interest. It includes a forward model for each diagnostic reflecting its particular physical principle, an elaborate treatment of all uncertainties and a joint optimization process to gain a common set of parameter values for the quantities of interest that match all the measured data best. By using heterogeneous sources of information about the same physical quantities and by taking benefit from interdependencies via simultaneous analysis of different physical quantities, the reliability of the resulting quantities is improved and inconsistencies between the diagnostics can be resolved.

3.3.1 Bayesian probability theory

Contrary to conventional statistical interpretations, probability in terms of Bayes' theory [78, 79] serves as a measure of the 'degree of belief' of a quantity, rather than its frequency distribution. This enables to include — in addition to the actual measured data — previous knowledge about the quantities of interest which is independent from the experimental measurements. The probability of this a priori information about the physical quantities, which are parameterised by x and y, is quantified by the prior Probability Density Function (PDF) $p(x, y)$. The information about the experimental data is contained in the likelihood PDF $p(d|x, y)$, denoting the conditional probability to measure d for given parameter values x, y.

These PDFs are linked via Bayes' theorem:

$$p(x, y|d) = \frac{p(d|x, y)p(x, y)}{p(d)}. \tag{3.16}$$

The posterior PDF $p(x, y|d)$ indicates the probability for the physical quantities to possess the values x, y if d is measured. Maximization of the posterior PDF delivers the parameter values that are most likely to produce the measured data set. Since the evidence PDF $p(d)$ in (3.16) is just a normalisation and does not influence the position of the maximal posterior value, it is omitted in this application of Bayes' theorem.

3.3.2 IDA at ASDEX Upgrade

The ECFM code, which is described in detail in section 3.4, was implemented into an already existing IDA package. The latter is routinely used at ASDEX Upgrade for the estimation of the electron density and temperature as presented in [24]. The standard application of IDA currently involves the data from the LIthium Beam emission spectroscopy (LIB, cf. appendix C) and the Deuterium CyaNide interferometry (DCN, cf. appendix A) for the density and the ECE data — applying the 'classical' optically thick plasma approximation — for the temperature evaluation. Also established in the IDA program are the analyses of the Thomson Scattering spectroscopy (TS) and REFlectometry (REF) data. However, they are not used for routine analysis due to the poor temporal resolution of the TS system [80] and the low memory capability of the REF data acquisition system which does not allow to diagnose the whole discharge with high temporal resolution.

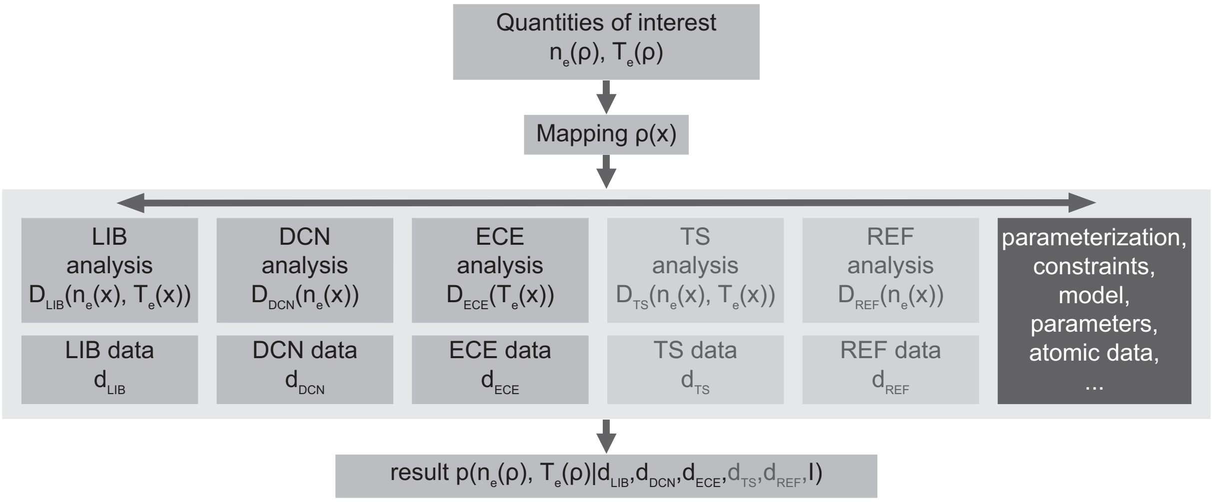

Figure 3.4: Schematic of the IDA process at ASDEX Upgrade.

The quantities of interest, electron density and temperature, are provided as exponentials of cubic B-splines over several parameter values at different positions between $\rho = 0$ and 1.2. The normalised poloidal radius $\rho = \sqrt{\frac{\Psi - \Psi_\mathrm{axis}}{\Psi_\mathrm{separatrix} - \Psi_\mathrm{axis}}}$ with poloidal flux Ψ (cf. Fig. 1.1 for the location of $\rho = 0$ and 1) offers a common coordinate system for all the diagnostics. Given the profile(s) of electron density and/or temperature and the information for the mapping to its/their corresponding experimental setup, the forward model of each diagnostic generates values for the measured quantity. The deviation between the modelled data D and the measured data d, weighted by the measurement uncertainties, yields the likelihood PDF $L \equiv p(d|x, y) \propto \exp\left(-\left[\{D - d\}/\Delta d\right]^2\right)$ using a Gaussian or $L \equiv p(d|x, y) \propto \left(1 + \left[\{D - d\}/\Delta d\right]^2\right)^{-1}$ using a Cauchy distribution [81]. Combining these for all the diagnostics together with the prior information according to (3.16) results in the posterior PDF

$$\text{Posterior} \propto \mathrm{L}_\mathrm{LIB} \times \mathrm{L}_\mathrm{DCN} \times \mathrm{L}_\mathrm{ECE}\, (\times \mathrm{L}_\mathrm{TS} \times \mathrm{L}_\mathrm{REF}) \times \text{Prior}, \tag{3.17}$$

which — maximized — delivers the results for electron density and temperature that are best compatible with all the measurements and the a priori constraints (e.g. positivity of electron density and temperature, smoothness and monotonicity of the profiles, ...).

The standard error analysis applies the χ^2-binning method [82] where single or groups of neighboured density/temperature values are increased and decreased as long as the modelled data D_i of channel i deteriorates from the measured data $d_{i,j}$ at time j such that $\Delta\chi^2 = \Delta \sum_{i,j} \left(\left[d_{i,j} - D_i\right] / \Delta d_{i,j}\right)^2 > 1$. These values form the upper and lower bounds of the original value. This rather simple method with independent error bars that do not include any prior information provides an intuitive assessment of the informational content of the measurement.

The IDA package also contains the possibility to calculate the uncertainties via Markov

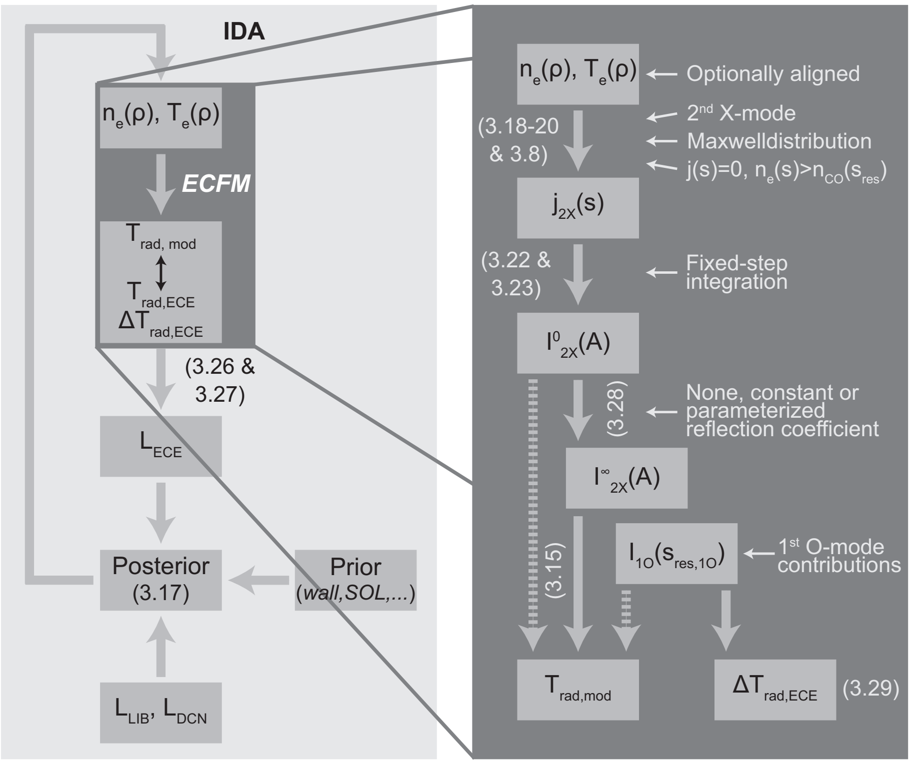

Figure 3.5: Left: Schematic of the IDA process; the new features (ECFM code and additional prior information) are indicated by italics. Right: Schematic of the ECFM code with default process marked by solid arrows; the numbers denote the equation used for the corresponding step in the program.

Chain Monte Carlo (MCMC) methods [82]. With Monte Carlo methods [83] it is possible to reconstruct the posterior PDF — including its mean, maximum and width — by taking a large set of arbitrary samples. In high dimensional parameter space, the usage of Markov chains [84] — sequences of samples with correlated probabilities — increases the effectiveness for the sampling. The width of the posterior PDF delivers the model uncertainties.

3.4 Code implementation: ECFM

As already mentioned, the newly developed Electron Cyclotron radiation Forward Modelling (ECFM) code was included into the existent IDA program described in section 3.3. It replaced the assumption $T_\mathrm{e}(\rho_\mathrm{res,2X}) = \mathrm{T}_\mathrm{rad,mod}(\nu_\mathrm{ECE})$ of the 'classical' analysis by the modelling of the electron cyclotron radiation transport, which generated the radiation temperature for given electron density and temperature profiles applying a new analytical formula for the emission profile. The surrounding IDA process (cf. left-hand side of Fig. 3.5), of forming the likelihood PDFs for every diagnostic, combining them via Bayes' theorem with the prior PDFs, maximizing the posterior PDF via gradient-based optimization processes and assessing the uncertainties via χ^2-binning method, was — apart from the inclusion of some additional prior information — applied as described in the previous section.

Input data The schematic of the ECFM code is sketched on the right-hand side of Fig. 3.5. It needed complete profiles of the electron density and temperature as input. The density profile was optionally aligned to the temperature profile. This alignment was regulated manually by a fixed radial scale of the density profile or automatically by adapting the position of the density value with maximum curvature — which was assumed to occur at the separatrix [85] — either to $\rho = 1.0$ or to the position of $T_{\mathrm{e}} = 100\,\mathrm{eV}$ (default setting) — a reasonable separatrix condition for the electron temperature [86]. Apart from the alignment, the density profile was mainly determined by the LIB and DCN data and was only slightly adapted to the ECE data.

Calculation of the radiation intensity Given $n_{\mathrm{e}}(\rho)$, $T_{\mathrm{e}}(\rho)$ and their mapping to the ECE viewing lines, the emissivity

$$j_{\nu,r}(s) = \begin{cases} 0 & \text{for } n_{\mathrm{e}}(s) > n_{\mathrm{co}}^{2\mathrm{X}}(s) \\ \eta_{2\mathrm{X}}(s) j(s) \Phi_{\nu,r}(s) & \text{else} \end{cases} \tag{3.18}$$

was calculated at every position s along the LOS where the frequency was not in cut-off and set to 0 elsewhere, because the radiation was not able to propagate inside the cut-off layer. Possible reflections were considered separately as described later. ECE channels that were in cut-off at the position of their cold resonance were discarded completely.

The total emissivity $j(s)$ was given by (3.8). For the shape function $\Phi_{\nu,r}(s)$, a new analytical formula was found. It was derived by the integration of (3.9) as carried out in appendix D:

$$\begin{aligned} \Phi(\nu) = {} & \frac{\zeta^{3/2}}{2\pi^{3/2}\nu\mu\cos^5\theta} \times \\ & \times \left[\exp\left(-\zeta\left\{1-\mu\alpha\right\}\right) \left(-\frac{\sin^2\theta}{\sqrt{\alpha}} + \frac{\eta^2}{\zeta\mu} - \frac{1}{\sqrt{\zeta\mu}} \left\{3\eta - 2\zeta\mu\sin^2\theta\right\} F\left(\sqrt{\zeta\mu\alpha}\right) \right) \right]_{\alpha_2}^{\alpha_1} \end{aligned} \tag{3.19}$$

with substitutions $\mu = \nu^2/\nu_{2\mathrm{X}}^2$, $\alpha = \left(1 - \beta_{\|}\cos\theta\right)^2$ and $\eta = 1 + \mu\cos^2\theta$ and Dawson integral $F(x) = \exp\left(-x^2\right)\int_0^x \exp\left(y^2\right)\mathrm{d}y$. The bounds of integration were given by $\alpha_{1,2} = \left(1 \pm \sqrt{1 - \mu\sin^2\theta}\cos\theta\right)^2/\eta^2$.

The X-mode fraction $\eta_{2\mathrm{X}}(s)$ was determined by

$$\eta_{2\mathrm{X}} = \frac{1}{2} + \frac{\frac{1}{8}\sin^4\theta + \cos^2\theta}{\left(\cos^2\theta + 1\right)\sqrt{\cos^2\theta + \frac{1}{16}\sin^4\theta}}, \tag{3.20}$$

applying the tenuous plasma approach ($\nu \gg \nu_{\mathrm{p}}$) which was usually fulfilled at the plasma edge [74] and, therefore, appropriate for our purpose. Here, it should be noted that the frequency switched from angular frequency ω to the measured frequency $\nu = \omega/(2\pi)$.

To increase the radial resolution not only the emission profile of the central frequency ν_{ECE} of each channel was calculated, but its measurement bandwidth $\Delta\nu_{\mathrm{ECE}}$ was discretized in N_ν (Default: $\mathrm{N}_\nu = 3$) equally distributed frequency intervals with bandwidths $\Delta\nu = \Delta\nu_{\mathrm{ECE}}/\mathrm{N}_\nu$.

At the same time, there was the option to split the LOS in N_r toroidally distributed rays r, accounting for the finite beam width. The electron density and temperature values along each ray were thereby taken over from the central ray of the corresponding LOS. This was motivated by the rays each transversing plasma regions with the same characteristics, given the validity of toroidal symmetry. Therefore, to consider the antenna pattern only the angle to the magnetic field had to be adapted via $\angle(\vec{B}, \mathrm{ray}) = \theta \pm \theta_r$ (cf. Fig. 3.3). The angle θ between the magnetic field lines and the central ray was calculated with the assumption of a magnetic field contribution only in the R-y-plane since the toroidal magnetic field was one order of magnitude larger than the poloidal magnetic field. The actual angle between the ray r and the magnetic field was given by simply adding or subtracting θ_{rx} to or from θ. This was justified by the curvature of the magnetic field being negligible within the small viewed area. The LOS were represented by straight lines which was justified at the tenuous plasma edge where refraction could be neglected.

Knowing the emissivity and via Kirchhoff's law (3.11) also the absorption, the intensity for each frequency and each ray was obtained by solving the radiation transport equation (3.6) with the refractive index $N = 1$ in the tenuous plasma approach:

$$\frac{\mathrm{d}I_\nu(s)}{\mathrm{d}s} = j_\nu(s) - \alpha_\nu(s) I_\nu(s). \tag{3.21}$$

This was done by simple integration with $N_{\mathrm{s}} = 1000$ fixed steps Δs ($\approx 0.1\,\mathrm{mm}$ close to the cold resonance position and $\approx 2\,\mathrm{mm}$ elsewhere) from the inner wall to the antenna:

$$I_{\nu,r}(\mathrm{A}) = \sum_{\mathrm{W}}^{\mathrm{A}} \left(j_{\nu,r}(s) - \alpha_{\nu,r}(s) I_{\nu,r}(s)\right) \Delta s. \tag{3.22}$$

From the computational point of view it would have been preferable to use an ODE solver with adaptable step size to solve the radiation transport equation. Unfortunately, the emissivity calculation was not absolutely numerically stable because the terms in (3.19) could possess very similar values which led to large round-off errors. This caused discontinuities in the intensity calculation which were way too small to have an influence on the result, but were not tolerable for the gradient-based optimization process.

To get the total modelled single-pass radiation intensity $I^0_{\mathrm{A}}(\nu_{\mathrm{ECE}})$ for one ECE channel, one had to sum up all the discretized frequencies and rays

$$I^0_{\nu_{\mathrm{ECE}}}(\mathrm{A}) = \sum_{\nu=1}^{\mathrm{N}_\nu} \sum_{r=1}^{\mathrm{N}_r} I_{\nu,r}(\mathrm{A}) w(\theta_r) \Psi(\nu) \Delta\nu \tag{3.23}$$

with the Gauss-shaped weighting function

$$w(\theta_r) = \sqrt{\frac{\ln 2}{\pi}} \frac{2}{\Delta\theta_\mathrm{r}} \exp\left(-\frac{4\ln 2}{(\Delta\theta_\mathrm{r})^2}\theta_r^2\right) d\theta_r, \tag{3.24}$$

where $\Delta\theta_r$ denoted the full width of half maximum and $\mathrm{d}\theta_r$ the discretized antenna pattern for the different rays r and with the filter function

$$\Psi(\nu) = \begin{cases} \frac{1}{\Delta\nu_\mathrm{ECE}} & \text{for } \nu_\mathrm{ECE} - \frac{\Delta\nu_\mathrm{ECE}}{2} \le \nu \le \nu_\mathrm{ECE} + \frac{\Delta\nu_\mathrm{ECE}}{2} \\ 0 & \text{else} \end{cases} \tag{3.25}$$

of the band pass filter.

Finally, the calculated radiation intensity was translated into the radiation temperature $T_\mathrm{rad,mod}(\nu_\mathrm{ECE})$ via (3.15) which was then compared to the measured data within the likelihood PDF

$$\mathrm{L}_\mathrm{ECE} = \frac{1}{\prod_{i,j}\sqrt{2\pi\left(\Delta T_\mathrm{rad,ECE}(i,j)\right)^2}} \exp\left(-\frac{1}{2}\chi^2\right) \tag{3.26}$$

$$\chi^2 = \sum_{i,j}\left(\frac{T_\mathrm{rad,ECE}(i,j) - T_\mathrm{rad,mod}(i)}{\Delta T_\mathrm{rad,ECE}(i,j)}\right)^2 \tag{3.27}$$

for all ECE channels i and measured time points j within the time frame selected for the analysis where the profiles were assumed to be constant.

Wall reflections Optionally, contributions from wall reflections and the 1st harmonic O-mode were added to the modelled radiation intensity. The former might cause multiple ray passes through the plasma and — especially in the fully tungsten-coated ASDEX Upgrade machine — a significantly enhanced intensity I_A at the antenna compared to the single-pass intensity I_A^0. This was incorporated within ECFM via the infinite-reflection model

$$I_\mathrm{A} = \frac{I_\mathrm{A}^0}{1 - R\mathrm{e}^{-\tau}}, \tag{3.28}$$

considering infinite reflections back and forth between parallel walls with reflection coefficient R for both walls [22]. In an optically thick plasma with $\tau \gg 1$ this did not cause a contribution to the antenna intensity, because the reflected intensity was re-absorbed completely, but it had to be taken into account in optically thin plasmas. The reflection coefficient was either given by a fixed value (default: $R = 0.99$) or as a model parameter.

1st harmonic O-mode contributions Due to harmonic overlap and mode conversion by polarization scrambling at the walls, radiation emitted by electrons at the high-field side in 1st harmonic O-mode might influence the measurement. This contribution was usually negligible compared to the 2nd harmonic X-mode radiation emitted in the main plasma since it was mostly re-absorbed on its path through the optically thick plasma. Furthermore, densities in typical ASDEX Upgrade discharges were generally much higher than the cut-off density of the 1st harmonic O-mode. Nevertheless, it was conceivable that O-mode radiation emitted outside the cut-off layer on the high-field side travelled poloidally around the plasma by reflections back and forth between the inner vessel wall and the cut-off layer and reached the antenna at the low-field side — partly converted to X-mode. This could hardly be modelled due to the complex reflection structures and unknown depolarization fraction. However, 1st harmonic O-mode contributions were approximated roughly by the application of the optically thick plasma approach and the assumption that they were fully converted to X-mode and completely reached the antenna: $T_{\mathrm{rad}}^{\mathrm{tot}}(\nu_{\mathrm{ECE}}) = T_{\mathrm{rad}}^{2\mathrm{X}}(\nu_{\mathrm{ECE}}) + T_{\mathrm{rad}}^{1\mathrm{O}}(\nu_{\mathrm{ECE}}) = T_{\mathrm{rad}}^{2\mathrm{X}}(\nu_{\mathrm{ECE}}) + T_{\mathrm{e}}(\rho_{\mathrm{res,1O}})$. This approach had been used to estimate the sensitivity of the model on 1st harmonic O-mode contributions. Nevertheless, since it was generally not valid, possible O-mode contributions were usually not considered in the calculation of the absolute radiation temperature value, but only taken into account as an additional source of uncertainty in the measurement. Outside a certain value (default: $\rho = 1.05$), where O-mode contributions were assumed to dominate over radiation emitted in the 2nd harmonic X-mode, the ECE data were given very large error bars and, therefore, were neglected in the model.

Error assessment Additionally to the 1st harmonic O-mode contributions, the uncertainty in the ECE measurement was composed of an approximated error of 7 % on the data for all channels including systematic uncertainties from the calibration process and the temperature dependence of the gains and the mixers, a factor f_{SNR} of the data including the individual signal to noise ratio of every channel provided by the calibration procedure, the 1σ-standard deviation of the statistical scatter within the analyzed time frame and the digitization error of 15 eV:

$$\Delta T_{\mathrm{rad,dat}} = \sqrt{\left(7\,\%\,T_{\mathrm{rad,dat}}\right)^2 + \left(\frac{T_{\mathrm{rad,dat}}}{f_{\mathrm{SNR}}}\right)^2 + \sigma^2 + (15\,\mathrm{eV})^2 + \left(100\,\%\,T_{\mathrm{rad,mod}}^{1\mathrm{O}}\right)^2}. \qquad (3.29)$$

The latter was introduced to account for uncertainties that might arise in the low intensity edge channels since the current data acquisition system did not allow optimized gain settings, but used a fixed gain for every channel.

A priori information Additionally to the prior information of former standard IDA application mentioned in section 3.3, two prior PDFs were included that penalize high electron temperature values in the SOL (default: $T_{\mathrm{e}}(\rho > 1.02) \not> 50\,\mathrm{eV}$) and outside the first vessel wall (default: $T_{\mathrm{e}}(\rho > \rho_{\mathrm{W}}) \not> 2\,\mathrm{eV}$). The latter acted like an outer boundary for the extrapolation in the region with omitted or without ECE data. The SOL prior was sometimes necessary to avoid bifurcation in the modelling of the 'shine-through' peak.

It will be shown in section 3.7 that the 'shine-through' peak could not only be modelled by radiation shining through from the hotter plasma edge region alone, but also with an additional contribution from very hot electrons located in the SOL. The suppression of the latter solution was justified assuming a typical ASDEX Upgrade separatrix temperature of $T_\mathrm{e,sep} = 100\,\mathrm{eV}$ and power decay length of $\lambda_q = 3\,\mathrm{mm}$ [87] which resulted in an electron temperature decay length of $\lambda_{T_\mathrm{e}} \approx 10\,\mathrm{mm}$ according to Spitzer-Härm conductivity and even less in the flux-limited model for parallel heat conduction [88] and, therefore, in an electron temperature $T_\mathrm{e}(\rho > 1.02) < 37\,\mathrm{eV}$.

Computational time Regarding its computational time, the ECFM code was not yet optimized for routine analysis. Each calculation of the complete radiation temperature profile — which means more or less solving (3.23) for all $\mathrm{N_{ch}} = 60$ ECE channels with default values of $\mathrm{N}_\nu = 3$ and $\mathrm{N}_r = 1$ — took approximately 0.13 s. This value was increased by several orders of magnitude within the optimization process and error analysis of IDA such that the time consumption of a complete IDA run for one time point was in the order of 10 min. The most time consuming part of the forward model was given by the calculation of the emission shape function (3.19) which was done $\mathrm{N_{ch}} \times \mathrm{N}_\nu \times \mathrm{N_r} \times \mathrm{N_s} = 1.8 \times 10^5$ times. Due to the linear dependence of the computational time on N_ν and N_r and their weak influence on the results (cf. section 3.7) only a small number of frequency and ray discretizations were used for standard analysis. This finding demonstrated the importance of the new analytical formula for the emission profile which accelerated its calculation by orders of magnitude.

3.5 Edge electron temperature profiles in H-mode

Since the H-mode serves as baseline scenario for fusion power plants and at the same time exhibits — with its steep edge gradients — the strong need for a sophisticated ECE analysis like ECFM to obtain reliable edge electron temperatures, the results of an arbitrary ASDEX Upgrade standard H-mode discharge #25804 and an H-mode discharge with strongly pronounced 'shine-through' peak #23417 are presented exemplarily. Both discharges were performed with plasma current of $I_\mathrm{P} = 1.0\,\mathrm{MA}$ and toroidal magnetic field $B_\mathrm{t} = -2.5\,\mathrm{T}$. Discharge #25804 was heated with $P = 9.1\,\mathrm{MW}$ and exhibited a central electron density $n_\mathrm{e,0} = 8.4 \times 10^{19}\,\mathrm{m^{-3}}$ at the analyzed time point $t = 2.06\,\mathrm{s}$. The total heating power and central density of discharge #23417 at $t = 3.47\,\mathrm{s}$ were lower with $P = 6.6\,\mathrm{MW}$ and $n_\mathrm{e,0} = 8.0 \times 10^{19}\,\mathrm{m^{-3}}$.

Fig. 3.6 (a) and (e) show the edge electron temperature profiles (red lines) obtained via ECFM analysis. Displayed by red pluses are the corresponding modelled radiation temperature values at the positions of their cold resonances. For both discharges they agreed very well with the ECE measurements (black crosses) up to the near SOL region — including the 'shine-through' peak.

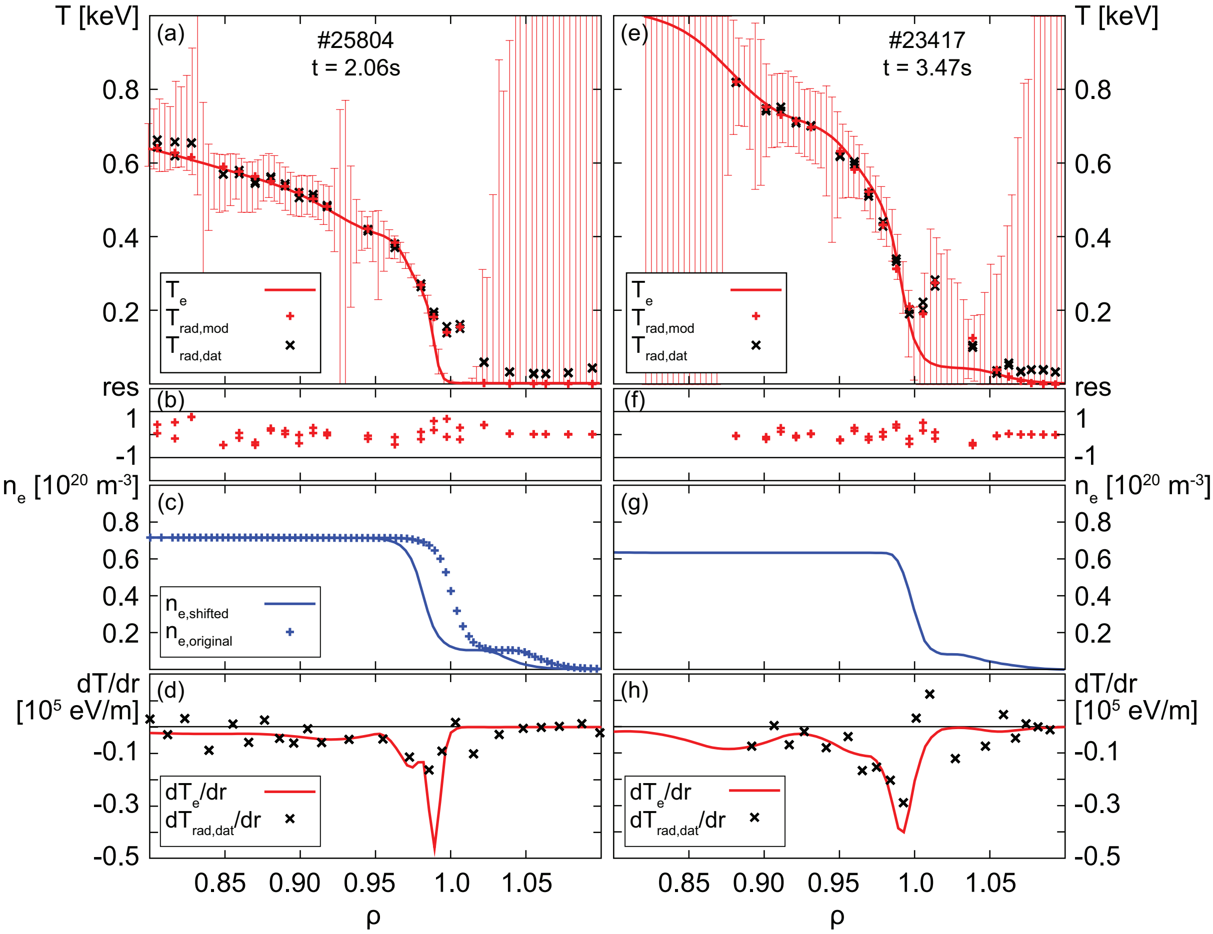

Figure 3.6: (a,e) Edge T_e profiles (red lines) together with the modelled (red pluses) and measured (black crosses) T_rad values at the positions of their cold resonance, (b,f) their residuals, (c,g) the applied (line) and original (pluses) n_e profile and (d,h) the gradients of T_e (red lines) and T_rad (black crosses) of discharge #25804 at $t = 2.06\,\mathrm{s}$ (left) and #23417 at $t = 3.47\,\mathrm{s}$ (right).

The consistency between modelled and measured data was also reflected in the residuals $\mathrm{res}_{\mathrm{i,j}} = \left(T_{\mathrm{rad,ECE}}(i,j) - T_{\mathrm{rad,mod}}(i)\right)/\Delta T_{\mathrm{rad,ECE}}(i,j)$ — stating the deviance between the modelled and measured values weighted by the measurement uncertainties. All residual values in Fig. 3.6 (b) and (f) lay between ±1 which means that the modelled values matched the measurement within its uncertainty. Outside of $\rho = 1.02$ for #25804 and $\rho = 1.05$ for #23417 the ECE data was assumed to contain a significant amount of 1st harmonic O-mode contributions and, therefore, was omitted in the analysis and its uncertainty set to a very large value. This caused residual values close to zero. The large error bars at $\rho \approx 0.83$ and $\rho \approx 0.93$ in Fig. 3.6 (a) and at $\rho < 0.87$ in (e) arose from the large gap between the measured data while for $\rho > 1$ in (e) they demonstrated that the ECE measurement did not contain sufficient information for a precise estimation of the electron temperature in the SOL. The explanation for this will be given in the next section.

Panels (c) and (g) additionally depict the electron density used for the forward modelling (solid lines). For ECFM analysis of discharge #25804 the electron density profile was shifted according to the separatrix condition mentioned in section 3.4.

The most important observation for the electron temperature results was their increased steepness compared to the radiation temperature and, therefore, also compared to the electron temperature results from 'classical' analysis. For discharge #25804 the maximal electron temperature gradient was more then two times higher than the radiation temperature gradient (cf. Fig. 3.6 (d)), for discharge #23417 the maximum of the electron temperature gradient exceeded the maximum of the radiation temperature gradient by around 40 % (cf. Fig. 3.6 (h)).

3.6 Radiation temperature versus electron temperature

The scope of this section is to explain the large deviations between the electron and radiation temperature and their gradients at the edge and in the SOL. In the following it is shown qualitatively and quantitatively — for different regions with characteristic plasma conditions regarding optical depth and gradient strength — how the radiation temperature behaves compared to the electron temperature at its cold resonance position. Therefore, the emission and absorption profiles and the radiation transport of three representative ECE channels with cold resonances marked by vertical black lines in Fig. 3.7 are described in detail.

Optically thick and low gradient plasma region For discharge #25804 the ECE channel with central frequency of $\nu_\mathrm{ECE} = 110.4\,\mathrm{GHz}$ had its cold resonance at $\rho = 0.96$. In this region of high electron density and temperature, already after a short ray path, the whole emitted radiation (blue, solid in Fig. 3.7 (b)) was fully re-absorbed (green, dashed) and the electron cyclotron intensity (red, solid) reached black-body level (black, dashed). At the same time, the high re-absorption narrowed the region in which the actual measured radiation has been emitted (filled range). The determination of the actual emission region was done by back-integration of the radiation transport from the antenna towards the plasma centre until the modelled radiation intensity was reached. In this case of high optical depth and low gradients the actually viewed region was located around the position of the cold resonance and exhibited only small changes in electron density and temperature. Under these conditions, the modelled radiation temperature (red plus in Fig. 3.7 (a)) matched the electron temperature (red line) at the cold resonance position of the measured frequency at $\rho = 0.96$ as predicted by the 'classical' ECE analysis described in section 3.1. The same behaviour was observed for the ECE channel with central frequency of $\nu_\mathrm{ECE} = 114.4\,\mathrm{GHz}$ of discharge #23417 (cf. Fig. 3.7 (f)).

Optically thick and high gradient plasma region The cold resonance positions of frequencies $\nu_\mathrm{ECE} = 109.8\,\mathrm{GHz}$ (#25804) and $\nu_\mathrm{ECE} = 112.9\,\mathrm{GHz}$ (#23417) illustrated in Fig. 3.7 (c) and (g) were located near the pedestal top where the plasma was still optically

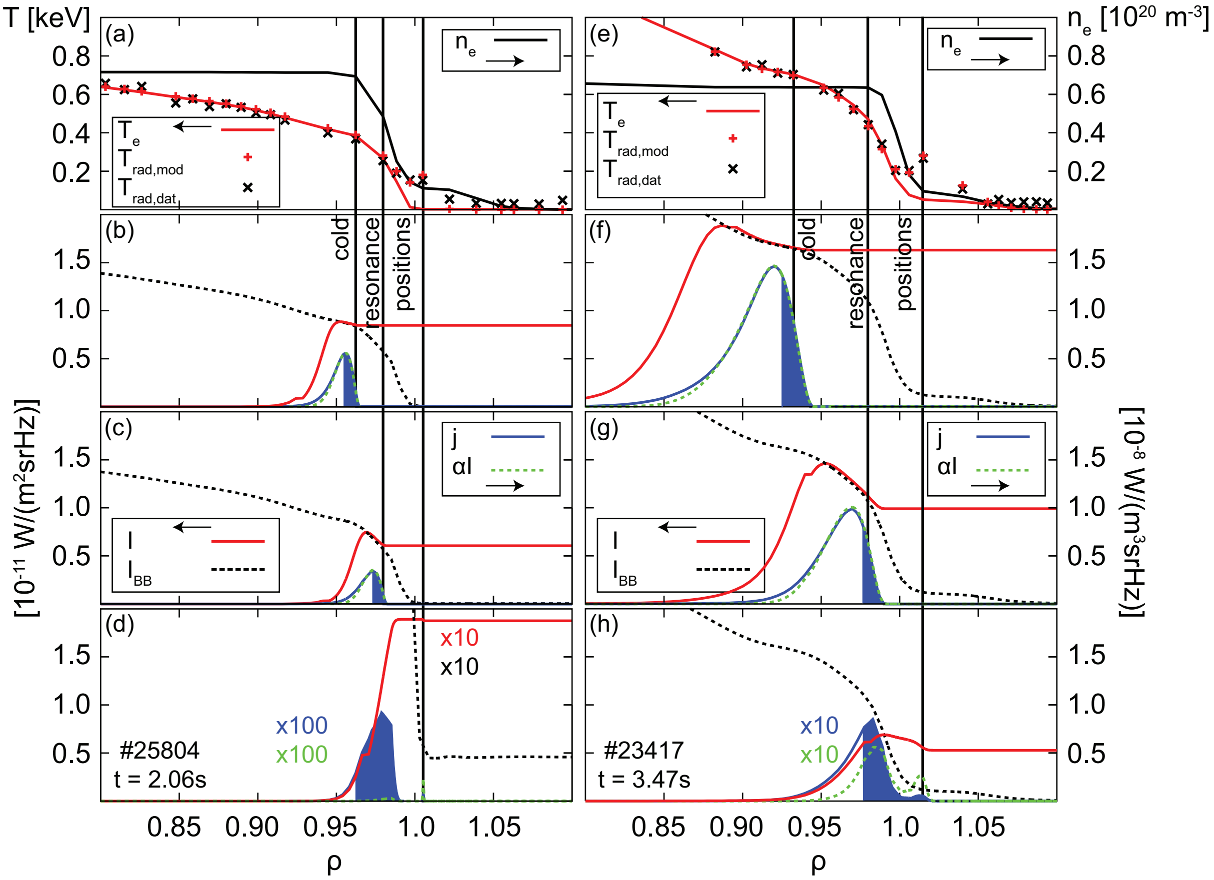

Figure 3.7: (a,e) Edge T_{e} profiles (red lines) together with the modelled (red pluses) and measured (black crosses) T_{rad} values at the positions of their cold resonance and the applied n_{e} profiles (black lines). Line integrated radiation (red, solid) and black-body intensity (black, dashed) together with the corresponding emission (blue, solid) and absorption (green, dashed) profiles of ECE channel with mean frequency (b) $\nu_{ECE} = 110.4\,\mathrm{GHz}$, (c) $\nu_{ECE} = 109.8\,\mathrm{GHz}$, (d) $\nu_{ECE} = 108.9\,\mathrm{GHz}$, (f) $\nu_{ECE} = 114.4\,\mathrm{GHz}$, (g) $\nu_{ECE} = 112.9\,\mathrm{GHz}$ and (h) $\nu_{ECE} = 111.8\,\mathrm{GHz}$, with their marked cold resonance positions (vertical black lines) and actual emission origins (filled blue range) for discharge #25804 at $t = 2.06\,\mathrm{s}$ (left) and #23417 at $t = 3.47\,\mathrm{s}$ (right).

thick but close to the steep edge. Again, the high absorption assured radiation at black-body level and a narrow emission region around the cold resonance position. However, the emission region reached the steep gradient area with large variation in the radiation level. In case of discharge #25804 the main contribution to the antenna intensity came from slightly inside the cold resonance position which resulted in a radiation temperature higher than the electron temperature at the cold resonance position. In case of discharge #23417 the main emission origin was shifted slightly outwards into regions with rapidly falling electron density and temperature which resulted in a radiation temperature smaller than the electron temperature at the cold resonance position.

Optically thin and high gradient plasma region The resonance regions of the ECE channels with central frequencies $\nu_{\mathrm{ECE}} = 108.9\,\mathrm{GHz}$ (#25804) and $\nu_{\mathrm{ECE}} = 111.8\,\mathrm{GHz}$ (#23417) were optically thin (incomplete re-absorption) and the observation areas remained rather broad (Fig. 3.7 (d) and (h)). In fact, the main contribution of the measured radiation was emitted far inside the cold resonance position in the much hotter edge gradient region which caused a radiation temperature that greatly exceeded the actual electron temperature at its cold resonance position — the ‘shine-through’ peak.

This also explained the large uncertainty of the SOL electron temperature in Fig. 3.6 (e). The radiation contribution from the SOL was too low as to provide significant information on the local electron temperature. However, since the ‘shine-through’ peak contained information about the edge gradient region it allowed to reduce the uncertainty of the electron temperature in this very important region. The low error bars around the separatrix in Fig. 3.6 (a) did not indicate that the informational content from this area was larger than for discharge #23417 because its emission contribution was also negligible. However, larger SOL electron temperatures would have increased the absorption such that the ‘shine-through’ peak could not have been modelled anymore. This might be an indication for an overestimated electron density.

Fig. 3.8 delivers the quantitative deviation between radiation and electron temperature depending on the optical depth and the gradient strength. It shows for every ECE channel the total width of the emission origin contributing to the measured intensity ΔR_origin (a) and the relative difference between radiation and electron temperature $(T_\mathrm{rad} - T_\mathrm{e})/T_\mathrm{e}$ (b) versus the optical depth. Furthermore, the relative difference between radiation and electron temperature is plotted against the electron temperature gradient length $L_{T_\mathrm{e}} = T_\mathrm{e}/\nabla T_\mathrm{e}$ (c). The blue dots represent the data of an L-mode discharge, the red squares correspond to an H-mode discharge. For the filled symbols, the electron temperature was higher than the radiation temperature.

In L-mode (blue) — due to lower density and temperature — the optical depth did not achieve values as high as in H-mode (cf. Fig. 3.8 (a)). Furthermore, the absence of strong gradients resulted in relatively weakly broadened ($\Delta R_\mathrm{origin} \approx 10\,\mathrm{mm}$)

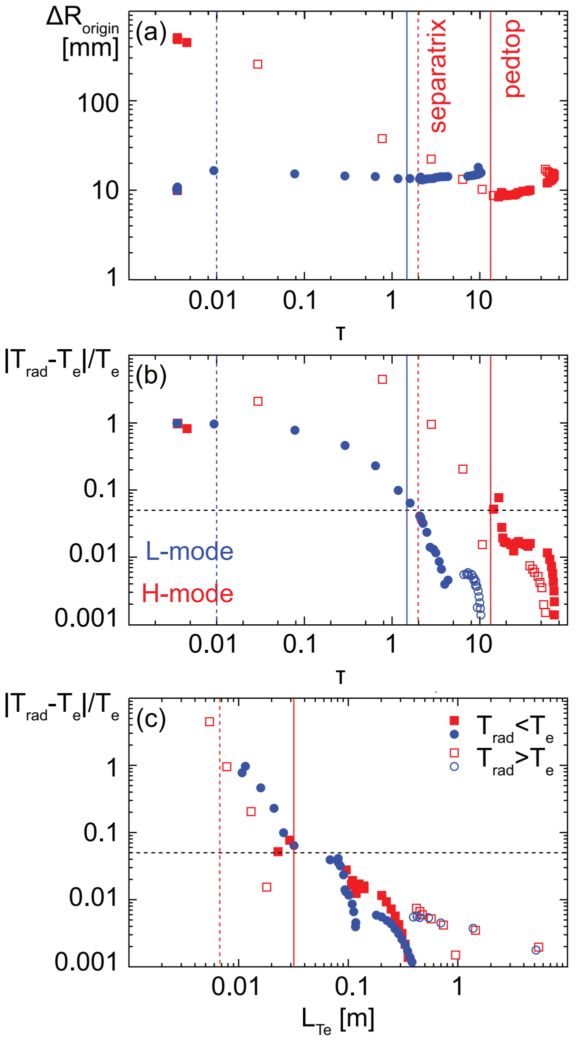

Figure 3.8: (a) ΔR_origin versus τ, (b) $(T_\mathrm{rad} - T_\mathrm{e})/T_\mathrm{e}$ versus τ, (c) $(T_\mathrm{rad} - T_\mathrm{e})/T_\mathrm{e}$ versus L_{T_e} in L-mode (blue) and H-mode (red); the vertical lines indicated the positions of the pedestal top (solid) and the separatrix (dashed).

emission profiles even for optically thin plasma. However, outside of the pedestal top (blue solid line in (b)), the radiation temperature deviated from the electron temperature by more than 5 % (black dashed line) up to 100 %. This was due to the low optical depth which caused emission far below the black-body level.

The H-mode discharge exhibited similarly broadened emission profiles in the main plasma. Yet, outside the separatrix (red dashed line in (a)) for optically thin plasma with $\tau \lesssim 1$, largely broadened profiles and, therefore, strongly de-localized emission origins from the cold resonance position were revealed. This was also reflected in the deviation between radiation and electron temperature (b) which was in the range of 100 % for optically thin plasma.

However, also in optically thicker plasma inside the separatrix, the radiation temperature of some channels exceeded the electron temperature by more than 5 % (black dashed line) up to 100 %. This was caused by the strong edge gradient which enabled radiation temperatures higher (towards separatrix) or lower (towards pedestal top) than the electron temperature even for slight shifts of the emission origin from the cold resonance position.

3.7 Sensitivity of the electron temperature results on input parameters

Due to non-linear physics (e.g. electron temperature and density dependence of the emission profile) and non-quantifiable sources of systematic uncertainties (e.g. wall reflections) of the different diagnostics, IDA incorporates high complexity and a large amount of degrees of freedom. This might cause non-transparent responses of the model to its inputs. This section is, therefore, dedicated to a detailed sensitivity study that was performed to demonstrate the influence of some model inputs on the ECFM output which on the one hand improved the understanding of the interaction between the model and its inputs and on the other hand allowed to narrow the area of validity of uncertain input parameters.

The numerical or physical origin of the respective behaviour was identified and objective criteria for proper selection of program settings were found. As a quantitative measure for the quality of the modelling χ^2 given by (3.27) or χ^2_n normalized on the number of ECE channels and the number of measurement points per analyzed time point were considered. It should be noted here, that — in contrast to considering statistically distributed uncertainties only — in this case, χ^2_n laid below 1 since systematic uncertainties were also taken into account. The dominant contribution to the uncertainty of the radiation temperature was given by a correlated uncertainty of 7 % on the data (cf. section 3.4) which strongly reduced χ^2_n. In addition, the inclusion of data points that were neglected in the analysis by a very large uncertainty caused a negligible contribution to χ^2 while

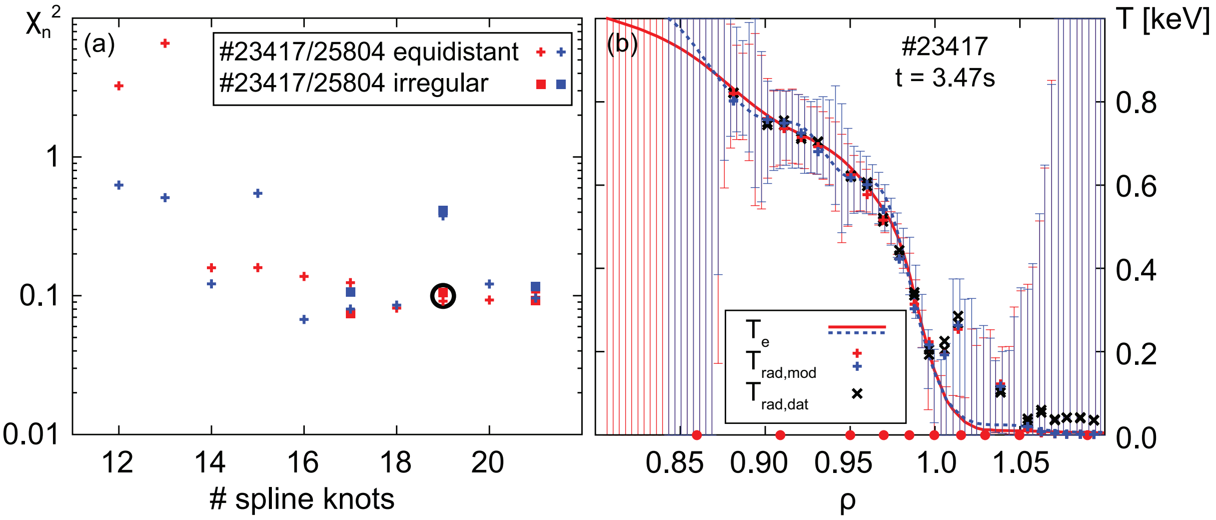

Figure 3.9: (a) Normalized χ^2 depending on the number of spline knots (equally (crosses) or irregularly (squares) distributed) for discharge #25804 at $t = 2.06\,\mathrm{s}$ (blue) and #23417 at $t = 3.47\,\mathrm{s}$ (red), results marked by black circles belong to profiles in (b). (b) Edge T_e profiles obtained with 19 irregularly (red solid line) and equally (blue dashed line) distributed spline knots (irregularly ones indicated by red circles) together with the modelled (red/blue pluses) and measured (black crosses) T_{rad} values at the positions of their cold resonance for discharge #23417 at $t = 3.47\,\mathrm{s}$.

they were still weighted and, therefore, reduced the normalized χ^2 further.

3.7.1 Sensitivity on the number of spline knots

The first sensitivity study accounted for the number and position of spline knots that were used to parameterize the electron temperature profile. In this investigation the nodes between $\rho = 0 - 0.8$ were kept fixed, while the number of nodes at the plasma edge was increased with either equidistant distribution (crosses in Fig. 3.9 (a)) or with decreasing step size (squares) towards the separatrix, the region of strongest changes.

According to the high χ^2_{n} values, less than 14 spline knots were not sufficient for reasonable modelling. On the other hand, any further increase of the node number did not influence χ^2_{n} strongly. Also the effect of equally or irregularly distributed nodes on χ^2_{n} was very small for discharge #23417. However, the resulting electron temperature profiles differed, as shown in Fig. 3.9 (b). They were each analyzed with 19 nodes but different node distribution. For both cases, the modelled radiation temperatures (red/blue pluses) were in good agreement with the measurement (black crosses). Yet, between $\rho = 0.85$ and $\rho = 0.98$ the electron temperature profile with equally distributed nodes (blue dashed line) exhibited some overshoots in the order of several %. This well-known phenomena of too much freedom in the spline is called 'ringing'.

3.7.2 Sensitivity on the electron density

Due to the linear electron density dependence of the emissivity (3.8), reasonable ECFM analysis relied on accurate knowledge about the complete electron density profile. The

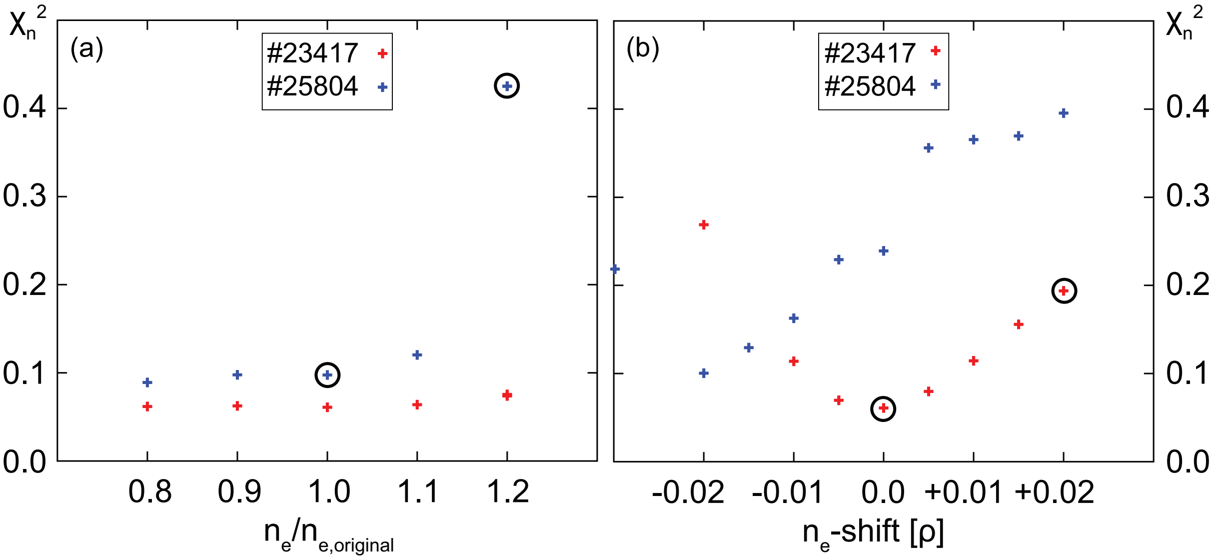

Figure 3.10: Normalized χ^2 depending on (a) the absolute values of n_e and on (b) the alignment of n_e and T_e for discharge #25804 at $t = 2.03\,\mathrm{s}$ (blue) and #23417 at $t = 3.47\,\mathrm{s}$ (red); results marked by black circles belong to profiles in Fig. 3.11.

joint analysis of electron density and temperature within the framework of IDA provided the best conditions to deal with the complementary information of these two quantities needed for ECFM. Nevertheless, electron density estimation is always accompanied by uncertainties in absolute value as well as position. Furthermore, the alignment between electron density and temperature profiles is exposed to uncertainties in the equilibrium reconstruction. The inclusion of the density uncertainties into the ECFM analysis would have greatly increased its complexity and was, therefore, omitted. Instead, the effect of density-scaling both in amplitude as well as position relative to the electron temperature profile on the electron temperature results was investigated in detail.

Absolute value Fig. 3.10 (a) displays χ_n^2 for varied electron density values between $0.8 \times n_\mathrm{e}$ and $1.2 \times n_\mathrm{e}$ which depicted the upper limit of 20 % uncertainty in the density reconstruction from LIB data. The effect on χ_n^2 was very small and also the modelled electron and radiation temperature values were nearly identical. The only outlier for discharge #25804 with increased electron density of 20 % (cf. blue dashed line in Fig. 3.11 (c)), resulted from the fact that the cut-off density (black crosses) was exceeded. In this case, the affected ECE channels were set to $T_\mathrm{rad,mod} = 0$ (cf. blue dots in Fig. 3.11 (a)) and omitted in the analysis by setting their uncertainties to a very large value. This caused a higher value for χ_n^2, even if the electron temperature (blue dashed line in (a)) and the residuals (blue in b) were very similar to the non-scaled (red) case.

Alignment In contrast to the weak influence of the absolute value, an accurate alignment of the electron density profile with the electron temperature profile was of great importance. This can be seen from Fig. 3.10 (b) where χ_n^2 is plotted against the electron

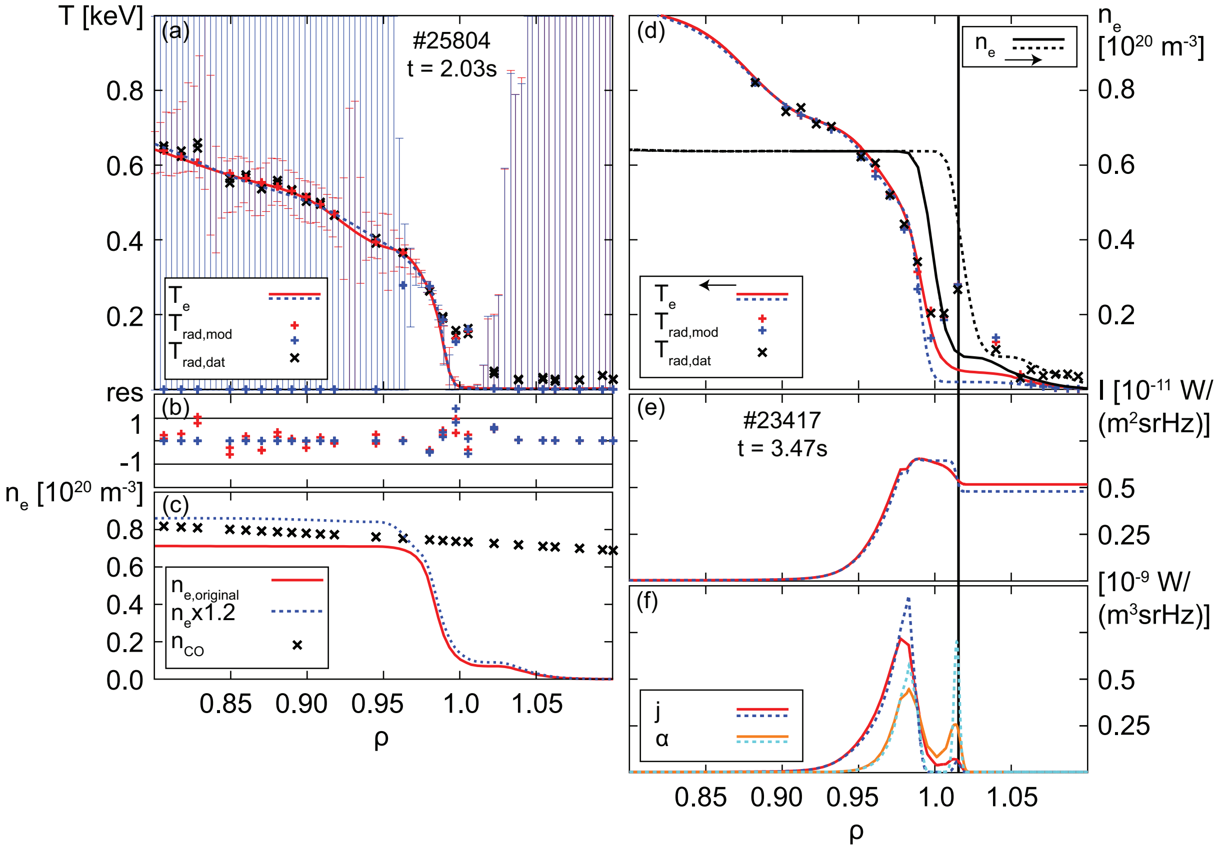

Figure 3.11: Left: (a) Edge T_{e} profiles (red/blue lines) together with the modelled (red/blue pluses) and measured (black crosses) T_{rad} values at the positions of their cold resonance, (b) their residuals and (c) the applied original (red line) and increased (blue line) n_{e} profile together with the cut-off density (black crosses) of discharge #25804 at $t = 2.03\,\mathrm{s}$. Right: (d) Edge T_{e} profiles (red/blue lines) together with the modelled (red/blue pluses) and measured (black crosses) T_{rad} values at the positions of their cold resonance and the original (black solid line) and the shifted (black dashed line) n_{e} profile, (e) the line integrated radiation intensities and (f) the corresponding emission (red/blue lines) the absorption (orange/light blue lines) profiles of ECE channel with mean frequency $\nu_{ECE} = 111.8\,\mathrm{GHz}$ for discharge #23417 at $t = 3.47\,\mathrm{s}$.

density shift. Shifts up to $\Delta\rho \pm 0.02$ (+ outwards/ − inwards), which corresponded to $\Delta R \approx \pm 10\,\mathrm{mm}$, seemed to be reasonable within the uncertainties. For both analyzed discharges χ^2_{n} exhibited a clear minimum. While for discharge #23417 the original electron density and temperature profiles were perfectly aligned, the density of #25804 needed to be shifted towards the temperature profile by $\Delta\rho = -0.02$ to achieve the best modelling results.

The effect of the profile alignment is shown on the right side of Fig. 3.11 where the electron density and temperature profiles (d), the line integrated radiation intensities (e) and the corresponding emission and absorption profiles (f) for ECE channel with mean frequency $\nu_{ECE} = 111.8\,\mathrm{GHz}$ are compared for different applied densities — results obtained with the original electron density profile (black solid line in (d)) are represented by reddish solid lines, results obtained with the outward shifted electron density profile (black dashed line in (d)) are represented by bluish dashed lines. The shift resulted in

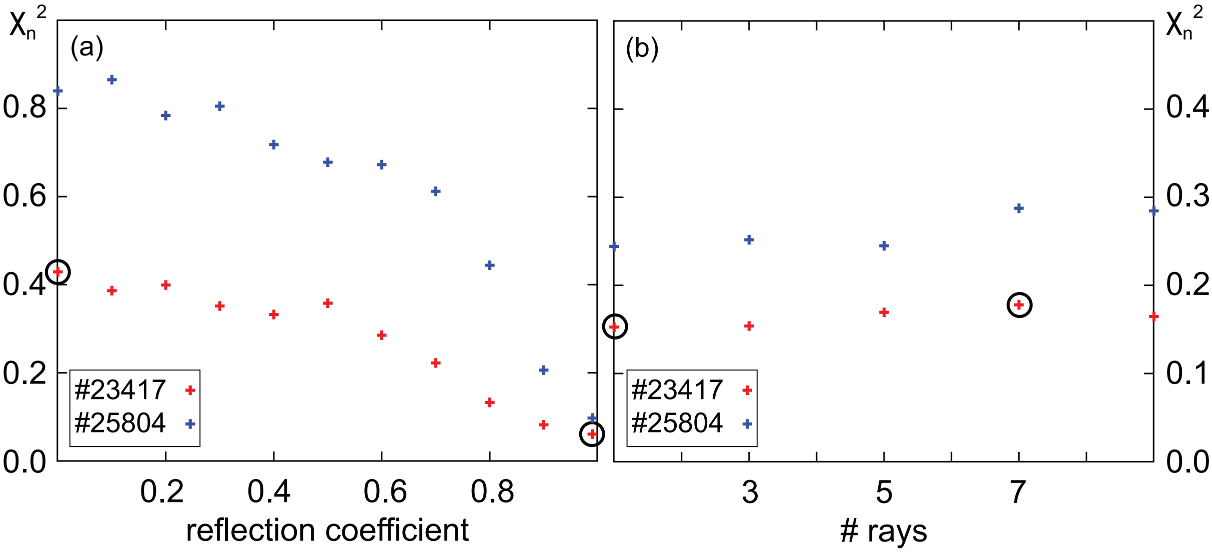

Figure 3.12: Normalized χ^2 depending on (a) the reflection coefficient and on (b) the number of rays for discharge #25804 at $t = 2.03\,\mathrm{s}$ (blue) and #23417 at $t = 3.47\,\mathrm{s}$ (red); results marked by black circles belong to profiles in Fig. 3.13.

a much higher electron density at the cold resonance position (vertical line at $\rho \approx 1.02$) of the selected ECE channel. At this point, the absorption (light blue dashed line in (f)) was, therefore, strongly increased compared to the original case (orange, solid). To match the ECE measurement anyway, the absorption was reduced in the region around the separatrix ($\rho = 0.99$–1.01) by a decrease in the electron temperature. However, these lower electron temperatures led to a misfit between measured (black crosses in (d)) and modelled (blue pluses) radiation temperatures for the two ECE channels slightly inside the separatrix.

3.7.3 Sensitivity on the reflection coefficient

In optically thin plasma regions multiple ray passes due to reflections increased the measured intensity as described in section 3.4. Unfortunately, an exact modelling with known reflection coefficients was not possible because of the complicated wall structures and resulting diffusive scattering. Instead, a simplified model (3.28) with a parameterized reflection coefficient was used for ECFM analysis.

The dependency of χ^2_n on this reflection coefficient is shown in Fig. 3.12 (a). For both discharges, the modelling with highest reflection close to 100 % delivered the best result. For the tungsten coated walls of ASDEX Upgrade this value was reasonable.

To illustrate the effect of reflections on the radiation intensity, the results for the ECE channel with central frequency of $\nu_{ECE} = 111.8\,\mathrm{GHz}$ of discharge #23417 obtained with high reflection coefficient ($R = 0.99$, reddish solid lines on the left-hand side of Fig. 3.13) were compared to the results obtained without considering reflections (bluish dashed lines). In both cases, the modelled radiation temperature (red/blue pluses in (a))

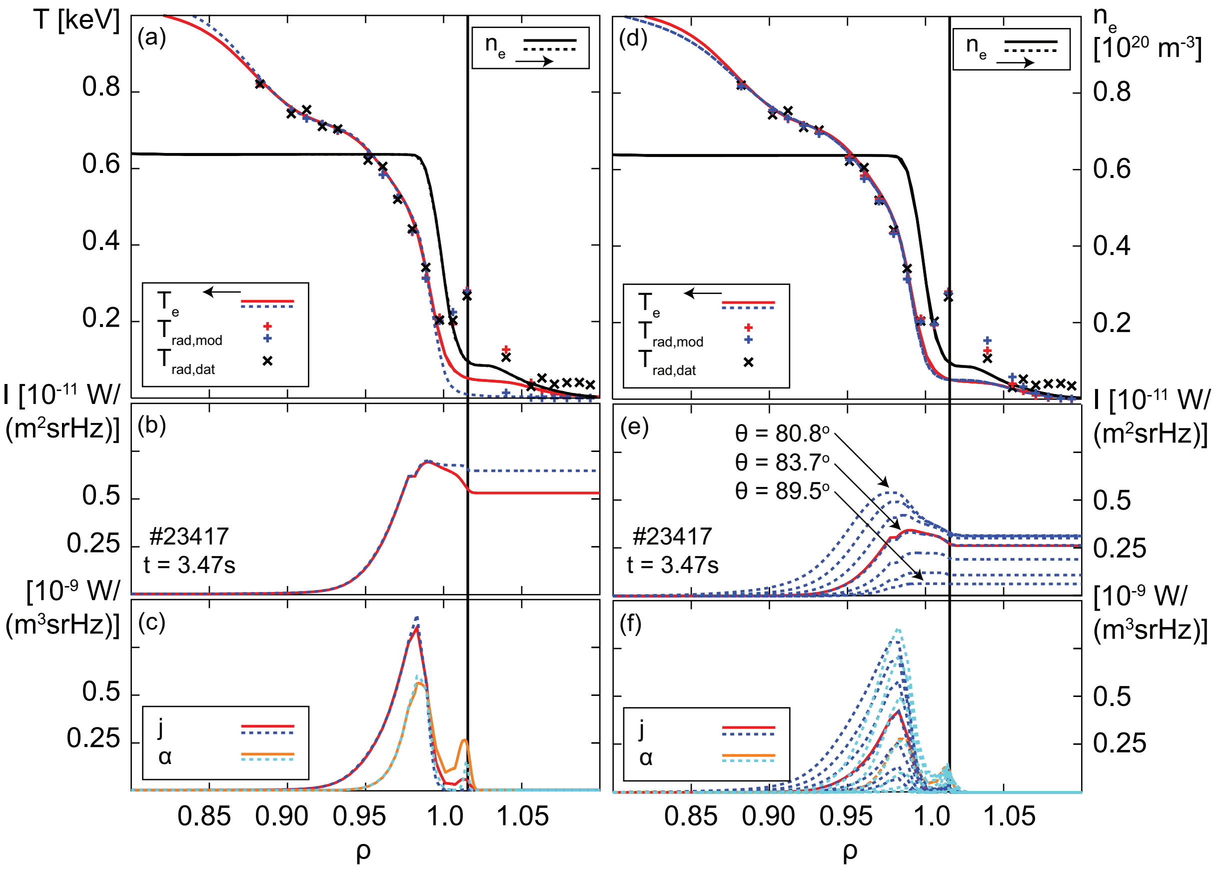

Figure 3.13: (a,d) Edge T_e profiles with (left) applied reflection of $R = 0.99$ (red solid line) and without reflection (blue dashed line) and (right) one ray (red solid line) and seven rays (blue dashed line) together with the modelled (red/blue pluses) and measured (black crosses) T_rad values at the positions of their cold resonance and the applied n_e profile (black line), (b,e) the line integrated radiation intensities (red/blue lines) and (c,f) the corresponding emission (red/blue lines) and absorption (orange/light blue lines) profiles of ECE channel with mean frequency $\nu_{ECE} = 111.8\,\mathrm{GHz}$ for the only central ray (red line in f) and for all seven (unweighted) rays (blue line in f) for discharge #23417 at $t = 3.47\,\mathrm{s}$.

for the selected ECE channel matched the measurement (black dot) perfectly. Without reflections, it was directly given by the single-pass intensity (blue dashed line in (b)). With reflections the single-pass intensity (red solid line in (b)) was smaller, but reached the same antenna intensity by multiple ray passes. The deviation in the single-pass intensity was produced by a higher electron temperature (red solid line in (a)) slightly before and at the cold resonance position which caused enhanced absorption (orange solid line in (e)) in this region.

3.7.4 Sensitivity on the antenna pattern

ECFM analysis incorporated the possibility to account for the finite antenna pattern (cf. section 3.4). The desired number of rays for the discretization of the viewing beam had to be defined in the input file. As already stated, for standard analysis only the central ray was considered, because the computational time increased linearly with the number of rays. This simplification was justified by the small variations in χ^2_n for different ray numbers (cf. Fig. 3.12 (b)) and the negligible deviations in the resulting profiles on the right-hand side of Fig. 3.13.

This plot compares the results obtained with the central ray only (reddish, solid) and with seven rays (bluish, dashed). The electron and modelled radiation temperatures in Fig. 3.13 (d) and the line integrated intensities (e), emission and absorption (f) profiles for the central rays were almost identical. The emission and absorption profiles of the other rays, seeing the plasma with another angle, of course differed. Nevertheless, the sum of all rays nearly caused the same result as the central ray. Note here, that the plotted profiles were not yet weighted which means that the actual contributions of the decentral rays were much smaller. An interesting observation was that the ray which was closest to perpendicular viewing exhibited the lowest emission. This was due to the fact, that its shape function was less shifted inwards, because of less Doppler broadening, to hotter and denser plasma regions.

3.7.5 Sensitivity on restrictions of the SOL temperature

As already mentioned in section 3.4, there might occur a bifurcation in the modelling of the ‘shine-through’ peak. Fig. 3.14 (a) shows the temperature results analyzed with the same data set (black crosses) with (red) and without (blue) the application of the SOL prior which penalizes electron temperature values greater than 50 eV outside of $\rho = 1.02$.

From the agreement of both modelled radiation temperature values (red/blue pluses in (a)) with the measurement of the ECE channel with $\nu_{ECE} = 108.4\,\text{GHz}$ (marked by the vertical black line) it can be seen that the ‘shine-through’ peak could be reproduced either by emission from hotter plasma regions far inside the cold resonance position only (filled red range in (c)) or by a dominant contribution from even further inside and an additional smaller local contribution (filled blue range in (c)). Both emission profiles were causing a similar final intensity (b). The first solution originated from an electron temper-

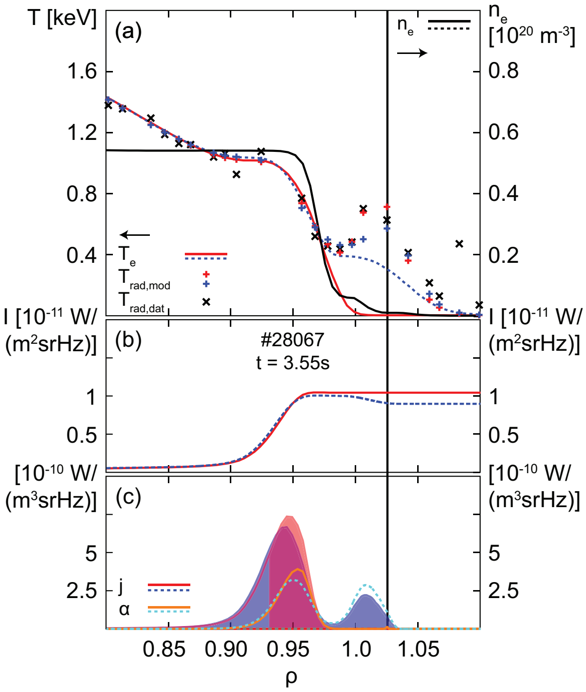

Figure 3.14: (a) Edge T_e profiles with (red) and without (blue) applied SOL prior together with the modelled (red/blue pluses) and measured (black crosses) T_{rad} values at the positions of their cold resonance and the applied n_e profile (black lines), (b) the line integrated radiation intensities (red/blue) and (c) the corresponding emission (red/blue lines) and absorption (orange/light blue lines) profiles of the ECE channel with mean frequency $\nu_{ECE} = 108.4\,\text{GHz}$ for discharge #28067 at $t = 3.55\,\text{s}$.

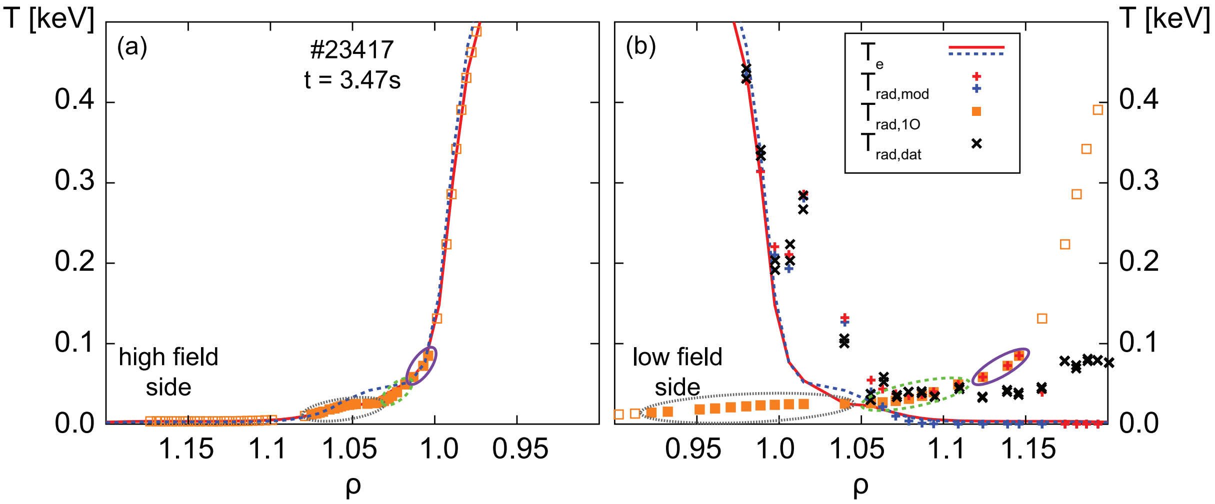

Figure 3.15: (a) High-field side and (b) low-field side edge T_e profiles obtained with (red line) and without (blue line) contribution of the 1st harmonic O-mode together with the total modelled (red/blue pluses) and measured (black crosses) T_rad values and the used (filled orange squares) and not used (empty orange squares) $T_\mathrm{rad,1O}$ values at their actual cold resonance positions (a) and the cold resonance position of the 2nd harmonic (b) for discharge #23417 at $t = 3.47\,\mathrm{s}$.

ature profile with very small SOL values (red line in (a)). The second solution which was slightly preferable in terms of χ^2 minimization — if not suppressed by the SOL prior — exhibited much higher local electron temperatures (blue line in (a)). However, such high SOL electron temperatures were not reasonable as argued in section 3.4 and, therefore, the suppression of the second solution by the SOL prior was justified.

3.7.6 Sensitivity on 1st harmonic O-mode contributions

The last issue of the sensitivity study is dedicated to possible O-mode emission contributing to the measured antenna intensity (cf. section 3.4).

The ECFM code contained the possibilities not to consider 1st harmonic O-mode contributions at all, to consider them only by an additional error (cf. (3.29)) or to really account for them — without initiating additional parameter values — within the calculation of the radiation temperature as described above.

Fig. 3.15 shows for discharge #23417 the results of ECFM analysis which includes 1st harmonic O-mode contributions for the radiation temperature calculation (red) compared to the standard analysis where 1st harmonic O-mode contributions were only treated as an additional measurement uncertainty (blue). The plotted lines illustrate the resulting electron temperature profiles at the low-field side (right) and its reflection to the high-field side (left) assuming temperature conservation on flux surfaces. The corresponding total modelled radiation temperatures, containing contributions from 2nd harmonic X-mode and the 1st harmonic O-mode (red pluses) or the 2nd harmonic X-mode only (blue pluses), are mapped to the cold resonance position of the 2nd harmonic X-mode. The fraction of 1st harmonic O-mode radiation for the first case is additionally shown by orange squares —

mapped to the cold resonance position of the 2$^{\text{nd}}$ harmonic X-mode on the right side and to its actual cold resonance position at the high-field side (left). The empty symbols hereby mark the frequencies that are either resonant outside the vessel walls or within the cut-off region and, therefore, omitted in model.

The influence of the contributions from 1$^{\text{st}}$ harmonic O-mode radiation within the ECFM analysis on the electron temperature results behaved differently depending on the location of their origin on the high-field side and their dedicated location on the low-field side. The three outermost (low-field side) channels considering 1$^{\text{st}}$ harmonic O-mode contributions (marked by the purple solid ellipse) exhibited a considerable amount of O-mode contributions, while they did not measure 2$^{\text{nd}}$ harmonic X-mode contributions at all. Nevertheless, their mismatch with the measured radiation temperature (black crosses) demonstrated that these channels did not affect the electron temperature formation, since the region of their origin ($\rho \approx 1.0$) was well-defined by 2$^{\text{nd}}$ harmonic X-mode radiation. The fact that the modelled data exceeded the measurement was not remarkable since optically thick radiation and complete reflection and mode conversion was assumed which was probably strongly overestimated.

The seven channels further inside (marked by the green dashed ellipse) were still dominated by 1$^{\text{st}}$ harmonic O-mode contributions and actually did influence the result by decreasing the electron temperature from $\rho = 1.02$ on (compared to the blue dashed electron temperature profile).

The innermost channels considering 1$^{\text{st}}$ harmonic O-mode contributions (marked by the grey dotted ellipse) were strongly dominated by 2$^{\text{nd}}$ harmonic X-mode radiation which implicated that the influence of 1$^{\text{st}}$ harmonic O-mode contributions within the main plasma, the edge and the near SOL region on the electron temperature result was negligible.

3.8 Validation and limitations of the method

The purpose of this section is to validate the ECFM method by demonstrating that it was possible to reconstruct artificial electron density and temperature profiles from the synthetic radiation temperature and by checking the consistency of the electron temperature results with other diagnostics. Furthermore, the limitations of the method are discussed.

3.8.1 Reconstruction of artificial data

To verify the reliability of the ECFM method, it is shown that using simulated radiation temperatures from artificial electron density and temperature profiles reproduced the initial electron temperature profile.

The artificial electron temperature and density profiles that reflected typical H-mode conditions are given by black lines in Fig. 3.16 (a) and (c). Modelling the radiation transport for these artificial profiles delivered the synthetic ECE data $T_{\text{rad,dat}}$ (black dots in (a)).

The application of ECFM within the optimization process of IDA resulted in the red profile for the electron temperature and the red dots for the modelled radiation temperature. The consistency of the red and black electron temperature profiles revealed that ECFM was able to reproduce the artificial input profile within the error bars.

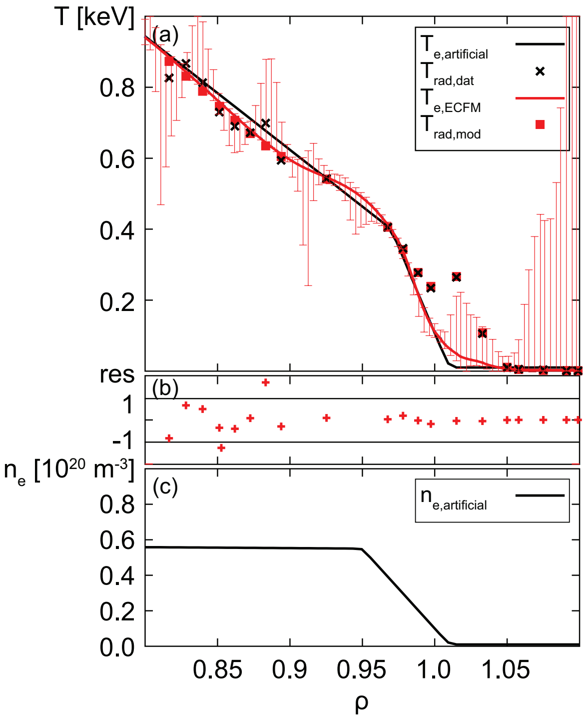

Figure 3.16: (a) Artificial (black line) and with ECFM analysis reproduced (red line) edge T_e profiles together with the simulated (black crosses) and the modelled (red boxes) T_{rad} values at the positions of their cold resonance, (b) their residuals and (c) the artificial n_e profile.

3.8.2 Comparison with other diagnostics

Depending on the plasma region, there are different methods available at ASDEX Upgrade to get information about the electron temperature (cf. appendix A). Thomson Scattering spectroscopy (TS) delivers kinetic data for the core and the edge gradient region. From Langmuir probe measurements one can obtain kinetic profiles in the SOL.

Despite its lower temporal and spatial resolution compared to the ECE measurement, TS diagnostic exhibits the advantage of measuring the electron temperature and density simultaneously and, therefore, delivers important information about the alignment of the profiles.

The left-hand side of Fig. 3.17 shows the electron temperature (a) and density (c) results obtained via ECFM/IDA analysis (red/blue line) compared to the TS data (green circles) for discharge #24161. After shifting the TS profiles 7 mm (#24161) outwards, both, electron temperature and density profiles agreed very well. The shifts were reasonable within the spatial resolution of TS and the uncertainties in the equilibrium reconstruction which acted differently on the spatially fixed TS measurement and the magnetic-field dependent localization of the ECE measurement.

The Langmuir probes which can only measure in cold plasma regions deliver electron temperature results in the SOL or in case of an L-mode discharge even up to slightly inside the separatrix. Like TS diagnostics they measure the electron temperature as well as the density, but usually with different probes.

The results of the Langmuir probes on the midplane manipulator for L-mode discharge #24111 [89] are shown as green circles on the right-hand side of Fig. 3.17. Without any

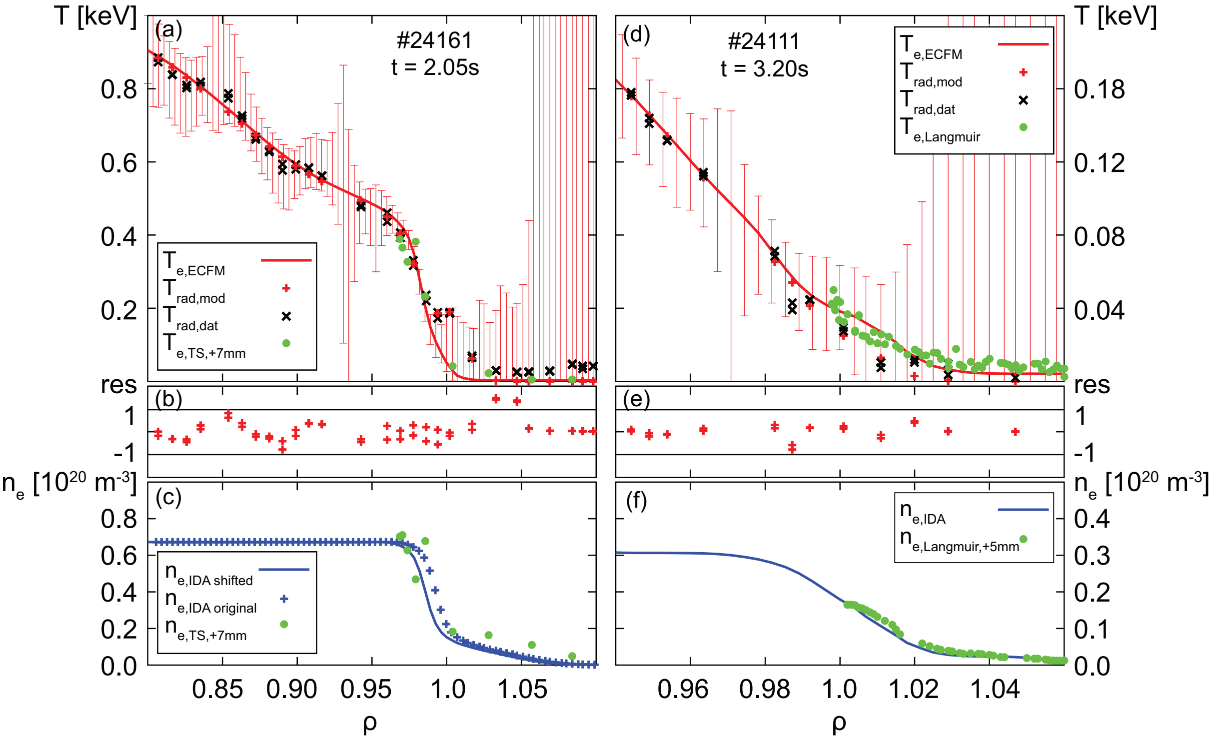

Figure 3.17: (a,d) Edge T_e profiles from ECFM analysis (red line) and TS (a) or Langmuir probes (d) (green circles) together with the modelled (red pluses) and measured (black crosses) T_{rad} values at the positions of their cold resonance, (b,e) their residuals and (c,f) the applied (blue line) and original (blue pluses) LIB and TS (a) or Langmuir probe (d) (green circles) n_e profiles of discharge #24161 at $t = 2.04\,$s (left) and discharge #24111 at $t = 3.20\,$s (right).

shift, the electron temperature (d) profile agreed very well with the ECFM result (red line). However, it should be noted that the significance of the electron temperature data from ECE in the SOL was rather low. Outside a certain radius (here: $\rho \gtrsim 1.02$), the fraction of 1st harmonic O-mode contributing to the measured radiation intensity was assumed to dominate over radiation emitted in the 2nd harmonic X-mode and, therefore, the affected ECE channels were omitted in the analysis. This is reflected by the large error bars. The profile in this region was mainly fixed by the wall prior which restricted the electron temperature to values lower than 2 eV at the first wall, as described in section 3.4. It is interesting to note here, that — contrary to H-mode discharges — the radiation temperatures for frequencies with cold resonance around the separatrix were below the electron temperature (cf. section 3.6).

3.8.3 Electron temperature in the scrape-off layer

As already indicated in section 3.5, measurements of the electron cyclotron radiation are not sensitive to the electron temperature in the near SOL.

This is demonstrated in Fig. 3.18 where the influence of varying the SOL decay length of the electron temperature (coloured dashed lines) compared to the original ECFM result (red solid line, $\lambda_{T_e} \approx 5\,$mm) on the resulting radiation temperature (coloured pluses) was investigated. The steepest SOL profile (blue) thereby corresponded to a decay length of $\lambda_{T_e} \approx 0.5\,\mathrm{mm}$, the flattest SOL profile (green) to $\lambda_{T_e} \approx 20\,\mathrm{mm}$. The small variation of the modelled radiation temperatures compared to scatter in the measurement (black crosses) indicated that it was not possible to resolve these differences in the decay length with ECE. The electron temperature decay length obtained via the power decay length according to (6) in [87] was assumed to lie between $\lambda_{T_e} \approx 8.6\,\mathrm{mm}$ (Spitzer-Härm model) and $\lambda_{T_e} \approx 3.7\,\mathrm{mm}$ (limited-flux model).

Again, the electron temperature profile resulting from ECFM analysis (red line) outside of $\rho = 1.02$ was set by the wall prior. In between this position and the separatrix the shape was determined by the curvature prior which favoured the least curved profile.

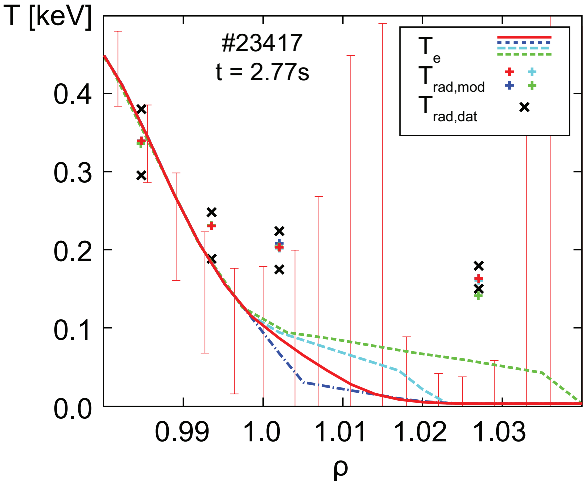

Figure 3.18: Edge T_e profiles from ECFM analysis (red line) and with different artificially created decay length (coloured lines) together with the modelled (coloured pluses) and measured (black crosses) T_{rad} values at the positions of their cold resonance of discharge #23417 at $t = 2.77\,\mathrm{s}$.

3.8.4 Extreme case

To test the ECFM method under extreme conditions, an improved H-mode discharge with strong heating and rather low density was analyzed. This produced very high central electron temperatures ($\lesssim 10\,\mathrm{keV}$) and as a consequence of their long Maxwell tail and the absence of any cut-offs — due to the low density — also a very high ‘shine-through’ peak ($\lesssim 8\,\mathrm{keV}$) as shown in Fig. 3.19 (a,d).

The analysis was done once with considering all ECE channels (left-hand side) and once without considering the channels outside $\rho = 1.02$ (right-hand side). The central electron temperature dominated the local radiation temperature as well as the ‘shine-through’ temperature and did not have a solution that modelled both regions correctly at the same time.

In the case that all channels were considered (left-hand side), the SOL channels dictated the modelling of the centre because of their higher number compared to the central channels. This caused an electron temperature profile (red line in (a)), that could reproduce the ‘shine-through’ peak quite well, but underestimated the central temperature.

The better solution probably was the one on the right-hand side where the SOL channels were omitted in the analysis. The mismatch between the modelled (red pluses in (d)) and the measured (black crosses) data for the SOL channels probably occurred due to the lacking consideration of refraction within ECFM. Regarding straight LOS,

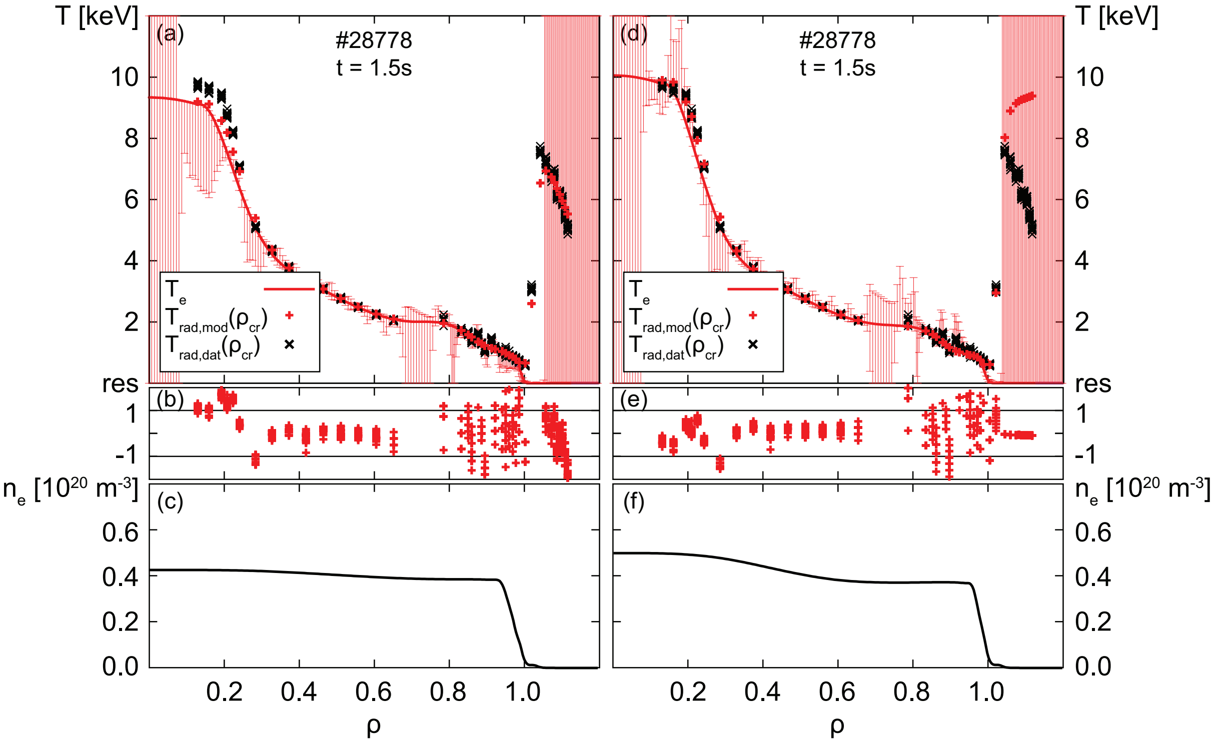

Figure 3.19: (a,d) Edge T_e profiles (red lines) considering all ECE channels (a) and only ECE channels with cold resonance inside $\rho = 1.02$ (d) together with the modelled (red pluses) and measured (black crosses) T_{rad} values at the positions of their cold resonance, (b,e) their residuals and (c,f) the n_e profile of discharge #28778 at $t = 1.45\,\mathrm{s}$.

the model assumed the innermost and the outermost channels to view the same electron density and temperature profiles, because the vertical positions and the absolute angles towards the torus of the corresponding antennae (red and blue in Fig. 3.3) were the same. However, since they measured at different frequencies, possible refraction would have deflected the low-frequency rays stronger than the high-frequency rays. The edge channels would, therefore, have seen a slightly colder plasma region and exhibited reduced radiation temperatures compared to the modelling with straight lines.

Nevertheless, independent of the incompleteness of the model due to neglecting possible refraction, it was important to see that even such high 'shine-through' peaks could be modelled with the assumption of Maxwellian electrons. However, it is shown in the following that this was not always the case.

3.8.5 Non-Maxwellian electron distribution

The profiles in Fig. 3.20 depict the electron temperature (a) and density (b) of a discharge with strong electron heating at very low density which was assumed to exhibit a non-thermal electron distribution. This was supported by the large discrepancies between the ECE data (black dots in (a)) and the TS data (blue) outside $\rho = 0.6$. In red, the ECFM results for the electron (line) and radiation (dots) temperature are plotted. It can be seen that neither in the centre nor outside $\rho = 0.85$ the measured radiation temperature could be modelled correctly which delivered an additional hint for a non-Maxwellian electron distribution. The (reasonable) decay of electron temperature at the edge — which is in contrast increasing radiation temperature — was caused by the priors for the SOL and wall temperatures.

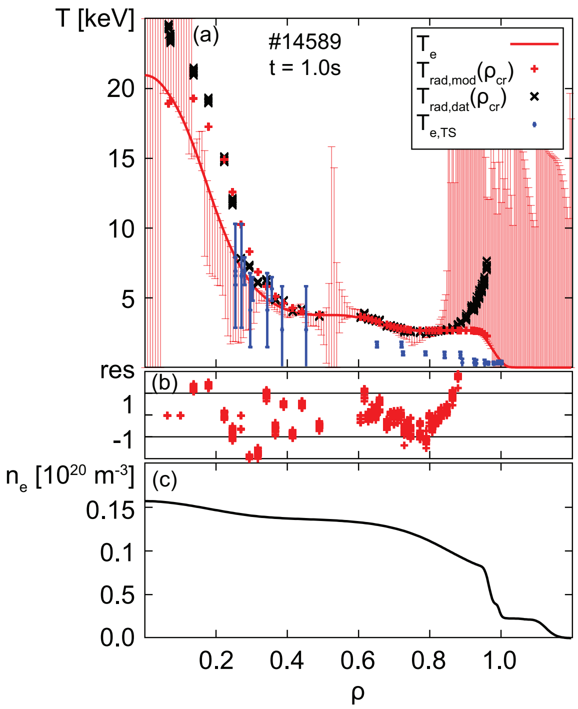

Figure 3.20: (a) T_e profiles from ECFM (red lines) and TS (blue dots) together with the modelled (red pluses) and measured (black crosses) T_rad values at the positions of their cold resonance, (b) their residuals and (c) the n_e profile of discharge #14589 at $t = 1.0\,\mathrm{s}$.

3.9 Discussion

A method has been presented to obtain reliable edge electron temperature profiles from ECE data by forward modelling of the radiation transport. Previous 'classical' ECE analysis was not able to exploit the information given by measurements with frequencies resonant in optically thin plasma regions. Hence, its resulting edge gradients mostly relied on extrapolations [24]. The integration of the newly developed ECFM code into the preexisting IDA routine now enables to apply ECE measurements for the estimation of accurate electron temperature profiles and gradients at the plasma edge.

The most important observation related to the electron temperature results from ECFM analysis is that the H-mode edge gradients are actually steeper than the 'classical' ECE analysis would predict. As expected, the electron temperature around the separatrix and in the near SOL is — in H-modes — generally lower than the radiation temperature because radiation from hotter plasma regions is shining through. Furthermore, already in the optically thick gradient and pedestal top region, the radiation temperature can deviate from the electron temperature at the cold resonance position — in both directions — due to the finite width of the emission region (cf. Fig. 3.8). This implies that the electron temperature gradients obtained with 'classical' ECE analysis can differ significantly from the actual value — despite careful handling of the ECE data with respect to the optical depth. Errors in the temperature are directly reflected in the pressure which is a key player for pedestal physics like edge stability. Therefore, studies based on 'classical' ECE analysis might lead to misinterpretations of edge phenomena.

The reliability of the model is reflected in the residuals. Moreover, electron temperature profiles resulting from ECFM analysis are consistent with those from TS at the pedestal top and in edge gradient region and with those from Langmuir probe measurements around the separatrix.

Another important result is that the ‘shine-through’ peak can be quantitatively reproduced by ECFM analysis. This phenomenon has been unresolved for a long time and was believed to have non-thermal origins [26, 27]. However, according to recent results from JET [90], the down-shifted emission of thermal electrons in the H-mode edge gradient region can be strong enough to match the cold resonance frequencies of the SOL. Furthermore, due to the low optical depth in the SOL, their emitted radiation actually reaches the antenna. This finding is confirmed by the results from ECFM analysis, which is also based on a Maxwellian electron distribution. It can even be extended by the observation of a huge ‘shine-through’ peak for frequencies with cold resonance in the SOL that are shifted up to the plasma centre.

Nevertheless, it has been demonstrated that a discharge which is supposed to have a dominant non-thermal electron distribution can not be modelled with ECFM (cf. Fig. 3.20). This discovery might allow the exclusion of non-thermal electrons in cases where ECFM analysis delivers reasonable results. To enable also the modelling of discharges with non-thermal electrons, (3.9) would have to be extended by a non-Maxwellian distribution function and might not possess an analytic solution anymore. This would result in an increased computational effort. Furthermore, if the electrons are becoming relativistic, the whole formalism sketched in section 3.1 which is based on a weakly relativistic plasma is no longer valid, but consideration of a fully relativistic plasma is needed. Another reasonable extension of the ECFM analysis is the inclusion of refraction via a ray tracing method. An indication that this might be necessary for a more reliable estimation of the central electron temperature is given by Fig. 3.19. The limitation of the electron temperature estimation to the region inside the separatrix can not be abolished by the model. It is intrinsically given by the lack of information from the H-mode SOL region which is covered by the stronger emission from the edge gradient region. On the other hand, this effect enhances the resolution of the electron temperature gradient.

The detailed sensitivity study has allowed to validate the variable program settings and input parameters. Investigations on the influence of the number and position of spline knots on the electron temperature results suggest to apply a sufficiently large node number close to the separatrix to be able to resolve the strong gradient, but a rather small number in regions of little changes to avoid ‘ringing’. Therefore, 21 spline knots with decreasing step size towards the separatrix are used for standard analysis.

Related to the sensitivity on the electron density, it has been observed that the electron temperature results hardly react on variations of the absolute density within its uncertainty range. However, an accurate alignment of electron density and temperature profiles is crucial because the steepness of the electron temperature edge gradient is very sensitive to the profile alignment. On the other hand, the increase of χ^2_n shows that it is not possible to fully compensate an inaccurate electron density position by adapting the electron temperature profile. This means that the method delivers the possibility to estimate the actual relative shift between the ECE and LIB diagnostic from the quality of the fit to the data. Density shifts up to 10 mm can be necessary to enable a good modelling. However, these shifts are justified within the radial resolution of LIB and the uncertainties in equilibrium reconstruction. Furthermore, the observations concerning the best alignment of the kinetic profiles are consistent with the findings in [85].

According to the investigations on the wall reflections, the modelling usually works best for almost total reflection. Like the density alignment, the value of the reflection coefficient strongly influences the resulting electron temperature edge gradients. Admittedly, the actual coefficient used for the analysis — which is either chosen manually or selected automatically by the model to enable the best fit to the data — is not based on any physical model or measurement. However, reflections close to 100 %, as suggested by the sensitivity study, seem to be reasonable for a tungsten coated wall and small deviations from that do not influence the result significantly.

The finite antenna pattern has been found to have a negligible effect on the result, while it strongly increases the computational effort. Therefore, only the central channel is considered for standard analysis. However, the inclusion of several rays might be crucial for the application of a ray tracing code.

An important parameter for reliable modelling is the SOL prior to get rid of the bifurcation of either very low or very high electron temperatures in the SOL. However, the suppression of the latter solution is justified and the strength of its penalization is weaker than physical restrictions (cf. section 3.4).

As discussed in section 3.4 it is not possible to set up a proper model for possible contributions from 1^{st} harmonic O-mode. However, results obtained with the simple approach described in section 3.4 showed that it is justified to consider all ECE data with cold resonance within $\rho = 1.05$ because the influence of 1^{st} harmonic O-mode contributions within the main plasma, the edge and the near SOL region on the electron temperature result is negligible. Furthermore, it is quite likely that the feature of relatively high and even increasing intensity measured for channels with cold resonance outside $\rho \approx 1.05$ can be explained by contributions from 1^{st} harmonic O-mode.

The occurrence of the ‘shine-through’ peak should not prevent the use of the ECE measurement as a suitable diagnostic for edge analysis. In fact, it really poses a chance. First, because it contains important information about the edge electron temperature gradient. Second, the existence of the ‘shine-through’ is not itself the reason for the failure of the ‘classical’ ECE analysis but only the evidence that the optically thick approach fails in any case in the edge region and that one really needs an appropriate model for the electron cyclotron radiation transport and reliable density profiles for well-grounded studies of plasma edge physics based on ECE data.

4 Edge kinetic data in ELMy H-modes with magnetic perturbations

(Parts of this work are published in: Rathgeber S K *et al* 2012 In *39th EPS Conference on Plasma Physics (Stockholm, Sweden)* **36F** P5.059)

The application of non-axisymmetric Magnetic Perturbation (MP) fields at the plasma edge has proven to successfully mitigate type-I Edge Localized Modes (ELMs). The underlying mechanism is, however, still unknown. Since ELMs are supposedly driven by the edge pressure gradient, this chapter focuses on the effect of MPs on the electron edge kinetic profiles and gradients and their relation to the present ELM type.

The results shown in the first three sections are restricted to three dedicated discharges. Their design and overall behaviour are outlined in section 4.1. In section 4.2, the edge kinetic profiles at some characteristic time points of the different ELM regimes are presented. This is followed by the examination of the temporal evolution of the edge pressure gradient in section 4.3. Whether the different ELM types can be distinguished by their associated altered edge parameters is studied in section 4.4 with the aid of several discharges that exhibited significant variation in plasma parameters. The relation between the edge kinetic data and the ELM type is concretized by the investigation of the onset of ELM mitigation under various conditions in section 4.5. The chapter ends with a discussion of all the results with regard to the different hypotheses for ELM mitigation via MPs stated in section 2.2.

4.1 Discharge description

To investigate the effect of MPs on the edge pressure gradient, three identical discharges with different application of MPs have been performed — one with resonant $n = 2$ perturbation (#28847), one with non-resonant $n = 2$ perturbation (#28850) and the reference discharge without MPs (#28848). The colour coding of data with resonant MPs indicated in shades of red, data with non-resonant MPs in shades of blue and data without MPs in shades of grey is applied throughout this whole chapter apart from section 4.5. In all three discharges the same NBI heating power of $P_{\mathrm{NBI}} = 4.9\,\mathrm{MW}$ (Fig. 4.1 (a)), a plasma current of $I_{\mathrm{P}} = 800\,\mathrm{kA}$ and a toroidal magnetic field of $B_{\mathrm{T}} = -2.5\,\mathrm{T}$ was applied. In discharges #28847 and #28850, the MP-coils were operating at a constant current of $I_{\mathrm{MP}} \approx 1\,\mathrm{kA}$ throughout the whole analyzed period ($1.5-7.6\,\mathrm{s}$).

The gas puff (b) was ramped in two steps with different slopes. This strong variation enabled to achieve in all three discharges phases with type-I ELMs at the beginning, with small ELMs at higher densities — also without MPs due to the strong gas puff (cf. section 2.2) — and a slow transition phase with both types of ELMs in between. The

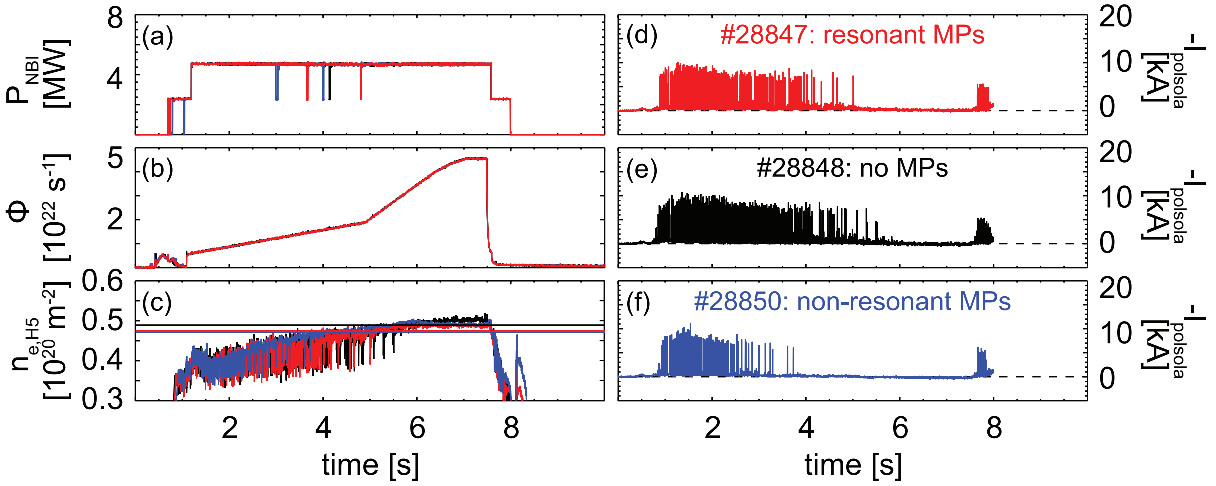

Figure 4.1: Time traces of (a) the NBI heating power, (b) the gas puff, (c) the line-averaged edge density and (d,e,f) the divertor current signals of discharge #28847 with resonant MPs (red), #28848 without MPs (black) and #28850 with non-resonant MPs (blue).

type-I ELMs can be identified by the large spikes in the divertor current in (d,e,f), the small ELMs caused fluctuations with strongly reduced amplitude. Complete type-I ELM suppression occurred earlier in the case with non-resonant than resonant MPs and latest without MPs. Yet, the line-averaged edge density $n_{\mathrm{e,H5}}$ (c) of the DCN interferometry 'H5' channel (cf. Fig. 3.3 and appendix A) shows that the threshold for the occurrence of the last type-I ELM (marked by the horizontal lines) was almost the same for both discharges with MPs and close to the experimental criterion stated in section 2.2, while it was slightly higher without MPs. In the fully mitigated regime, the density was the same in both perturbed discharges, but slightly lower compared to the reference.

4.2 Kinetic edge profiles

The effect of MPs on the electron edge kinetic profiles and relation of the latter to the occurring ELM type are visualized for some dedicated time points.

Fig. 4.2 and Fig. 4.3 each depict the electron edge kinetic profiles of discharge #28847 (left column, red), #28848 (middle column, black) and #28850 (right column, blue). From top to bottom the rows illustrate the electron temperature profiles (lines) together with the modelled (pluses) and the measured (crosses) radiation temperature values at the positions of their cold resonance, the residuals — indicating that the modelling worked well — and the electron density and pressure profiles.

All the density profiles have been shifted inwards within ECFM analysis (solid lines) as suggested by the separatrix criterion (cf. section 3.4). The original density profiles are additionally plotted as dotted lines. The fact that the shift tended to be stronger in the cases with MPs was consistent with the misalignment between the LIB and the equilibrium reconstruction caused by the separatrix deformation due to MPs [91]. Fig. B.1 and Fig. B.2 illustrate that the field line perturbation at the position of the LIB measurement

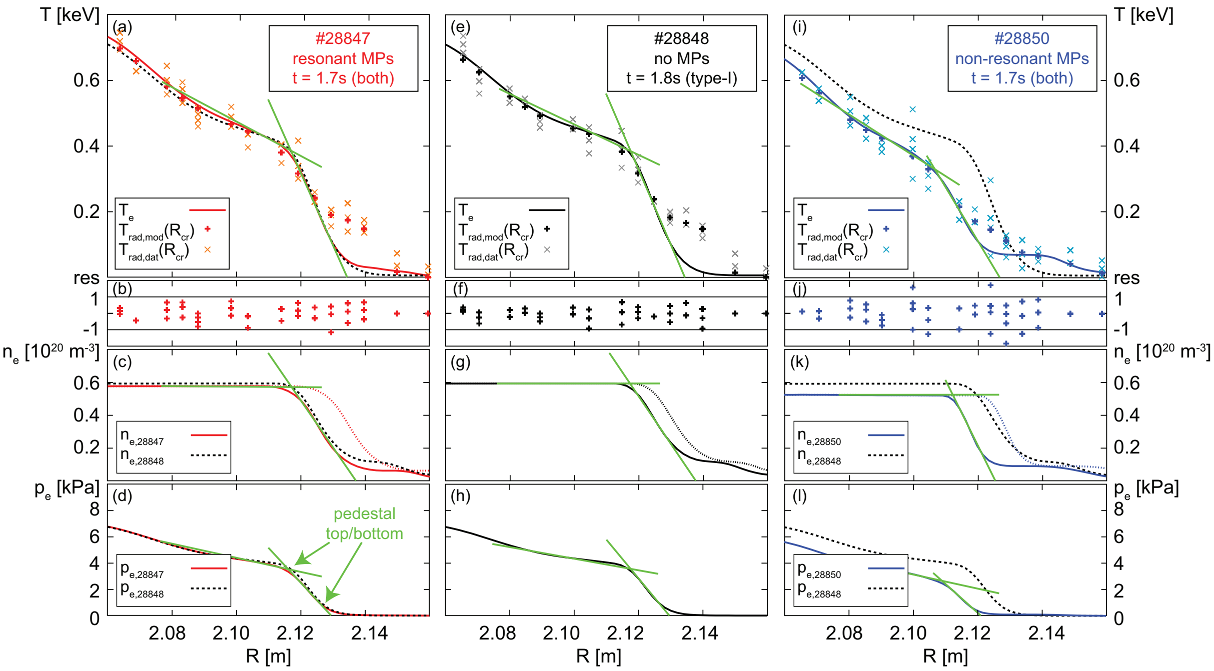

Figure 4.2: (a,e,i) Edge T_e profiles together with the modelled (pluses) and measured (crosses) T_{rad} values at the positions of their cold resonance, (b,f,j) their residuals, (c,g,k) the applied (solid) and original (dotted) n_e profiles and (d,h,l) the p_e profiles of discharge #28847 (left, red), #28848 (middle, black) and #28850 (right, blue) at $t = 1.7/1.8$ s; the black dashed lines in the left and the right column again show the profiles of discharge #28848 without MPs; the green lines additionally illustrate the application of the two-line fit.

was caused by MP-coils 5 and 6. Both of them possessed a positive coil current in these discharges which caused an outward bending of the field lines. Hence, by the equilibrium reconstruction — which relied on measurements at a different toroidal position — the LIB data was assigned to flux surfaces too far outside. This misalignment exhibited the same direction for the ECE reconstruction but was weaker, since the ECE diagnostics was located at the same toroidal position as the LIB diagnostic, but vertically further apart from the MP-coils. This justified an inward shift of the LIB data relative to the ECE data.

Fig. 4.2 shows the profiles at an early time point (1.7/1.8 s) which was dominated by type-I ELMs but exhibited also some small ELMs with applied MPs. To compare the profiles, the results of discharge #28848 are again plotted as black dashed lines in the left and right column. This revealed almost identical profiles for #28847 and #28848, with slightly smaller pedestal top values and gradients for the discharge with resonant MPs. The pressure gradient was reduced by about 10 %.

To the contrary, the edge kinetic profiles of discharge #28850 differed significantly. They were strongly shifted inwards — note here the use of the major radius R as abscissae —, exhibited significantly lower pedestal top values and reduced edge gradients of temperature and pressure ($\approx -40\,\%$) compared to the reference discharge. This indicated that type-I ELMs were not related to a fixed edge pressure gradient but occurred at very different values.

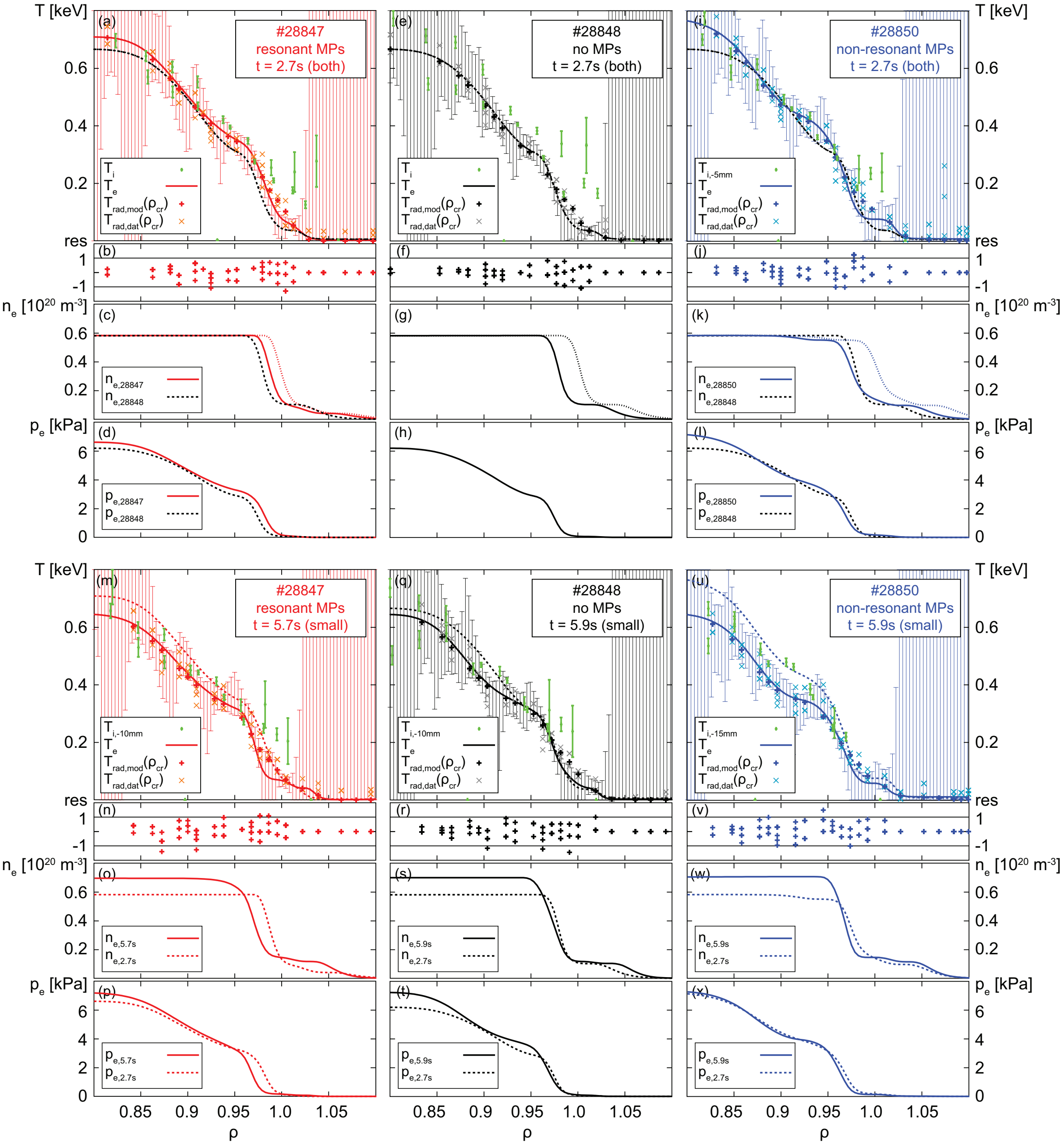

Figure 4.3: (a,e,i,m,q,u) Edge T_e (lines) and T_i (green dots) profiles together with the modelled (pluses) and measured (crosses) T_rad values at the positions of their cold resonance, (b,f,j,n,r,v) their residuals, (c,g,k,o,s,w) the applied (solid) and original (dotted) n_e profiles and (d,h,l,p,t,x) the p_e profiles of discharge #28847 (left, red), #28848 (middle, black) and #28850 (right, blue) at $t = 2.7\,\mathrm{s}$ (top row) and $t = 5.7\,\mathrm{s}$ (bottom row); the black dashed lines in the left and the right column of the top row again show the profiles of discharge #28848 without MPs; the dashed lines in the bottom row again show the profiles at $t = 2.7\,\mathrm{s}$.

Additionally shown in green in Fig. 4.2 are the results of the two-line fit — a least-squares fit that modelled the profiles between some cm inside the separatrix and the pedestal bottom by two straight lines. This enabled an automatic estimation of the pedestal top (point of minimal curvature) and bottom (point of maximal curvature) values and positions and the mean gradient between them. This information was used for the investigations presented in the next sections.

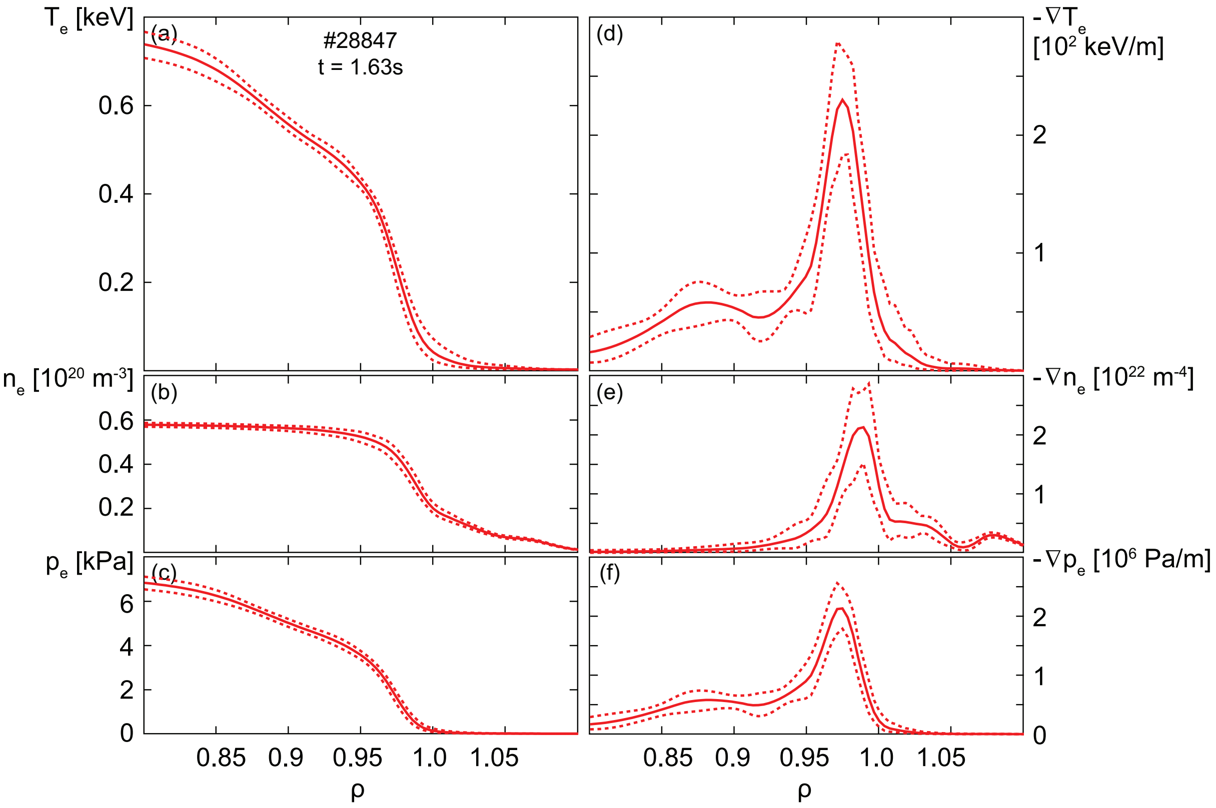

Figure 4.4: Edge profiles (solid) of (a) T_e, (b) n_e, (c) p_e, (d) ∇T_e, (e) ∇n_e and (f) ∇p_e with their upper and lower boundaries (dashed) given by MCMC calculations of discharge #28847 at $t = 1.67\,\mathrm{s}$.

At a later time point ($t = 2.7\,\mathrm{s}$) shown at the top of Fig. 4.3 — with strongly reduced type-I ELM frequency and small ELMs in between the remaining type-I ELMs in all three discharges — the edge pressure gradients of discharges #28847 and #28848 were significantly reduced compared to the previous time point. Neither the comparison of discharges #28847 and #28848 at the top left of Fig. 4.3 nor of discharges #28850 and #28848 at the top right revealed any significant difference in the edge kinetic profiles — apart from different density shifts.

These profiles are compared to the ones of a time point with fully suppressed type-I ELMs ($t = 5.7/5.9\,\mathrm{s}$) in all three discharges at the bottom of Fig. 4.3. The profiles of $t = 2.7\,\mathrm{s}$ are plotted as dashed lines, the ones of $t = 5.7/5.9\,\mathrm{s}$ as solid lines. At the later time point — due to the stronger gas puff — the pedestal top densities were higher in all three discharges. This also caused a temperature reduction at and inside the pedestal top — which was less pronounced in the reference discharge. Both these effects resulted in pressure profiles that were very similar to the previous ones.

The comparison of the electron temperatures with the ion temperatures (green dots) from CXRS measurements (cf. appendix A) demonstrated that the profiles were — apart from an inward shift of the ion temperatures of about $\Delta R \approx 10\,\mathrm{mm}$ in the later time points — almost the same.

All the error bars shown in the previous figures have been obtained via χ^2-binning method (cf. section 3.3) which exhibited the advantages of directly depicting the informational content of the measurement data and of being estimated with a reasonable computational effort. However, since it considered the neighbouring uncertainties as uncorrelated, it did not reveal the uncertainties of the gradients. The latter were provided by an error analysis via Markov Chain Monte Carlo (MCMC) calculations (cf. section 3.3). Due to its considerable higher computational effort, it has only been applied exemplarily for a few cases to get an idea about the uncertainties of the gradients. Shown in Fig. 4.4 are the profiles (left, solid) and the gradients (right, solid) obtained by MCMC calculations of the electron temperature (top row), density (middle row) and pressure (bottom row) together with their upper and lower uncertainty bands (dashed). For the quantities that were used for further studies, the uncertainties exhibited values of $\Delta n_{\mathrm{e,pedtop}} \approx 5\,\%$, $\Delta T_{\mathrm{e,pedtop}} \approx 5-10\,\%$ and $\Delta \nabla p_{\mathrm{e,mean}} \approx 40\,\%$.

4.3 Temporal evolution of the edge pressure gradient

To study the behaviour of the edge pressure gradient under different conditions and in the presence of different ELM types, the two-line fit — as described in the previous section — has been applied in several time frames of the three discharges. The mean edge pressure gradients are plotted in Fig. 4.5 (a,e,i,m) together with the divertor currents for four time intervals of each 50 ms.

The large gaps in the time traces of the pressure gradients originated from the lacking LIB data during chopped periods that were necessary for background signal subtraction (cf. appendix C). Smaller gaps also arose from time points that were not modelled correctly. These were automatically detected by checking the residuals.

The excursions in the mean pressure gradients (indicated by the red arrows in Fig. 4.5 (a)) were caused by the edge profile degradation during the ELMs — which was stronger for type-I than for small ELMs (marked up in Fig. 4.5 (g) and (o), respectively; note the different scale of the ordinate). After the ELM crashes, the pressure gradients recovered and tended to exhibit their maximal values shortly before the next one. However, as already mentioned in section 2.2, they generally reached their threshold values already several ms before the next ELM crash.

For the generation of average pressure gradients, allowing a quantitative comparison of different discharges and time frames, the reduced values during ELMs and the recovery phase had to be neglected and only the highest values some time before the next ELM had to be taken into account. These were at the same time the interesting ones for studying the stability threshold. However, an automatic detection of the small ELMs was — due to the small signal excursions — not possible. Therefore, the average of the upper 10 %-ile of the mean pressure gradient (named $\nabla p_{\mathrm{e,upper}}$) within time intervals of 200 ms was used which is indicated by the horizontal lines in Fig. 4.5.

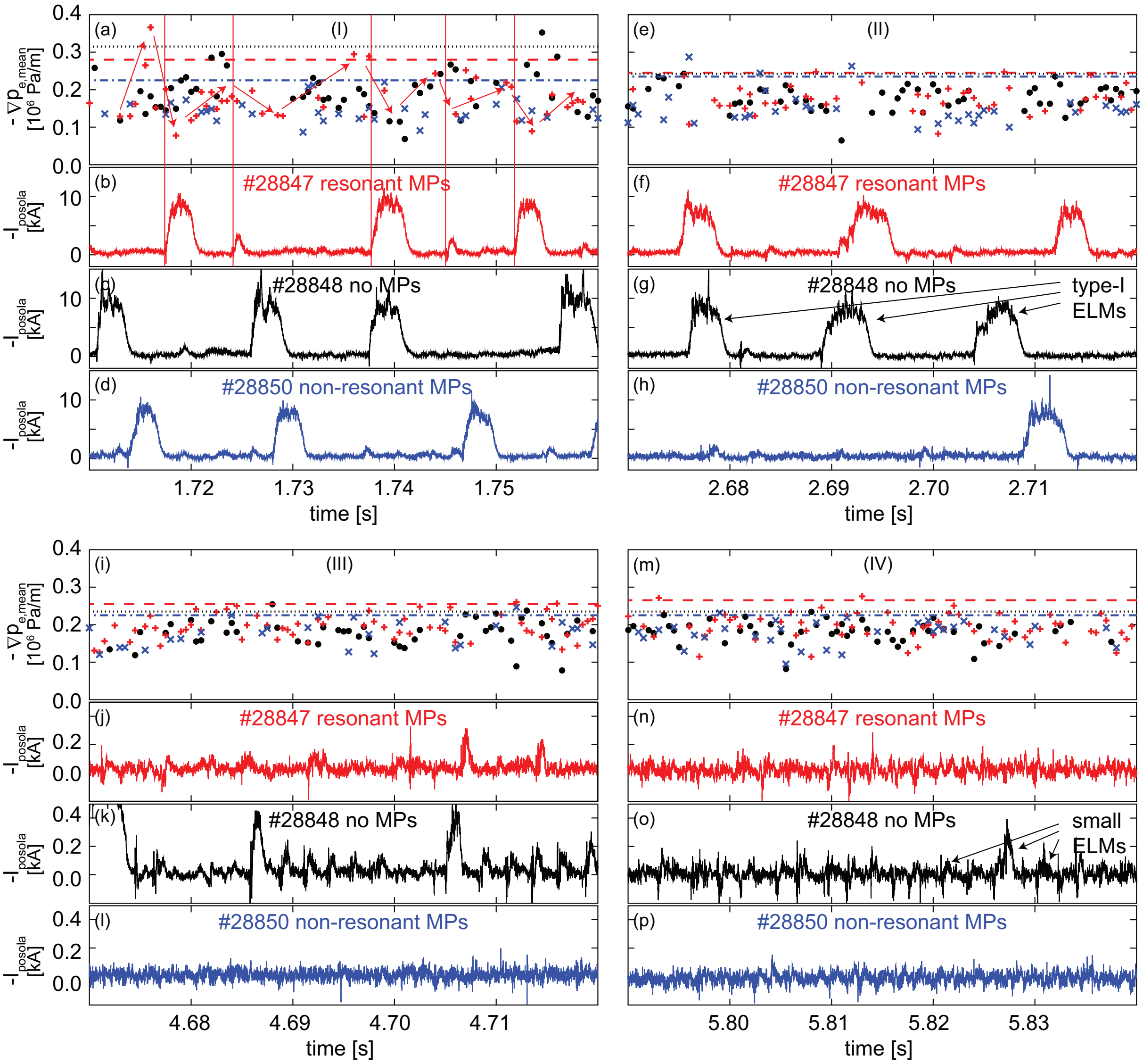

Figure 4.5: Time traces of the mean edge pressure gradients (a,e,i,m) of discharge #28847 (red pluses), #28848 (black circles) and #28850 (blue crosses) together with the corresponding divertor currents; the horizontal lines indicate the mean of the 10 % highest values.

Time slot (I) Discharge #28848 exhibited only type-I ELMs, while #28847 and #28850 were dominated by type-I ELMs but also some small ELMs occurred. Discharges #28848 and #28847 showed a very similar behaviour with significantly higher values of the pressure gradient before type-I than before small ELMs and with only slight difference (≈ 10 %) of the upper value (black dotted line versus red dashed line). Yet, the pressure gradients of discharge #28850 were strongly reduced and did not reveal a difference in the pre-type-I and pre-small ELMs values. The upper value of the pressure gradient (blue dash-dotted line) was with about 40 % significantly reduced compared to the one of #28848.

Time slot (II) Discharges #28847 and #28848 were dominated by type-I ELMs, while #28850 was dominated by small ELMs. The upper values of the pressure gradient were reduced in #28847 and #28848 compared to time slot (I) and reached similar values for all three discharges.

Time slot (III) Discharges #28847 and #28850 exhibited small ELMs only, while #28848 was dominated by small ELMs, but exhibited some type-I ELMs as well. Also the small ELMs showed larger excursion in the divertor current compared to the discharges with MPs. Again, the upper values of the pressure gradient were similar — at the low level of time slot (II) — for all three discharges.

Time slot (IV) All three discharges exhibited small ELMs only. Again the excursions in the divertor signal were the largest for #28848 and the smallest for #28850. The upper values of the pressure gradient were similar for discharges #28848 and #28850 and tended to be slightly higher for #28847.

4.4 Correlation of local edge parameters with ELM type

The previous findings — together with the results of several other discharges — are summarized in Fig. 4.6 in order to demonstrate how the occurring ELM type and the edge kinetic parameters depend on the external settings of MP-coil configuration, gas puff and heating power. The type-I ELM frequencies (a), the pedestal top densities (b) and temperatures (c) and the upper values of the mean pressure gradients (d) are plotted against the gas puff. The data shows the mean values of different time slots with type-I ELMs only (filled squares), both types of ELMs (empty squares) and small ELMs only (crosses) of seven discharges whose characteristics are listed in Tab. 4.1. For two data points (red and grey), the uncertainties obtained from MCMC methods (cf. Fig. 4.4 and section 3.3) are shown.

Discharge	MP-coil setting	P_{NBI} [MW]	Color
#27941	$n = 1$ resonant	9.7	orange
#27942	—	9.4	grey
#27943	$n = 1$ non-resonant	8.7	light blue
#28847	$n = 2$ resonant	4.9	red
#28848	—	4.9	black
#28850	$n = 2$ non-resonant	4.9	blue
#28863	—	7.4	brown
#29231/32/33/38	$n = 2$ resonant	4.7-12.1	dark red (only in
#29231/32/33/38	—	4.7-12.1	dark grey Fig. 4.7)

Table 4.1: Characteristics of discharges shown in Fig. 4.6 and Fig. 4.7

Type-I ELM frequency versus gas puff (Fig. 4.6 (a)): In all the discharges the frequency of the type-I ELMs decreased with increasing gas puff until they were suppressed completely. The decay was faster with lower heating power (compare black and brown shaded lines) and — for the same heating power — the type-I

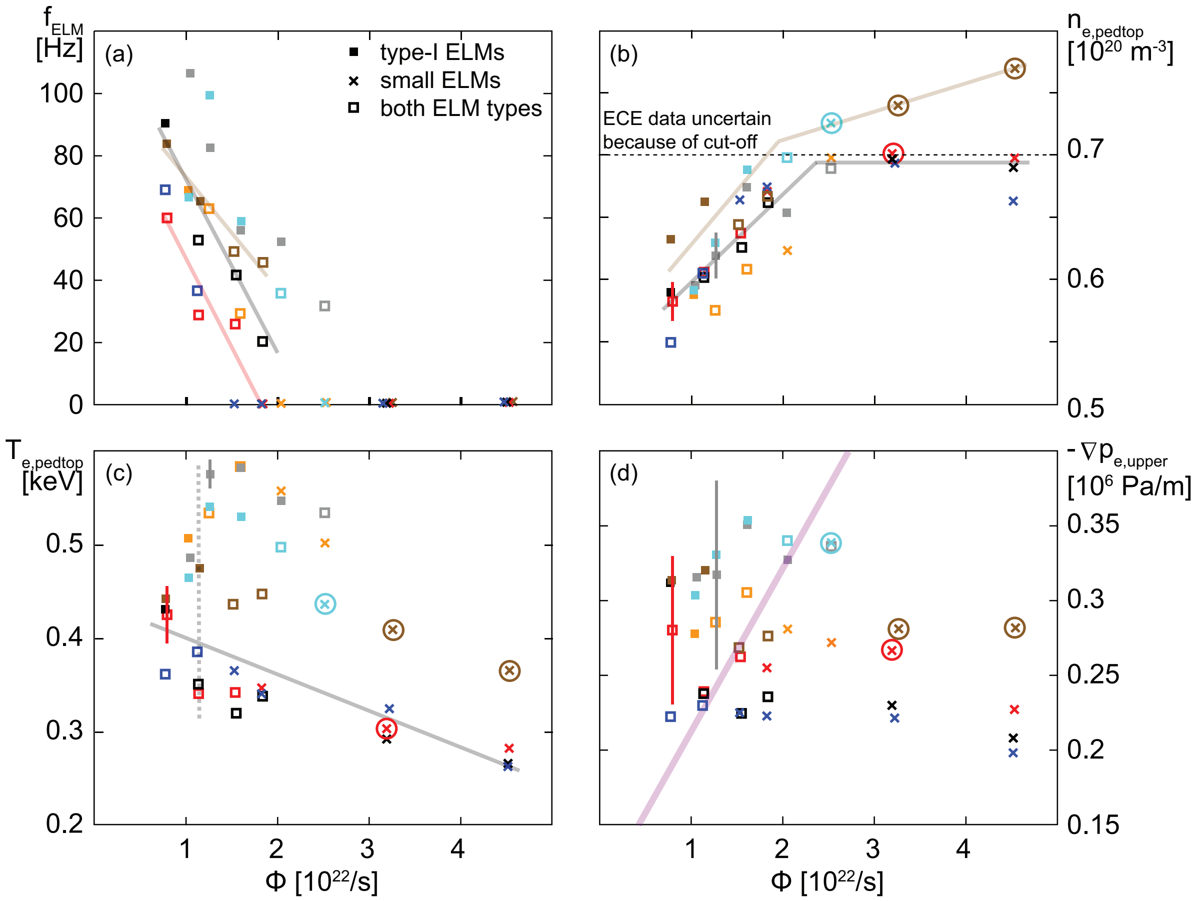

Figure 4.6: (a) Type-I ELM frequency, (b) pedestal top density, (c) pedestal top temperature and (d) upper edge pressure gradient versus gas puff for various discharges shown in different colours; the different symbols indicate the ELM type; the circles mark data that are less reliable due to the ECE cut-off; additionally plotted are lines to guide the eye.

ELM frequency was generally lower with than without MPs (compare black and red shaded lines). Whether resonant or non-resonant MPs suppressed type-I ELMs earlier depended on poloidal mode number n of the perturbation field.

Pedestal top density versus gas puff (Fig. 4.6 (b)): The density first rose strongly with the gas puff and saturated (for low heating power, black shaded line) or increased more slowly (for high heating power, brown shaded line) at high gas puff. Data points above the vertical black dashed line were affected by the ECE cut-off and their temperature and pressure values were less reliable. These data — marked by circles in Fig. 4.6 and Fig. 4.7 — therefore had to be taken with care concerning their temperature and pressure values, while the accuracy of the density was not effected.

Pedestal top temperature versus gas puff (Fig. 4.6 (c)): Due to its cooling effect, stronger gas puff — at otherwise same conditions — resulted in lower pedestal top temperatures (cf. black shaded line). Higher heating power at the same gas puff caused higher temperatures (cf. black shaded dashed line). (Note that the data

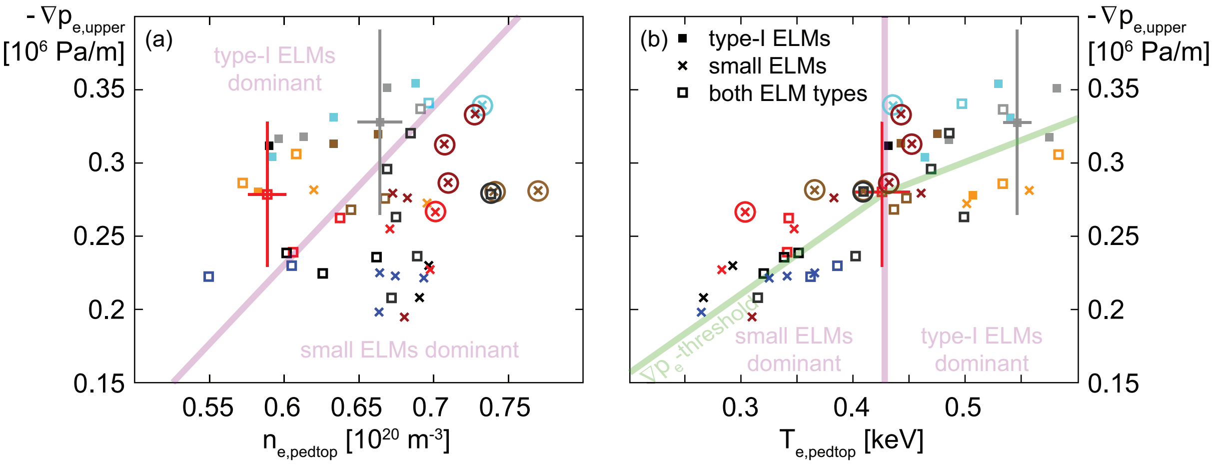

Figure 4.7: Upper edge pressure gradient versus (a) the density and (b) the temperature at the pedestal top for various discharges shown in different colours; the different symbols indicate the ELM type; the circles mark data that are less reliable due to the ECE cut-off; additionally plotted are lines to guide the eye.

points of #27941/2/3 at a gas puff of $\Phi = 1 \times 10^{22}\mathrm{s}^{-1}$ did not yet have the full power.) Discharges with identical plasma settings exhibited similar pedestal top temperatures with and without MPs, except for the significantly reduced values of #27943 (light blue) and of the point with lowest gas puff of #28850 (blue).

Upper pressure gradient versus gas puff (Fig. 4.6 (d)): In discharges #27941, #27942, #27943 and #28850, the evolution of density and temperature compensated each other such that the pressure gradient was almost constant with increasing gas puff. In discharges #28847, #28848 and #28863 the pressure gradient was reduced with stronger gas puff. The only significant difference between discharges with and without MPs was the reduced value of #28850 (blue) with lowest gas puff. It can clearly be seen that in regimes with low gas puff and high pressure gradient (above purple line), type-I ELMs were the dominant ones.

Operationally, application of MPs or a large gas puff can result in mitigation of ELMs. However, the identification of the actual (physical) reason for ELM mitigation requires the detection of dependencies between internal parameters and the ELM type. To study whether large and small ELMs populate separate edge parameter regions, independently of which actuator is used to access them, the upper values of the pressure gradients of the discharges listed in Tab. 4.1 are plotted versus the pedestal top densities (a) and temperatures (b) in Fig. 4.7 with the different ELM types marked by different symbols.

Upper pressure gradient versus pedestal top density (Fig. 4.7 (a)): This plot can be divided in two regions according to the occurrence of ELM type as indicated by the purple shaded line. Type-I ELMs (filled squares) clearly dominated at higher pressure gradients and lower pedestal top densities, while at lower pressure gradients and higher densities, mostly small ELMs (crosses) occurred. This behaviour was independent of the external settings, however application of MPs provoked small ELMs also at rather low densities (red and orange) and non-MP cases also showed type-I ELMs at rather high densities and low pressure gradients (black and dark grey). The indicated uncertainties demonstrated that small variations — especially in the pressure gradient — could not be resolved, while the differences between the two regions were significant. For the data at very high densities marked by the circles, the estimation of temperature and pressure was less reliable due to the ECE cut-off.

Upper pressure gradient versus pedestal top temperature (Fig. 4.7 (b)): There seemed to exist an upper threshold for the pressure gradient (green shaded line) in both ELM regimes which increased monotonically with the pedestal top temperature. The small ELMs mainly occurred at a colder pedestal top (left of the purple shaded line), the region of higher pedestal top temperatures and pressure gradients was dominated by type-I ELMs. Application of different MP-coil configurations might have resulted in different threshold temperatures between the type-I and small ELM regimes — towards lower pedestal top temperatures without MPs.

4.5 The onset of ELM mitigation

Another series of discharges — #28231 (red), #29232 (blue), #29233 (green) and #29238 (black) — with similar settings compared to the ones presented in section 4.1 had been performed to investigate under various conditions how 'easy' it was to achieve ELM mitigation, i.e. how strong the perturbation fields had to be. In contrast to previous discharges, the MP-coil current was ramped up slowly — twice in each discharge — at otherwise constant conditions. All MP phases differed in heating power and/or gas puff to measure the MP-coil current needed for ELM mitigation under various conditions. The ELM mitigation onset data are shown in Fig. 4.8. The gas puff Φ (a), the heating power P_{NI} (b), Φ^2/P_{NI} (c), the pedestal top density (d) and temperature (e) and the edge pressure gradient (f) are plotted against the MP-coil current.

MP-coil current threshold versus global discharge parameters (Fig. 4.8 left) There was a tendency that with increasing gas puff, the perturbation field needed for ELM mitigation was less (a) but no clear correlation of the MP-coil current threshold with the heating power (b). However, at similar gas puff (red and blue), the MP-coil current threshold rose with the heating power. Combining these dependencies delivered an almost monotonic increase of the MP-coil current threshold with decreasing Φ^2/P_{NI} (c).

MP-coil current threshold versus local edge parameters (Fig. 4.8 right) Apart from the case with lowest heating power (red point at $I_{\mathrm{MP}} = 0.35\,\mathrm{kA}$), ELM mi-

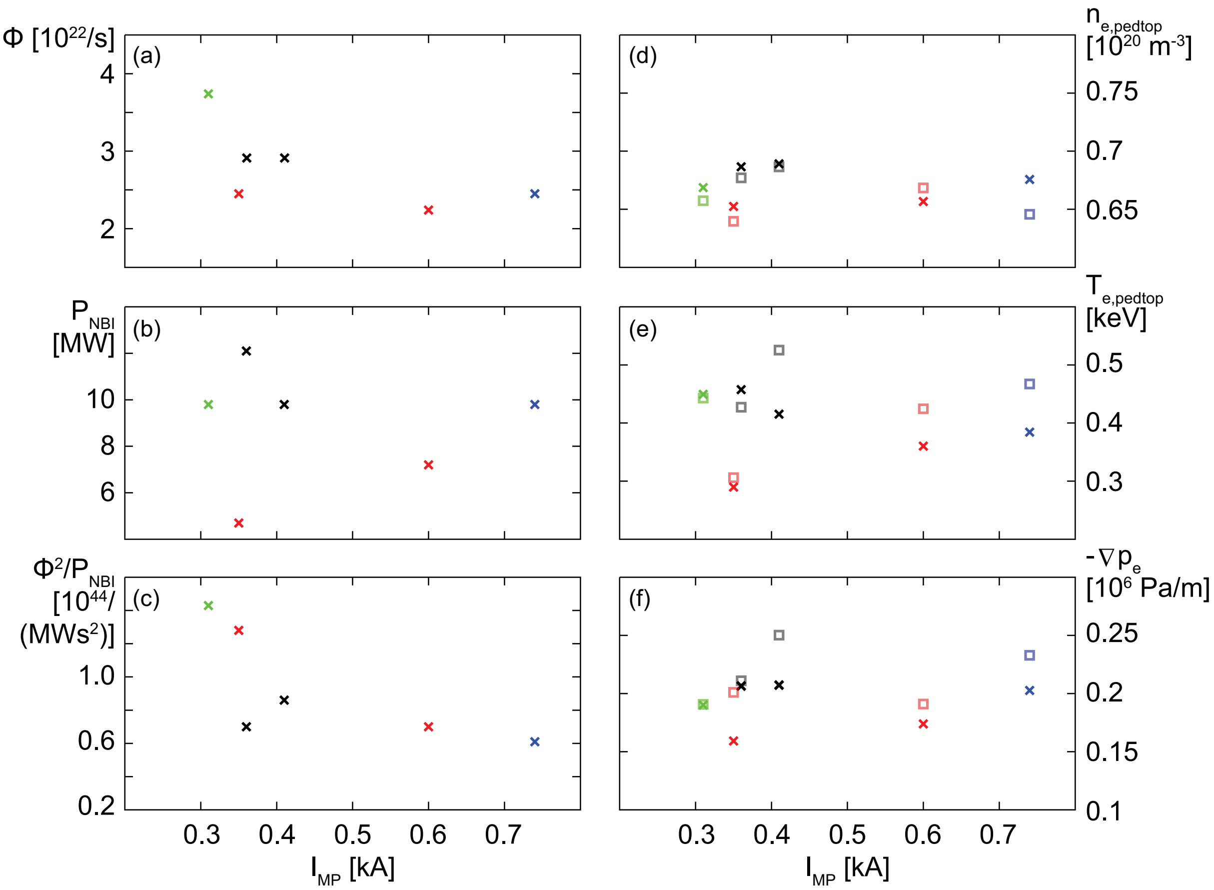

Figure 4.8: (a) Gas puff Φ, (b) heating power P_{NI}, (c) $Φ^2/P_{NI}$, (d) pedestal top density, (e) pedestal top temperature and (f) upper edge pressure gradient versus MP-coil current at the onset of ELM mitigation for discharge #29231 (red), #29232 (blue), #29233 (green) and #29238 (black); the shaded squares on the right-hand side indicate the corresponding kinetic data just before the MP onset.

tigation always started at very similar edge kinetic data (crosses). The pedestal top density (d) was rather high, the pressure gradient (f) rather low. Furthermore, the comparison of each data point at the ELM mitigation onset (crosses) with the associated value just before the MP onset (shaded squares, correct position would be at $I_{\mathrm{MP}} = 0\,\mathrm{A}$) indicated that switching on the MPs did not have a significant effect on the edge kinetic data.

The variation in the global parameters at the onset of ELM mitigation while the local edge kinetic data were always similar, demonstrated that the physics condition was the same but the recipe to reach it differed.

The slow ramp of the MP-coil current also allowed to investigate a possible dependency of the level of diffusive transport on the strength of the error field. For the

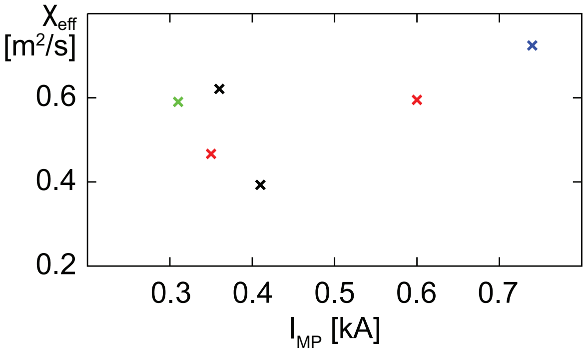

Figure 4.9: Heat diffusivity versus MP-coil current at the onset of ELM mitigation.

cases above with varying MP-coil current, Fig. 4.9 shows that there was no clear correlation between the effective heat diffusivity χ (cf. (2.3)) and the MP-coil current threshold.

4.6 Discussion

Experiments have been performed to study the transition from type-I to small ELMs — by increasing the gas fuelling rate or application of MPs — and the associated edge kinetic data. Generally, small ELMs tend to occur at higher pedestal top densities and reduced pedestal top temperatures and edge pressure gradients compared to regimes with dominant type-I ELMs.

In view of the detailed edge parameter measurements and some results from the literature, possible mechanisms for ELM mitigation via MPs (cf. section 2.2) are now discussed.

Evaluation of "hypothesis ELM-I" The reason for type-I ELM suppression might be an increased radial transport due to an ergodized magnetic field which degrades the pedestal pressure below the ballooning limit. In this case the level of radial transport should depend on the degree of stochasticity. Therefore, with increasing heating power the onset of ELM mitigation — which is supposed to occur at the same edge parameters just below the ballooning limit — should start at a higher transport level according to (2.3). This means that ELM mitigation at higher heating power should require stronger ergodization which is controlled by the MP-coil current. The experiments described above allowed the evaluation of the radial energy transport for different densities, heating powers and MP-coil currents. Since the effective heat diffusivity shows no correlation with the MP-coil current at the onset of ELM mitigation (cf. Fig. 4.9) it is indicated that the degree of ergodization is not sufficient to open up an additional channel of radial transport which degrades the pressure below the ballooning limit.

The conclusion that the level of ergodization is lower than suggested by the vacuum calculations of the ‘Chirikov’ parameter (cf. section 2.2) is a sign for the efficient shielding of the perturbation fields inside the separatrix.

Furthermore, the results presented in this work and also most of the other observations at ASDEX Upgrade show that the plasma reacts very similar to resonant and non-resonant MPs, while ergodization is only possible with the application of a resonant perturbation. Moreover, ergodization does not explain the occurrence of small ELMs.

However, ELM suppression experiments at DIII-D in the low collisionality regime [16] might be caused by enhanced radial transport due to a weakly stochastic layer.

Evaluation of "hypothesis ELM-II" Since the transition from type-I to small ELMs can not only be induced by the application of MPs, but also by strong deuterium fuelling and since the small ELM regime in the presence of MPs is accessed easier at higher gas puff, there might be a common mechanism for ELM mitigation based on edge cooling via particle influx. In fact, small ELMs generally occur — with and without MPs — in regimes with higher pedestal top densities, lower pedestal top temperatures and slightly reduced edge pressure gradients compared to type-I ELMy regimes (cf. Fig. 4.7).

However, the effect of MPs seems not to be the provision of an additional source of cold particles from the SOL region. This is indicated by the fact that in type-I ELMy regimes, the density is similar or even lower with MPs (compare red and blue with black as well as orange and light blue with light grey in Fig. 4.6 (b) at a gas puff $\Phi \lesssim 1.5 \times 10^{22}\,\mathrm{s}^{-1}$). Furthermore, Fig. 4.8 (d) shows that the densities just before the onset of MPs and just after the onset of ELM mitigation are very similar. Hence, reaching a certain density value might not be sufficient — but necessary — for ELM mitigation. This is also reflected in Fig. 4.7 (a) which shows fully mitigated ELMs only for $n_{\mathrm{e,pedtop}} \gtrsim 6.6 \times 10^{19}\mathrm{m}^{-3}$, while also type-I ELMs occur in this density regime. The possible observation of higher densities with than without MPs (compare blue with black and light blue with light grey in Fig. 4.6 (b) at a gas puff $\Phi \approx 1.5 - 2.5 \times 10^{22}\,\mathrm{s}^{-1}$) might be related to the reduced particle losses during small ELMs compared to type-I ELMs.

The requirement of a high edge density for ELM mitigation seems to lay in its relation to a low temperature which is the more probable candidate to determine the ELM type (cf. Fig. 4.7 (b)). Nevertheless, also the temperature is not generally lower with MPs (cf. Fig. 4.6 (c)) and does not decrease immediately with the onset of MPs (cf. Fig. 4.8 (e)). The fact that the temperature for the data points at higher MP-coil current tended to be smaller compared to the associated points without MPs might be explained by the longer transition times during which the temperature can be decreased due to the arising small ELMs in between the type-I ELMs.

Evaluation of "hypothesis ELM-III" The observation that the suppression of type-I ELMs comes along with the emergence of small ELMs may lead to the assertion that the edge pressure gradient is clamped by the occurrence of small ELMs at a value below the type-I ELM threshold. In fact (see discussion above) the edge pressure gradient seems to not depend on the heat flux, indicating its nature as a stability limit, rather than resulting from a diffusive transport mechanism. I.e. under certain conditions — preferably in the presence of MPs — the stability threshold for the small ELM must be lower than that of type-I ELMs.

In Fig. 4.10 the same data as in Fig. 4.7 is shown but for easier comparison the colour-coding here distinguishes only cases with (red) and without MPs (black). Furthermore, data points which are less reliable because of their closeness to the cut-off densities are removed. The shaded lines indicate possible stability thresholds for type-I ELMs (purple) and small ELMs (light blue and green). These lines are not obtained by fitting the data, but created such that their trends and relative locations are consistent with the data and might explain the following conclusions.

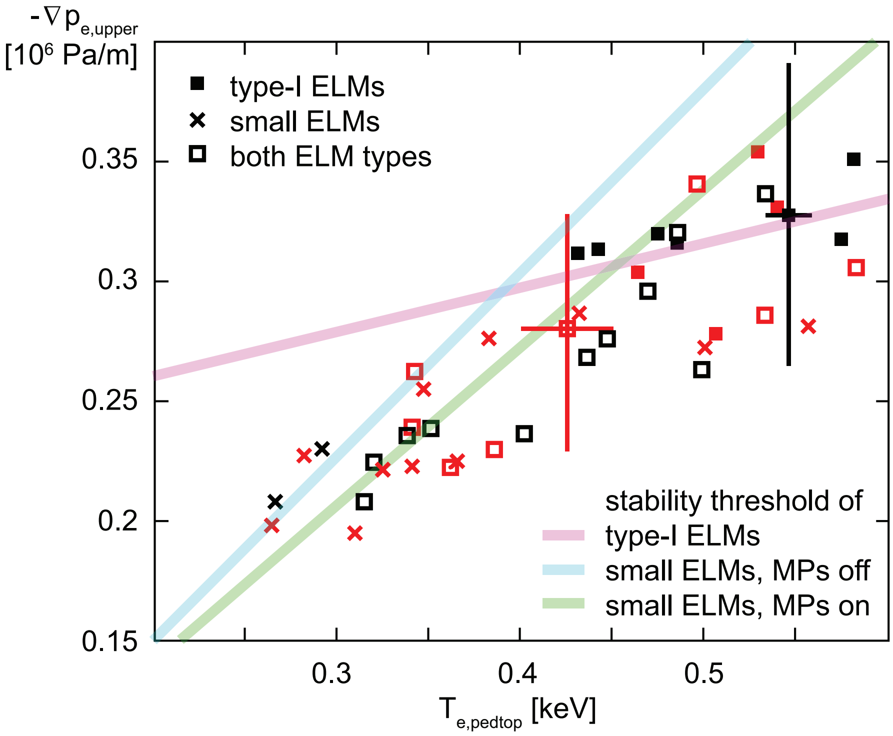

Figure 4.10: Upper edge pressure gradient versus pedestal top temperature for various discharges with (red) and without (black) MPs; the different symbols indicate the ELM type; additionally plotted are lines to guide the eye.

According to this image, in regions of colder edge plasma the stability threshold for small ELMs is lower than the type-I ELM threshold, i.e. small ELMs are triggered before the limit for type-I ELM is reached and the latter is suppressed — vice versa at high edge temperatures. The closer both stability thresholds are, the higher is the probability for coexisting type-I and small ELMs. The dependency of the occurring ELM type on the temperature might be a sign for the small ELMs being a resistive instability since the resistivity increases with decreasing temperature ($\eta \propto T^{-1.5}$) [92].

A possible effect of the MPs might be a shift of the small ELM stability limit towards higher edge temperatures (green versus blue line). This is indicated by the occurrence of regimes with small ELMs only in the range of $T_{\mathrm{e,pedtop}} = 300 - 400\,\mathrm{eV}$, while with MPs complete type-I ELM suppression is only observed below $T_{\mathrm{e,pedtop}} = 250 - 300\,\mathrm{eV}$.

Summarizing all these findings, the following picture about the formation of the edge parameters and the occurrence of ELM type emerges:

Heating power and gas puff determine density and temperature. These are thereby coupled via the pressure gradient that is clamped by the ELM stability limit. The ELM type and the threshold pressure gradient in turn depend on the pedestal temperature. In the low temperature (resistive) regime the pressure gradient decreases strongly with the edge temperature, while in the high temperature (ideal) type-I ELM regime, the pressure gradient does not or only slightly depend on the temperature. A possible dependence of the type-I ELM stability threshold on the temperature might be due to arising resistive effects in the low temperature range. Furthermore, the temperature might act on the stability via the bootstrap current, which has a stabilizing effect on the ballooning modes and increases with temperature.

Starting from a point at the top right of Fig. 4.10 and either reducing the heating power or increasing the gas puff, the operational point moves to the left, i.e. the temperature decreases while the pressure gradient is not or only slightly affected and the density increases. With further temperature reduction, the operational points enters the region where the stability limits of type-I and small ELMs are close to each other and both types of ELMs occur. Due to the emergence of the small ELMs, whose stability limit is much stronger coupled to the temperature, the edge pressure gradient decreases with reduced temperature. At some point also the density can no longer increase and eventually even decreases. In this picture, the effect of MPs consist in shifting the transition between both ELM types towards higher temperatures.

Up to now, only the differences between the small ELMs and type-I ELMs have been discussed. However, it would also be interesting to know whether the small ELMs might be identified with or clearly distinguished from another ELM type, especially type-II and type-III ELMs. The present work allows the comparison of small ELMs caused by MPs (in this paragraph: MP-mitigated ELMs) with the ones caused by a strong gas puff (without MPs) — which are supposed to be type-III ELMs [55]. In fact, there are many similarities between the MP-mitigated ELMs and the type-III ELMs. Both of them only exist at a sufficiently high gas puff relative to the heating power. Furthermore, they are both related to regimes with higher edge density and reduced edge temperature and pressure gradient. Although the 'threshold' values of these external and local edge parameters are not the same for the occurrence of MP-mitigated ELMs and type-III ELMs, the transition from type-I to both small ELM regimes follows the same trend in the mentioned parameters. This might be an indication that MP-mitigated ELMs and type-III ELMs are caused by the same instability with a slightly different stability threshold in the presence of MPs.

Nevertheless, type-III ELMs exhibit two typical features that have not been observed for the MP-mitigated ELMs [93]: A magnetic precursor and the decreasing poloidal velocity of the modes related to the occurrence of each ELM event. However, in [93] also significant differences between MP-mitigated ELMs and type-II ELMs have been found. The first do neither show the continuous fluctuations nor the poloidal asymmetry in the mode amplitude of the latter.

5 Edge kinetic data during L-H transitions with magnetic perturbations

(Parts of this work will be published in: Ryter F *el al* Survey of the H-mode power threshold and transition physics studies in ASDEX Upgrade *to be published in Nucl. Fusion*)

Although the purpose of the application of Magnetic Perturbations (MPs) is ELM mitigation, MPs do also affect the threshold power needed for the L-H transition. This is important for ITER which will be operated only slightly above this threshold (cf. section 2.1). Hence, the object of the study presented in this chapter was the effect of MPs on the edge electron temperature, density and pressure and related quantities before and at the L-H transition. The chapter is structured similarly to the previous one. First, the discharge setup and general plasma behaviour around the L-H transition are displayed in section 5.1. This is followed by a detailed description of the differences in the edge kinetic profiles with and without MPs at some dedicated time points in section 5.2, while section 5.3 provides the complete temporal evolution of the edge gradients and pedestal top values across the L-H transition. This information enables an approximation of the heat transport which is presented in section 5.4. These first four sections are restricted to the results of one exemplary pair of identical discharges with and without MPs. In the following section 5.5, which is focussed on the radial electric field at the L-H transition, the findings of several similar discharges are included. The chapter ends with a discussion.

5.1 Discharge description

Representative for all experiments used for this study, discharges #28395 and #28394 are discussed in detail. Apart from the application of MPs in #28395, the discharges were identical. Some of their time traces are shown in Fig. 5.1, where the red lines correspond to #28395 and the blue lines to #28394. This colour classification of data with MPs indicated in red and data without MPs displayed in blue is maintained throughout this whole chapter. The heating power (cf. appendix A) was provided by ECRH (black in (a)) only, which — in contrast to NBI — offered the possibility of neither inducing a torque nor additional particles. NBI (grey in (a)) was only applied with short pulses which did not contribute to the heating, but were necessary for CXRS measurements (cf. appendix A). The ECRH power was increased in small steps to achieve a slowly developing plasma and a smooth evolution of the net thermal loss power P_{LOSS} (red/blue in (a)) which is defined by (2.1). Panels (b), (c) and (d) of Fig. 5.1 respectively show the plasma stored energy W_{MHD}, the line-averaged edge density $n_{\mathrm{e,H5}}$ provided by the 'H5' channel (cf. Fig. 3.3) of DCN interferometry (cf. appendix A) and the D_α radiation.

In the presence of MPs, the L-H transition (marked by the vertical red line) occurred

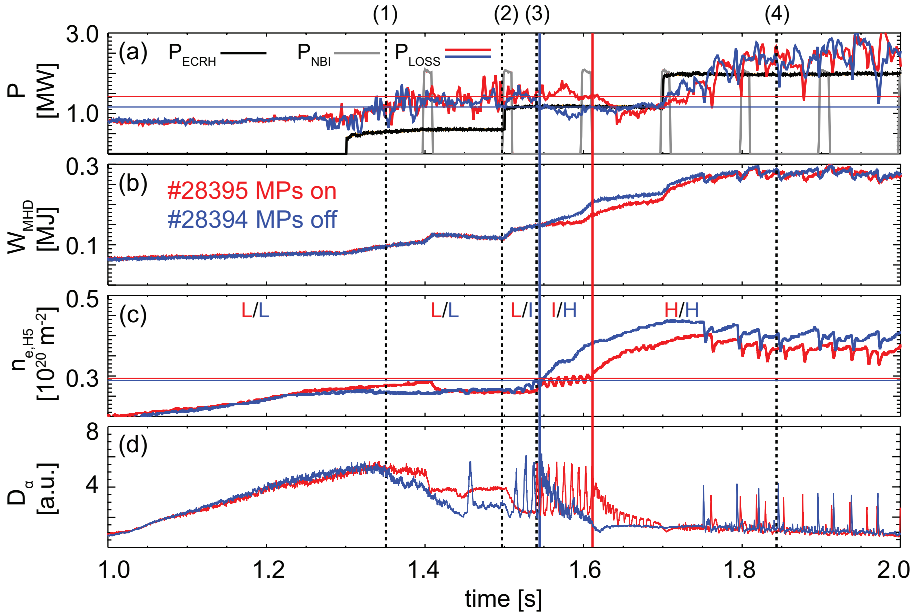

Figure 5.1: Time traces of (a) the ECRH (black), NBI (grey) and loss (red/blue) power, (b) the plasma stored energy, (c) the line-averaged edge density and (d) the D_α radiation for discharge #28395 with MPs (red) and its reference discharge #28394 without MPs (blue), the L-H transitions are marked by the vertical solid lines; the dashed numbered lines indicate the time points of the profile shown in Fig. 5.2.

60 ms later than in the reference case (blue) — at almost the same density, but larger loss power (as indicated by the horizontal lines). The oscillations of density and D_α light preceding the L-H transition in both discharges probably indicate an Intermediate phase (I-phase) [44] caused by transitions back and forth between phases of low and high transport. In the fully developed H-mode, the plasma energy was very similar in both discharges, while the density was slightly reduced with MPs. From 1.75 s on, both discharges exhibited type-I ELMs as can be seen by the drops in density and energy and the spikes in the D_α radiation. Hence, no ELM mitigation with MPs has been achieved in this case since the density was below the threshold. The vertical black dashed lines indicate the time points of the profiles shown in the following.

5.2 Kinetic edge profiles

In Fig. 5.2, the electron edge kinetic profiles of discharge #28395 (red solid lines) and #28394 (blue dashed lines) are compared at four different characteristic time points.

From top to bottom each row depicts the electron temperature profiles (lines) of both discharges together with the modelled (red pluses) and the measured (black crosses) radiation temperature values at the positions of their cold resonance of #28395 (a,e,i,m). Panels (c,g,k,o) depict the electron density. For discharge #28395, the density profile has been shifted 5 mm inwards within ECFM analysis (red solid line). The original density profiles are additionally shown as red dotted lines. The shift has been suggested by the separatrix criterion for the H-mode (cf. section 3.4) applied in the H-mode phase of

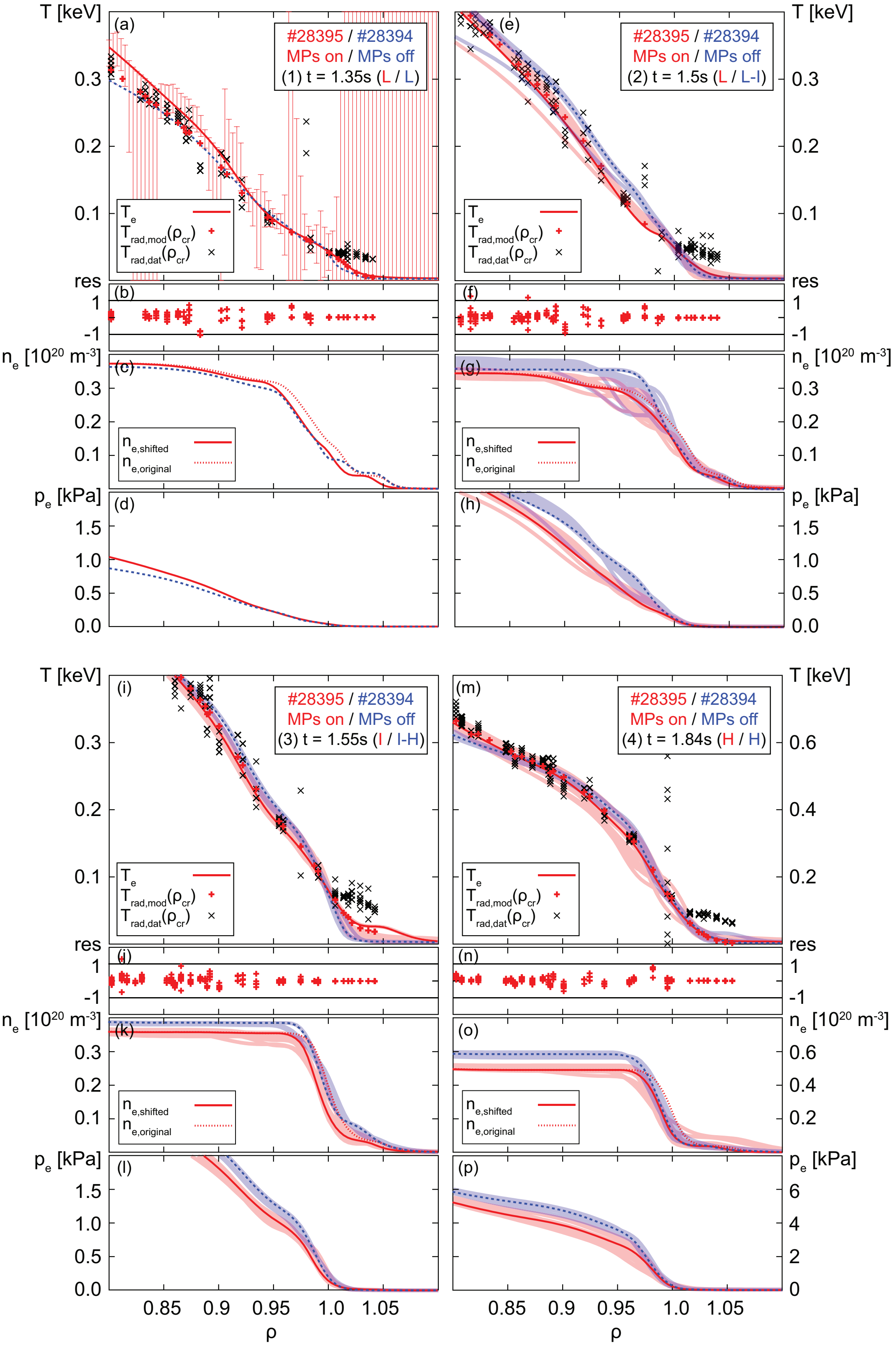

Figure 5.2: (a,e,i,m) Edge T_e, (c,g,k,o) n_e and (d,h,l,p) p_e profiles of discharge #28395 (red solid lines) and #28394 (blue dashed lines) at $t = 1.35\,\mathrm{s}$ (top left), $t = 1.50\,\mathrm{s}$ (top right), $t = 1.55\,\mathrm{s}$ (bottom left) and $t = 1.84\,\mathrm{s}$ (bottom right, different axis); the shaded lines mark the profile variations within 10 ms; for discharge #28395 also (a,e,i,m) the modelled (red pluses) and measured (black crosses) T_rad values at the positions of their cold resonance, (b,f,j,n) their residuals and (c,g,k,o) the original (non-shifted) density profiles (red dotted lines) are shown.

#28395 and was consistent with the misalignment between the LIB and the equilibrium reconstruction caused by the separatrix deformation due to MPs (cf. section 4.2 and [91]). The pressure profiles are plotted in (d,h,l,p).

In all cases the ECE data outside $\rho = 1.0$ has been omitted — as reflected by the large error bars in (a) — to avoid contributions from the 1st harmonic O-mode (cf. section 3.7). The uncertainties depicted in (a) were achieved via χ^2-binning method which demonstrates the informational content of the data and includes systematic uncertainties (cf. section 3.3). The actual uncertainty at some positions, e.g. outside $\rho = 1$ and in regions with large gaps between the ECE data, was much smaller. Furthermore, the systematic uncertainties were assumed to be very similar for both discharges. Hence, to investigate the significance of differences between both discharges, only the statistical scatter — plotted as shaded lines — of the edge kinetic data within a time period of 10 ms ($\widehat{=}$ 10 data points) was considered. The residuals (b,f,i,n) of #28395 indicated that the modelling worked well.

Time point (1) (top left) At this early time point during the first step of ECRH power, both discharges were in L-mode. The kinetic profiles were all the same with and without MPs.

Time point (2) (top right) This time point occurred slightly before discharge #28394 transitioned to I-phase, while discharge #28395 was still in clear L-mode. All kinetic values inside $\rho = 0.98$ were reduced in the presence of MPs. Hence, also the gradients, especially the pressure gradient, were significantly lower with MPs.

Time point (3) (bottom left) These profiles correspond to the phase just before the L-H transition for #28394 and the L-I transition for #28395. Due to the higher heating power, the electron temperature and pressure of both discharges were strongly increased. However, the pedestal top values of all quantities and the gradients of temperature and pressure were still slightly reduced with MPs.

Time point (4) (bottom right) In the fully developed H-mode, the pedestal top density and pressure and the pressure gradient were significantly reduced with MPs.

Fig. 5.3 shows the edge kinetic profiles of discharges #28394 (left-hand side and blue dashed on the right-hand side) and #28395 (right-hand side) at their respective L-H transition at $t = 1.55$ s and $t = 1.61$ s. The slight discrepancies in the absolute values inside the pedestal top were still remaining. Yet, the pressure gradient (h) at the transition seemed to be the same with (red solid line) and without (blue dashed line) MPs. Note here, that the density of #28395 (red solid line in (g)) seemed to be shifted too far inside at this time point. This small misalignment was not crucial for ECFM analysis. However, it strongly influenced the determination of the radial electric field, as will be demonstrated in section 5.5.

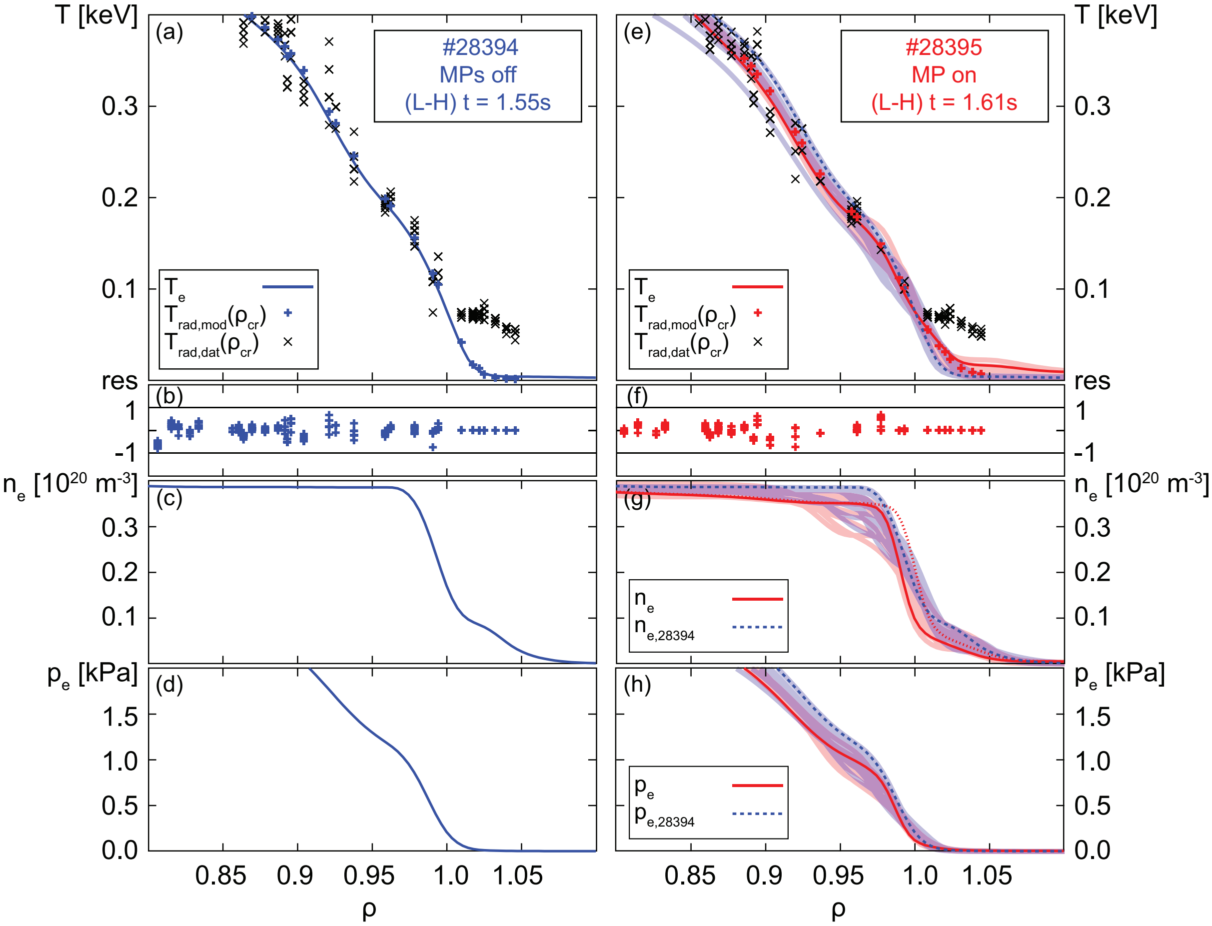

Figure 5.3: (a,e) Edge T_e profiles (lines) together with the modelled (pluses) and measured (black crosses) T_{rad} values at the positions of their cold resonance, (b,f) their residuals, (c,g) the n_e profiles and (d,h) the p_e profiles of discharge #28394 (left, blue) and #28395 (right, red) at their L-H transition times $t = 1.55/1.61$ s; the dashed blue lines on the right-hand side show again the profiles of #28394; the shaded lines on the right-hand side mark the profile variations within 10 ms; the red dotted line in (g) additionally shows the original (non-shifted) density profile of discharge #28395.

5.3 Temporal evolution of the edge kinetic data

Applying the two-line fit on the profiles as described in section 4.2 delivers the mean edge gradients and pedestal top values of electron temperature, density and pressure. Fig. 5.4 depicts those values for discharge #28395 (red squares) and #28394 (blue crosses).

Up to slightly before the L-H transition, the two-line fit did not work properly because the position of the break-point between the two fitted lines was undefined as the pedestal was not clearly formed. Hence, the scatter was very large and small differences between the two discharges could not be identified. However, the profiles shown on top of Fig. 5.2 in the previous section depict the typical L-mode characteristic of primarily identical profiles with and without MPs (time point (1)) and — with increasing heating power — of reduced edge kinetic values and gradients with MPs (time point (2)).

Despite the large scatter it can clearly be seen in Fig. 5.4 that the edge electron temperature and pressure gradients and pedestal top values slowly increased after the

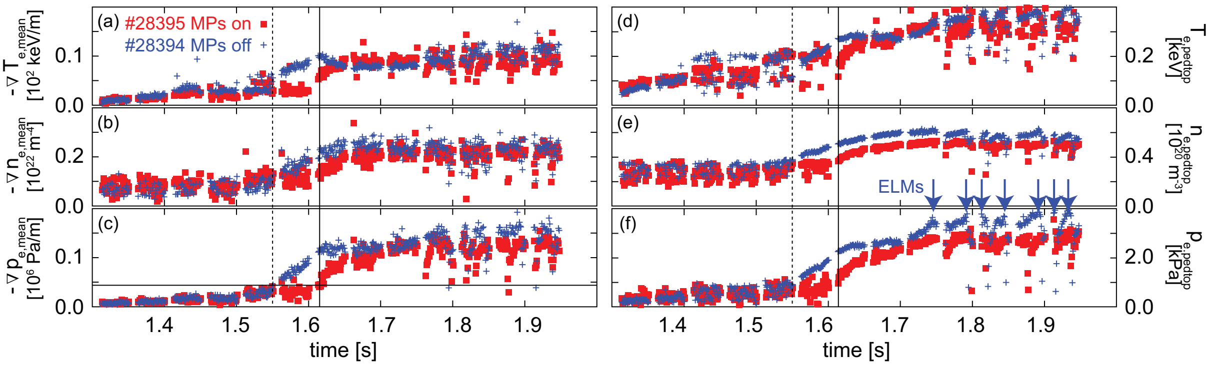

Figure 5.4: Time traces of the mean edge gradients (left) and the pedestal top values (right) of T_e (a,d), n_e (b,e) and p_e (c,f) of discharge #28395 (red squares) and its reference #28394 (blue crosses); the dashed (#28394) and solid (#28395) vertical lines mark the L-H transition times.

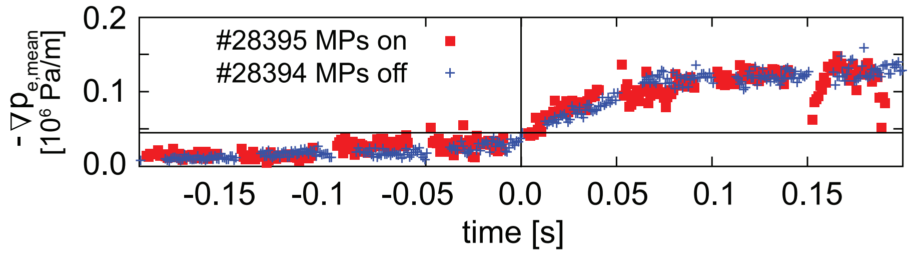

Figure 5.5: Temporal evolution of the mean edge pressure gradients relative to the L-H transition time of discharge #28395 (red squares) and its reference #28394 (blue crosses).

second step in the ECRH power at 1.5 s.

After the L-H transition at 1.55 s all kinetic edge gradients and pedestal top values of #28394 strongly increased due to the enhanced confinement, while the edge pressure gradient of #28395 remained slightly below the 'threshold' value up to the L-H transition at 1.61 s and then increased, as well.

The evolution after the L-H transition was similar in both discharges, but the pedestal top values of electron density and pressure and the edge pressure gradients were slightly lower with MPs. The large drops from 1.75 s on were related to ELM crashes.

The gaps in the time traces which frequently occurred every 50 ms arose from chopping of the LIB (cf. appendix C).

In Fig. 5.5, the temporal evolution of the mean edge pressure gradients is again plotted on a time axis relative to the L-H transition. It can nicely be seen that 100 ms before the L-H transition, the electron pressure gradient was higher for #28395 because it was later relative to the step in the heating power. It was already close to — but below — the 'threshold' value, while in #28394 the pressure gradient rose up to the 'threshold' value just before the transition, which then occurred at the same electron pressure gradient for both discharges.

5.4 Heat transport

In the previous sections it has been shown that the application of MPs degraded the edge kinetic profiles which delayed the L-H transition compared to the reference discharge without MPs. Here, it is studied whether the temperature reduction might have been caused by an increased heat transport.

The temporal evolution of the effective heat diffusivity before (dashed lines) and after (solid lines) the L-H transition of discharge #28395 (orange/red) and #28394 (light blue/blue) is plotted in Fig. 5.6 (a). In L-mode, in the range of 1.4 – 1.55 s (bold lines), the heat diffusivity was significantly higher with MPs. Fig. 5.6 (b) demonstrates that not only at the same heating power (at the same time), but also at the same net thermal loss power, the heat transport in L-mode (bold lines) was enhanced with MPs.

From L- to H-mode, the heat diffusivity decreased by a factor of 4 or 5 in both discharges. In H-mode the heat diffusivity seemed to be similar with and without MP.

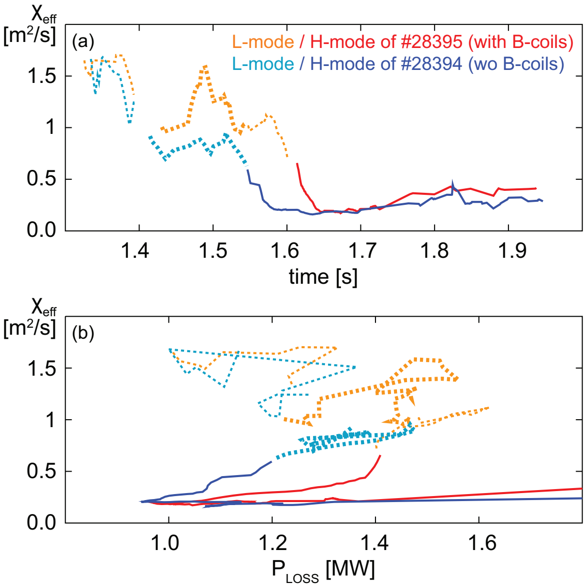

Figure 5.6: Effective heat diffusivity χ_{eff} versus (a) time and (b) the loss power of discharge #28395 (reddish) and #28394 (bluish) in L- (dashed lines) and H-mode (solid lines).

5.5 Radial electric field

In section 2.1 it has been discussed that the strength of the radial electric field shearing determines the accessibility to H-mode. The minimum of the radial electric field well serves — with the assumption of a constant radial electric field value at the pedestal top and a constant width of the well [94] — as a measure for the shearing and is a more robustly determined quantity than the shearing itself. In this section, (2.4) was applied to obtain the diamagnetic component of the radial electric field for several cases with and without MPs to investigate the well depth of the edge radial electric field close to the L-H transition.

Four examples of edge radial electric field profiles obtained from the electron edge kinetic data given by ECFM and IDA are shown in Fig. 5.7. All the results were achieved in L-mode, slightly before the L-H or L-I transition. The two cases on the left were without MPs (blue), the two cases on the right with MPs (red). The results at the top correspond to discharge #28807 that had two L-H transitions, one without and one with MPs. At the bottom, again results from discharges #28394 (without MPs) and #28395

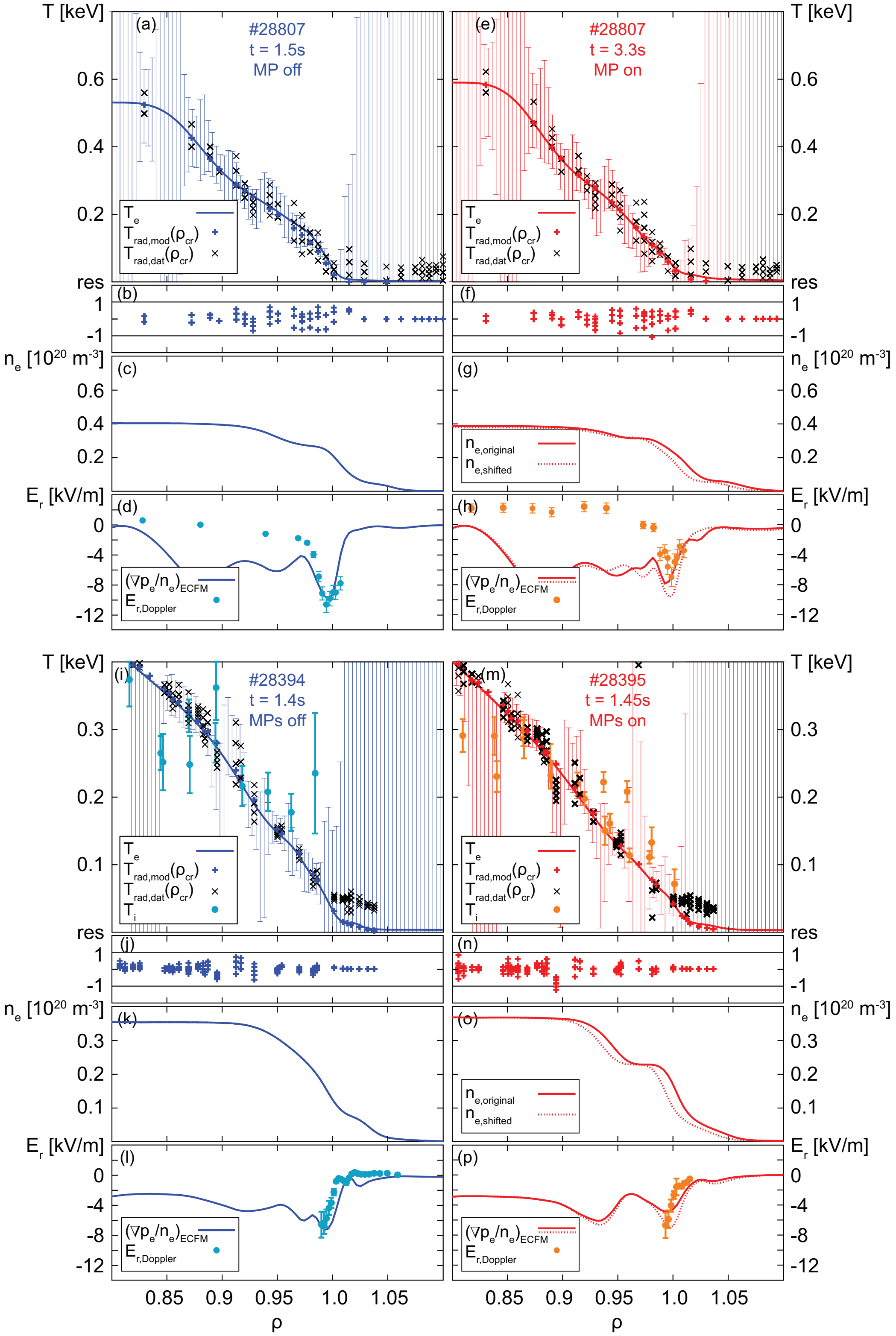

Figure 5.7: (a,e,i,m) Edge T_e profiles (blue/red lines) together with the modelled (blue/red pluses) and measured (black crosses) T_{rad} values at the positions of their cold resonance, (b,f,j,n) their residuals, (c,g,k,o) the n_e profiles and (d,h,l,p) the E_r profiles from ECFM/IDA (blue/red lines) and from Doppler reflectometry (light blue/orange dots) of discharge #28807 at $t = 1.5$ s without MPs (blue, top left) and at $t = 3.3$ s with MPs (red, top right) and of discharge #28394 without MPs (blue, bottom left) and discharge #28395 with MPs (red, bottom right) at $t = 1.4/1.45$ s; additionally plotted in (a,e) are the edge T_i profiles (light blue/orange dots).

(with MPs) are presented.

Plotted from top to bottom are the electron temperature profiles (blue/red lines) together with the modelled (blue/red pluses) and measured (black crosses) radiation temperature values at the positions of their cold resonance (a,e,i,m), the residuals of ECFM analysis (b,f,j,n), the density (c,g,k,o) and the radial electric field (d,h,l,p). For #28394 and #28395 also the ion temperatures (light blue/orange dots) obtained from CXRS measurements are plotted in (i) and (m). These were not available for discharge #28807, since there was no NBI. For all cases, the radial electric field profiles (d,h,l,p) obtained from ECFM/IDA analysis (lines) were compared with the ones from Doppler reflectometry measurements (dots) (cf. appendix A). With the MPs switched on (right-hand side) an inward shift of the density by 5 mm as suggested by the separatrix criterion (cf. section 3.4) applied in the following H-mode might have been required. The original (solid) as well as shifted (dotted) density (g,o) and the corresponding radial electric field profiles (h,p) are plotted.

Comparison of #28807 with MPs (top left) and without MPs (top right):

Temperature (a,e) The profiles were very similar with and without MPs.

Density (c,g) Apart from a slight outward shift — due to field line perturbation — with MPs, the profiles were very similar with and without MPs. ECFM analysis with a density profile shifted inwards by 5 mm (red dotted line) resulted in the same temperature profile.

Radial electric field (d,h) Around the separatrix, where the diamagnetic term of the radial electric field was the dominant one, the radial electric field profiles obtained from ECFM/IDA (without density shift) agreed very well with the ones obtained from Doppler reflectometry at both time points. The minimum in the case without MPs was with −10 keV slightly deeper than with MPs (−8 keV). Shifting the density profile 5 mm inwards for the MP case resulted in the same well depth as without MPs.

The two other minima in the diamagnetic radial electric field component were artifacts from the ECFM/IDA analysis. At $\rho = 0.88$ the electron temperature and, therefore, also the pressure gradient was probably overestimated due to the lack of data from further inside, which resulted in a flat extrapolation of the temperature inside $\rho = 0.85$ and a too steep gradient between $\rho = 0.8 - 0.95$. This uncertainty was also reflected in the large error bars in this range. The minimum at $\rho = 0.95$ was caused by the small step in the density profile, which might not be real. Nevertheless, there was a remaining discrepancy inside the pedestal top between the radial electric field from ECFM/IDA and Doppler reflectometry. This can partly be explained by the Doppler reflectometry measuring the total radial electric field including the Lorentz contribution caused by rotation (cf. (2.2)). Furthermore, the assumption of equal electron and ion temperature, which was justified at and outside the pedestal top [39] became less reliable towards higher temperatures and lower collisionalities ($\nu^\star \propto n_\mathrm{e}/T_\mathrm{e}^2$) further inside the plasma. Unfortunately, both of these effects could not be quantified due to lacking information about the ion temperature and rotation because there was no NBI for CXRS measurements. Yet, a comparison of the minimal values of $\nabla p_\mathrm{e}/n_\mathrm{e}$ close to the separatrix seemed to be reasonable.

Assessing the relation between electron and ion temperatures has been possible for discharges #28394/5, since they exhibited short NBI pulses for CXRS measurements. Comparison of #28394 with MPs (bottom left) and #28395 without MPs (bottom right):

Temperature (i,m) The electron and ion temperatures each agreed very well for $\rho \gtrsim 0.87$. Further inside, the ions were slightly colder than the electrons. The profiles — of both, the ion as well as the electron temperature — were very similar with and without MPs.

Density (k,o) Apart from the step inside the separatrix and a slight outward shift in #28395, the profiles were very similar with and without MPs. The step was probably an artifact from the analysis, the shift can again be explained by the field line perturbation due to the MPs. ECFM analysis with a density profile shifted inwards by 5 mm (red dotted line) resulted in the same temperature profile.

Radial electric field (l,p) Except for a slight shift, the profiles obtained from ECFM/IDA — with density shift for #28395 (red dotted line) — agreed very well with the ones from Doppler reflectometry. Due to the lower density, another frequency range — compared to discharge #28807 — had to be used for Doppler reflectometry measurements. These covered only the outer branch of the radial electric field well. However, the comparison with the result of the previous time point demonstrated that the innermost data point just corresponded to the radial electric field minimum. The latter was the same ($E_\mathrm{r,min} \approx -7\,\mathrm{kVm}^{-1}$) with and without MPs. Without the density shift (red solid line), the well depth was slightly reduced.

Fig. 5.8 shows the results obtained from several L-H transitions with (red circles) and without (blue squares) MPs. The minimal radial electric field occurring just before the L-I (empty symbols) and the I-H (full symbols) transition is plotted against the loss power. Associated pairs with and without MPs are connected with a black line.

All the L-H transitions appeared at minimal values of the radial electric field in the range of $E_\mathrm{r,min} = 6.5 - 11\,\mathrm{kVm}^{-1}$ which was comparable to its uncertainty range. Regarding the empty and filled symbols corresponding to one transition phase (marked by dashed ellipses), the well depth increased by about 10 % within the I-phase. This variation was not significant with respect to the large error bars obtained for single profiles.

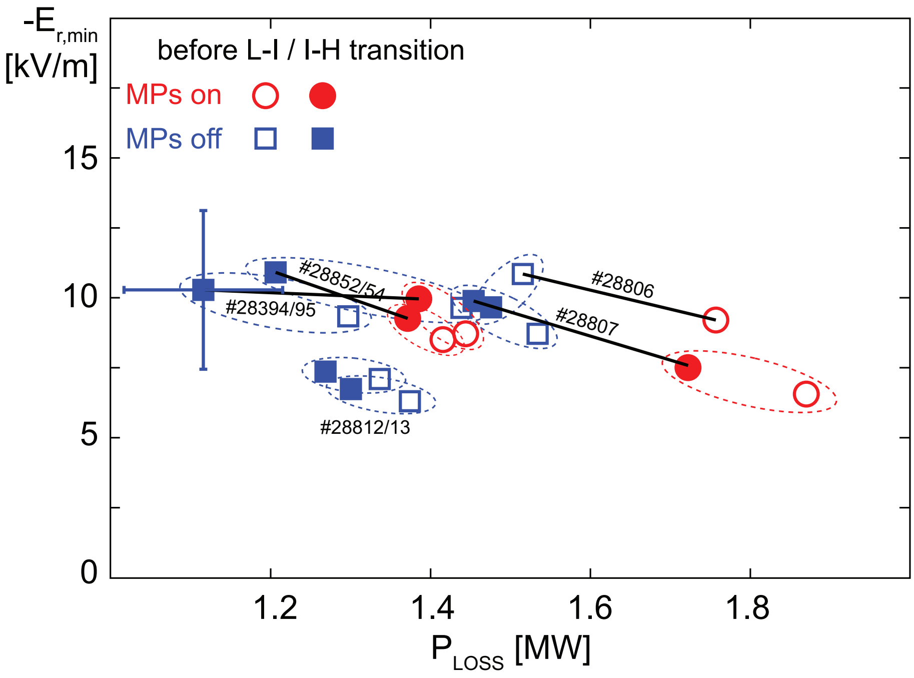

Figure 5.8: Minimal value of the edge radial electric field against the loss power at the L-I (empty symbols) and the I-H transition (filled symbols) with (red circles) and without (blue squares) MPs; pairs with and without MPs are connected with a black line.

However, since the systematic uncertainty was supposed to be the same within one discharge, the trend of increasing pressure gradient and radial electric field shearing from I- to H-mode might have been real — and reasonable. Also between L-H transitions with and without MPs there seemed to be a difference in the minimal value of the radial electric field of up to 20 %. However, as already mentioned, there is a large uncertainty arising from the alignment of electron temperature and density. The results shown in Fig. 5.8 were obtained from the original (un-shifted) density profiles. Yet, all the discharges with MPs had the same MP-coil setting causing an outward bending of the equilibrium field lines at the position of the LIB diagnostic. This could justify an inward shift of the density profile of about 5 mm as performed on the right-hand side of Fig. 5.7 which would eventually compensate the difference.

In any case, identical discharges except for their MP-coil setting, significantly differed regarding the power loss at the transition. As already indicated in section 5.1, a larger P_{LOSS} was needed for the L-H transition with MPs in all the analyzed pairs of discharges.

5.6 Discussion

It has been shown that the L-H transition occurs at a similar electron pressure gradient and radial electric field well depth with and without MPs, while the L-H power threshold is higher in the presence of MPs.

Using the example of one pair of identical discharges with and without MPs — the other similar experiments performed for this study show the same behaviour —, the effect of MPs on the edge kinetic parameters before and at the l-H transition is pointed out. In L-mode, at very low heating power, application of MPs has no influence on the edge kinetic data. With increasing heating power and steepened edge profiles, the pedestal top values and gradients are reduced with MPs compared to non-MPs cases at otherwise same conditions. The reason for the pedestal degradation seems to be an increased energy transport at the edge as indicated by the effective heat diffusivity which can — in L-mode — be significantly higher with MPs.

The rising level of transport in the presence of MPs might be caused by field line ergodization. It has been discussed in section 2.2 that ergodization can only occur with resonant MPs, while the applied fields in all the discharges presented here have been mainly non-resonant. However, it is conceivable that the small resonant component, which is always present (cf. section 2.2), causes a partly ergodized edge. This explanation would be consistent with the observation from DIII-D [19] that application of mainly resonant MPs increases the L-H threshold power stronger than non-resonant MPs. The observation of unchanged edge profiles at MAST [18] is not necessarily contradictory to the findings of this work, since at another machine with different discharge settings, the effect of MPs can easily vary.

A possible ergodization effect in the analyzed L-mode regimes would not be contradictory to the results presented in section 4.5 indicating no or negligible ergodization, because the screening of the error fields is probably more effective in the considered H-mode regimes with high density and collisionality than in the low density and low collisionality regimes of the analyzed L-mode discharges.

Despite the increased transport, the plasmas with MPs do — later in time and after stronger heating compared to the references — achieve the same pressure gradients as the cases without MPs and the L-H transition occurs at the same ‘threshold’ edge pressure gradient.

This is also reflected in the radial electric field well depth which is similar — relative to the uncertainties — just before the L-H transition in all analyzed discharges with and without MPs. This finding supports the model for the L-H transition described in section 2.1 which requires a sufficient radial electric field shearing to enter and sustain the H-mode. Whether this requirement is slightly reduced with MPs as indicated by the lower radial electric field minima in Fig. 5.8 or whether this is an artifact from the uncertain alignment of density and temperature profile could not be resolved. Furthermore, the ‘threshold’ values of the radial electric field depth are lower than the results from [39]. This might originate from the consideration of the ion instead of the electron kinetic data or systematic discrepancies due to the usage of different diagnostics and data fitting methods.

The few results of the total radial electric field obtained from Doppler reflectometry measurements indicate that the assumption of a dominant diamagnetic component at the edge is justified and that — in contradiction to MAST [18] — the increased L-H threshold power due to MPs is not a rotation effect. However, since the Doppler reflectometer setting has not been dedicated for that purpose, the effect of MPs on the total radial electric field should be tested in future experiments.

All the findings on the electron edge kinetic parameters, the heat transport and the diamagnetic component of the edge radial electric field presented in this chapter corroborate the hypothesis — formulated in section 2.1 — that application of MPs can degrade the electron pressure gradient, hence reduce the radial electric field shearing, by enhancing the heat transport via ergodization of the edge magnetic field and, therefore, increase the necessary heating power to reach the critical level of radial electric field shearing for achieving the H-mode.

6 Summary and Outlook

In future high power fusion reactors, type-I ELMs are likely to cause material damage. The application of non-axisymmetric MP fields in present day machines, has been proven to successfully mitigate ELMs. Nevertheless, the underlying mechanism is not yet understood which precludes a reliable prediction for the effect of MPs on ITER plasmas.

This work offers a method to improve the understanding of the plasma edge behaviour with respect to electron temperature and pressure, delivers new observations for the relation of MPs, ELM type and edge kinetic parameters which might contribute to the theoretical description of ELMs and ELM control and demonstrates how MPs can act on the L-mode edge kinetic parameters which might influence the accessibility to H-mode.

A new approach for the reconstruction of electron temperature profiles from ECE data has been developed which — in contrast to conventional ECE analysis — delivers accurate results also at the plasma edge by forward modelling of the electron cyclotron radiation transport taking into account the broadened emission and absorption profiles. These are calculated via a new analytical formula for the emission shape function considering frequency shifts due to relativistic and Doppler effects in a weakly relativistic thermal plasma. The method is able to quantitatively reproduce the measured electron cyclotron radiation intensities for all frequencies resonant up to the near SOL. This also includes the 'shine-through' peak which is caused by strongly down-shifted radiation originating from Maxwellian tail electrons in the H-mode edge gradient region and not being fully reabsorbed in the optically thin plasma region. A promising extension of this model seems to be the inclusion of refraction effects to avoid systematic errors of emission volumes positioned near the magnetic axis where refraction effects can be strong.

The method has been applied to a detailed study of the impact of MPs on the edge kinetic profiles and gradients in ELMy H-modes and at the L-H transition which revealed effects that could not be resolved with conventional ECE analysis.

According to the presented experiments, H-mode plasmas exhibiting small ELMs are related to regimes with higher pedestal top electron densities and reduced pedestal top temperatures and pressure gradients compared to type-I ELMy regimes. This edge parameter regime is achieved — independently of the application of MPs — by a strong gas puff and/or low heating power and restricted by the stability threshold for the edge pressure gradient which is a function of the pedestal temperature in the considered regime. MPs do not directly effect the edge kinetic parameters, yet ELM mitigation occurs in a different parameter range with applied MPs.

These observations allow to test a series of hypotheses about the origin of ELM mitigation. The pressure degradation seems not to be a consequence of an additional diffusive radial transport due to field line ergodization caused by MPs as it has been suggested by "hypothesis ELM-I". This has been indicated by the independence of the heat transport from the MP-coil current which should control the level of ergodization. Also "hypothesis ELM-II" of an increased plasma fuelling due to modified magnetic SOL topology in the presence of MPs that cools the edge and moves the operational point away from the ballooning boundary is not consistent with the presented results. These show unchanged edge kinetic parameters at increasing MP-coil current. The slight density rise after the onset of ELM mitigation (not the onset of MPs) is more probable a consequence of the reduced particle losses due to the smaller ELMs. Yet, from the low edge temperature values related to the small ELMs one can conclude that a rather cold pedestal top might be the necessary condition for the occurrence of small ELMs instead of type-I ELMs. This is consistent with the assumption that the stability threshold of small ELMs is lower than the one of type-I ELMs at low pedestal top temperatures, i.e. it is reached first and prevents the occurrence of type-I ELMs. The assumption of two overlapping stability thresholds would also explain the coexistence of both ELM types in the intermediate parameter regime. The second stability limit at lower edge temperatures might be related to a resistive MHD phenomenon. With MPs, complete type-I ELM suppression seems to be enabled at higher pedestal top temperatures than without. This confirms the "hypothesis ELM-III" that MPs are shifting the stability threshold of small ELMs. To validate this, stability analyses taking into account ideal and resistive MHD have to be performed which is beyond the scope of this work.

The L-H transition occurs at a similar edge pressure gradient and radial electric field shearing with and without MPs, but more heating power is needed to achieve these values in the presence of MPs which reduce the edge kinetic gradients and pedestal top values in L-mode. This might be caused by an increased energy transport as indicated by the higher effective heat diffusivity compared to identical cases without MPs. These findings support the "hypothesis LH" of edge confinement degradation via ergodization which increases the L-H power threshold. An important future experiment to consolidate whether or not the L-mode edge is ergodized by MPs is the investigation of the L-H transition with different MP-coil configurations (resonant, non-resonant, several poloidal mode numbers) and at varying MP-coil currents which should modify the degree of ergodization. It should also be checked whether this hypothesis is consistent with the observed density dependence of the effect of MPs by investigating the L-H transition at lower and higher densities.

The statement that ergodization might be the reason for the increased L-H power threshold, while it has been excluded to play a role in the presented H-modes is not contradictory, since both regimes differed strongly in density and collisionality which influences the effectiveness for screening the perturbation field. This should be validated in further experiments by changing the degree of ergodization in L-mode as described above and by searching for an H-mode regime where ergodization can occur also in the confined plasma region. Last but not least, calculations of the magnetic field structure taking into account also the possibility of field screening should be performed.

A The ASDEX Upgrade tokamak

The fusion experiment ASDEX ('Axial Symmetric Divertor EXperiment') Upgrade is a large research experiment of tokamak type in Germany. It is located at the Max-Planck-Institut für Plasmaphysik in Garching and started its operation in 1991 as successor of the ASDEX tokamak.

ASDEX Upgrade [95] exhibits a major radius of 1.65 m, a minor radius of 0.5 m and a plasma volume of 14 m^3. It can be operated with magnetic fields up to 3.1 T and plasma currents up to 1.6 MA. Most plasma discharges use a central magnetic field of 2.5 T and a plasma current of 1 MA. Three different sources of heating systems provide a combined power of 27 MW: The Neutral Beam Injection (NBI), which heats the plasma particles via collisions with highly energetic deuterium atoms and the Electron and Ion Cyclotron Resonance Heating (ECRH and ICRH) launching micro- and radio waves into the plasma that are absorbed by the electrons and ions. This heating mix allows for different heating of ions and electrons, flexible heat deposition and current drive. Plasmas with pulse duration of 10 s, densities of $\sim 10^{20}\,\mathrm{m}^{-3}$ and temperatures of ~ 10 keV can be generated.

Two of the most important features of ASDEX Upgrade are its reactor-relevant plasma shape and wall material which enable to address critical issues for ITER operation and DEMO design.

The elongated plasma geometry and closed divertor configuration (cf. right-hand side of Fig. 1.2) come close to the ITER design — down-scaled by a factor of four — and are produced by a set of vertical field coils outside the vessel (purple in Fig. A.1). This was aimed to study different divertor concepts, power and particle exhaust under various conditions, target heat loads, radiative cooling, control of plasma density and impurities and pumping efficiency. [97]

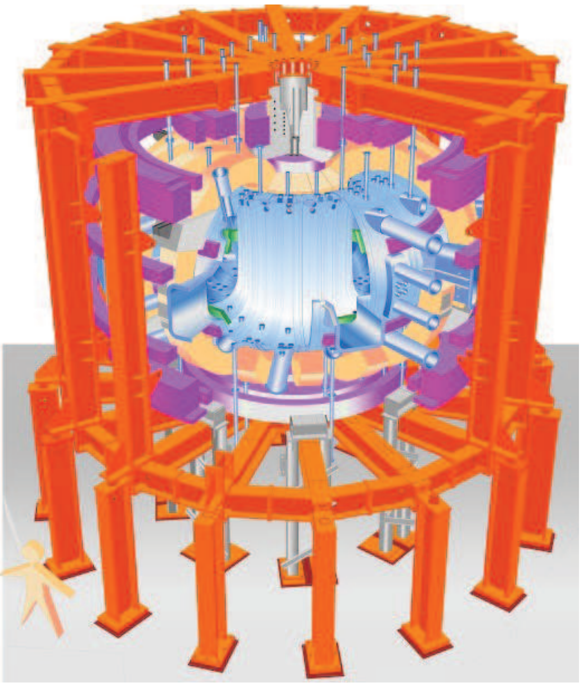

Figure A.1: Three-dimensional schematic of the ASDEX Upgrade tokamak [96].

Since 2007 all plasma facing components are coated with tungsten [98], as can be seen on the photograph of the torus inside in Fig. A.2. In future fusion devices, the usage of low-Z materials, especially carbon, as wall materials has to be avoided due to their high erosion and tritium retention. High-Z materials like tungsten are more favourable in terms of erosion and chemical reactions with hydrogen isotopes. However, they were feared to degrade the energy confinement due to their higher radiation power losses. Nevertheless, the fully tungsten coated machine demonstrated high-performance operation with central tungsten concentration below the critical limit [99].

ASDEX Upgrade is equipped with around 70 diagnostics. The two most important ones for this work are electron cyclotron emission measurements (cf. chapter 3) and lithium beam emission spectroscopy (cf. appendix C). Further measured data shown in this thesis were derived from Deuterium CyaNide interferometry (DCN) [100], Thomson Scattering spectroscopy (TS) [101], Langmuir probe measurements [89], Charge eXchange Recombination Spectroscopy (CXRS) [102] and Doppler reflectometry [103].

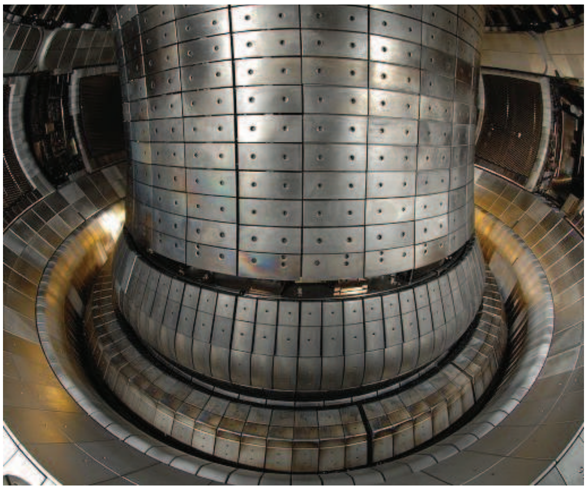

Figure A.2: Inside view of the vacuum vessel of ASDEX Upgrade [96].

From interferometry diagnostics one can obtain the line-integrated density [104]. A millimetre wave laser beam that crosses the plasma experiences a phase shift with respect to a reference beam of the same geometrical path length in vacuum due to the different refractive indices of both media. The refractive index of the plasma depends on the plasma density. TS measurements also exploit the interaction of the plasma with a laser beam [105]. From the intensity and the Doppler shift of the measured radiation spectrum of the laser light scattered at the electrons, one can derive the electron density and temperature, respectively.

Langmuir probes [106] are electric probes which attract ions and/or electrons and, therefore, experience an electric current that depends on the applied potential. From current-potential characteristic one can deduce the electron temperature, density and plasma potential. CXRS measurements [107] rely on the charge exchange reaction of neutral atoms injected by the NBI with impurity ions. After neutralization, the latter can emit radiation via de-excitation processes. The emission spectrum contains information about the ion density — via its intensity —, the ion temperature — via its width — and the ion velocity — via its Doppler shift. The Doppler reflectometry enables to determine the total radial electric field [108]. It is calculated from the Doppler shift of a back-scattered microwave beam caused by the perpendicular movement of the density perturbation in the cut-off layer. Assuming that the propagation velocity is dominated by the $\vec{E} \times \vec{B}$-drift, the radial electric field amplitude can be derived from the measured velocity and by sweeping the probing frequency a complete profile can be obtained.

B Magnetic perturbation field configuration

The ASDEX Upgrade tokamak has recently been equipped with 16 error field coils for ELM mitigation. Each eight of these saddle coils are installed — toroidally distributed — above and below the outer midplane (silver in Fig. B.1 top). The assembly of eight additional coils at the midplane (red and purple) is planned for the future. The lower panel of Fig. B.1 shows the two existing rows of coils in the $z - \Phi$ plane. The signs for the indicated coil currents correspond to an $n = 2$ MP field with even (same coil current in upper and lower coils) or odd (opposite coil current in upper and lower coils) parity. Positive/negative values of the coil current correspond to an outward/inward directed radial field. Also indicated in this figure are the positions of the LIB ($z = 0.33\,\mathrm{m}$) and the ECE ($z = 0.075\,\mathrm{m}$) diagnostics.

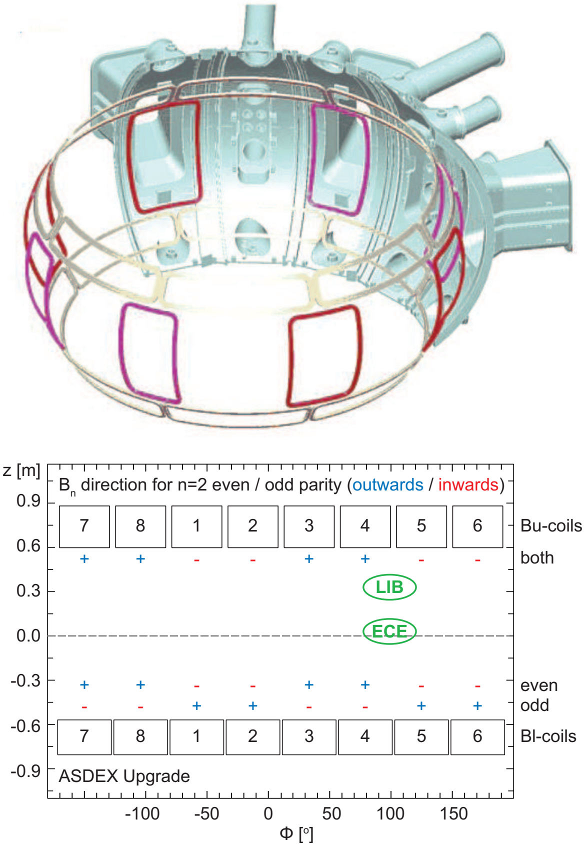

Figure B.1: Setup of the MP-coils at ASDEX Upgrade in a three-dimensional schematic (top) [109] and in the $z - \Phi$ plane with the indicated current configuration for $n = 2$ odd and even (bottom).

With eight toroidally distributed coils it is possible to create non-axisymmetric perturbations fields with toroidal mode numbers $n = 1$ (four neighbouring coils with same coil current polarity), $n = 2$ (two neighbouring coils with same coil current polarity) and $n = 4$ (altering coil current polarity).

With the phase between the upper and lower row the resonant field component can be varied. Resonant MP means that a significant component of the perturbation field is aligned with the equilibrium field lines, i.e. the ratio of poloidal m and toroidal n mode numbers of a resonant component equals the safety factor: $q = m/n$ (cf. left-hand side of Fig. B.2). From the poloidal mode spectrum on the right-hand side of Fig. B.2 it can be seen that it is not possible to achieve fully resonant or fully non-resonant MPs. This is due to the box-like shaping of the MP-coils which always creates broad poloidal spectra [31]. However, the amplitude of the resonant component can be varied by a factor, as shown on the right-hand side of Fig. B.2.

The figure also shows that the amplitude of the Fourier component of the perturbation field at the plasma surface is very small compared to the equilibrium magnetic field

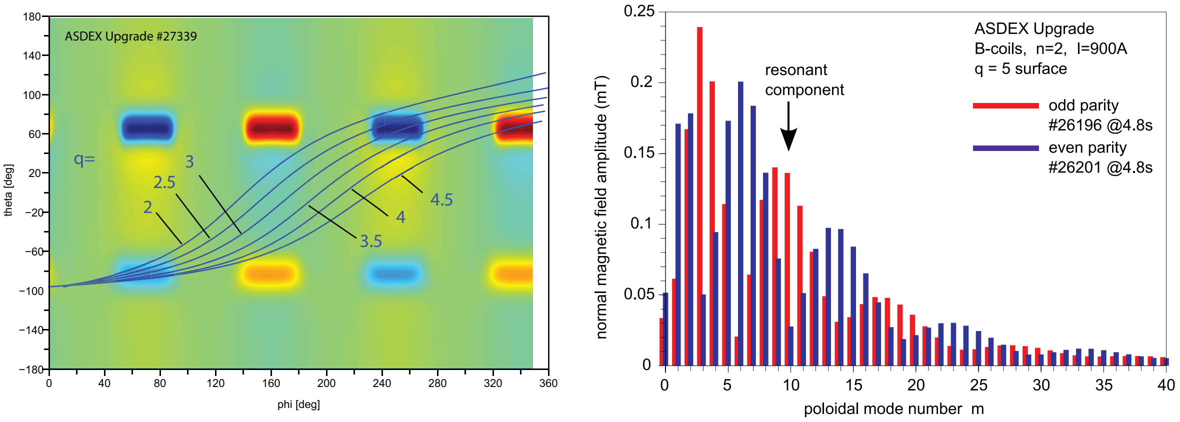

Figure B.2: Left: Alignment of the MP field with the safety factor [110]. Right: MP mode number spectrum [64].

($\approx 10^{-4} B_{\text{tot}}$). The strength of the total radial perturbation field at its maximum in front of a coil is about $B_{\text{MP,r}} \approx 10^{-3} B_{\text{tot}}$.

C Lithium beam emission spectroscopy

The reconstruction of electron density profiles at the edge of a fusion plasma is enabled by the LIthium Beam (LIB) emission spectroscopy diagnostic [23] which is based on measurements of the Li I $(2p \rightarrow 2s)$ line emission of lithium atoms that are injected into the plasma and excited by collisions with plasma particles.

In the plasma, the originally neutral lithium atoms in ground state undergo various processes changing their charge and energetic states. They are excited and ionized by collisions with plasma electrons and ions via impact excitation, ionization and charge exchange. Excited lithium atoms are in turn exposed to spontaneous or collisional de-excitation.

The occupation level of each state i ($i = 1$: Li $(2s)$, $i = 2$: Li $(2p)$, ...) of neutral lithium is given by a coupled system of linear differential equations:

$$\frac{\mathrm{d}N_i(z)}{\mathrm{d}z} = \left[n_\mathrm{e}(z)a_{ij}(T_\mathrm{e}(z), Z_\mathrm{eff}(z)) + b_{ij}\right] N_j(z) \tag{C.1}$$

which depend on the electron density and temperature and the effective ion charge Z_eff at the LIB coordinate z and the Einstein coefficients which contain all collisional a_{ij} and spontaneous b_{ij} processes. As boundary condition, all atoms have to be in ground state at the plasma entrance ($N_i(z = 0) = \delta_{1i}$). The intensity of the measured Li I $(2p \rightarrow 2s)$ resonance line at 670.8 nm is directly proportional to the occupational level $N_2(z)$ of the first excited $2p$ state.

The reconstruction of the density profile from the Li I $(2p \rightarrow 2s)$ emission profile is done via forward modelling within the framework of IDA [82]. The equations system (C.1) is solved for $i = 1, .., 9$ with parameterized profiles for electron density and temperature and tabulated Einstein coefficients. Comparison of the modelled and measured intensities of the $2p$ state within the Likelihood (cf. section 3.4 and [82]) together with additional prior information delivers the parameter values for the electron density profile which is most likely to cause the measured emission profile.

The setup of the LIB diagnostic at ASDEX Upgrade [111] is shown in Fig. C.1. It is equipped with a source (right-hand side in Fig. C.1) which provides beam energies between $30 - 80$ keV and two optical heads observing the beam from two different positions (IXS and CXS in Fig. C.1). The beam energy allows for measurements up to the H-mode pedestal top, where the beam is attenuated almost completely.

The optical system used for density profile measurements (IXS) exhibits a spatial resolution of 5 mm and a temporal resolution of 50 μs. The beam is chopped in order to distinguish between the active signal from Li I line emission and the passive background which is mainly caused by bremsstrahlung. This is done by modulating either the deflection voltage which misaligns the beam aside the optics or the extraction voltage to

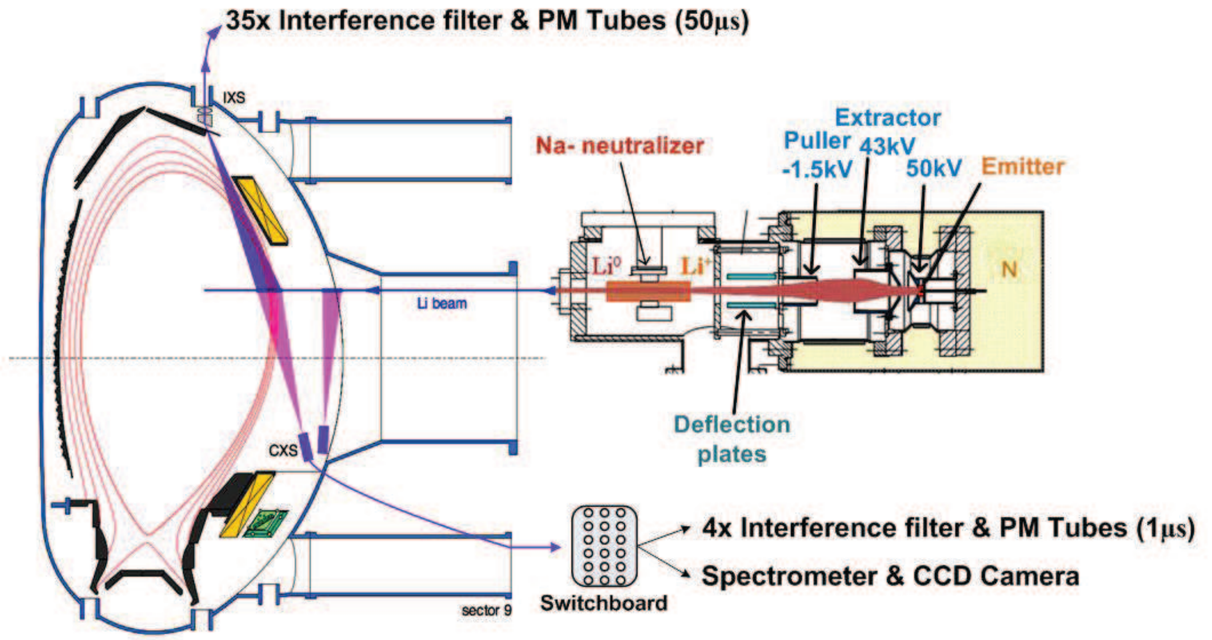

Figure C.1: Experimental setup of the LIB diagnostic at ASDEX Upgrade [111].

suppress the beam. The averaged beam-off (usually 24 ms) signal is then subtracted from the beam-on (usually 56 ms) signal.

D Calculation of the emission shape function

The integration of the emission profile along the ECE LOS is the central part within the ECFM analysis. Since it has to be calculated 10^5 times for one single forward modelling (cf. section 3.4), the numerical calculation of the shape function according to (3.9) is not acceptable. In the following, the derivation of a new analytical formula for the shape function of the emission profile is sketched.

$$\begin{aligned}
\Phi(\omega) &= \frac{\zeta^{7/2}}{\sqrt{\pi}} \int_{-1}^{1} \mathrm{d}\beta_\parallel \int_0^{\sqrt{1-\beta_\parallel}} \mathrm{d}\beta_\perp \beta_\perp^5 \delta\left(\left[1-\beta_\parallel\cos\theta\right]\omega - \frac{\omega_{2\mathrm{X}}}{\gamma}\right) \times \exp\left(-\zeta\left[\beta_\perp^2+\beta_\parallel^2\right]\right) \\
&\underbrace{=}_{\mathrm{I}} \frac{\zeta^{7/2}\omega}{\sqrt{\pi}\omega_{2\mathrm{X}}^2} \int_{\beta_{\parallel,1}}^{\beta_{\parallel,2}} \mathrm{d}\beta_\parallel \left(1-\beta_\parallel^2-\left[1-\beta_\parallel\cos\theta\right]^2\mu\right)^2 \left(1-\beta_\parallel\cos\theta\right) \\
&\qquad \times \exp\left(-\zeta\left[1-\left\{1-\beta_\parallel\cos\theta\right\}^2\mu\right]\right) \\
&\underbrace{=}_{\mathrm{II}} \frac{\zeta^{7/2}\omega}{2\sqrt{\pi}\omega_{2\mathrm{X}}^2\cos\theta} \int_{\alpha_2}^{\alpha_1} \mathrm{d}\alpha \left(1-\left[\frac{1-\sqrt{\alpha}}{\cos\theta}\right]^2-\alpha\mu\right) \exp\left(-\zeta\left[1-\mu\alpha\right]\right) \\
&= \ldots = \\
&= \frac{\zeta^{7/2}\omega}{2\sqrt{\pi}\omega_{2\mathrm{X}}^2\cos^5\theta} \int_{\alpha_2}^{\alpha_1} \mathrm{d}\alpha \left(\sin^4\theta - 4\sqrt{\alpha}\sin^2\theta + 2\alpha\left[2+\eta\sin^2\theta\right] - 4\eta\alpha^{3/2} + \eta^2\alpha^2\right) \\
&\qquad \times \exp\left(-\zeta\left[1-\mu\alpha\right]\right) \\
&\underbrace{=}_{\mathrm{III}} \frac{\zeta^{7/2}\omega}{2\sqrt{\pi}\omega_{2\mathrm{X}}^2\cos^5\theta} \epsilon[\exp\left(-\zeta\left\{1-\mu\alpha\right\}\right)(\sin^4\theta + 2\epsilon\left\{\eta\sin^2\theta+2\right\}\left\{\frac{\alpha}{\epsilon}-1\right\} \\
&+\eta^2\left\{\alpha-2\alpha\epsilon+2\epsilon^2\right\} - 4\eta\alpha^{3/2} + 4\sqrt{\alpha}\left\{\frac{3}{2}\eta\epsilon-\sin^2\theta\right\} - 4\sqrt{\epsilon}\left\{\frac{3}{2}\eta\epsilon-\sin^2\theta\right\} F\left(\sqrt{\frac{\alpha}{\epsilon}}\right))]_{\alpha_2}^{\alpha_1} \\
&\underbrace{=}_{\mathrm{IV}} \frac{\zeta^{3/2}}{\sqrt{\pi}\omega\mu\cos^5\theta} \\
&\times \left[\exp\left(-\zeta\left\{1-\mu\alpha\right\}\right)\left(-\frac{\sin^2\theta}{\sqrt{\alpha}} + \frac{\eta^2}{\zeta\mu} - \frac{1}{\sqrt{\zeta\mu}}\left\{3\eta-2\zeta\mu\sin^2\theta\right\} F\left(\sqrt{\zeta\mu\alpha}\right)\right)\right]_{\alpha_2}^{\alpha_1}
\end{aligned} \tag{D.1}$$

with substitutes: $\mu = \omega^2/\omega_{2\mathrm{X}}^2$, $\eta = 1+\mu\cos^2\theta$, $\epsilon = (\zeta\mu)^{-1}$

I: Integral over $\beta_\perp$

$$\int_a^b f(x)\delta(g(x))dx = \sum_i \int_a^b f(x)\frac{\delta(x-x_i)}{|g'(x_i)|}\mathrm{d}x = \sum_i \frac{f(x_i)}{|g'(x_i)|}, \text{where } i \text{ are the roots in } [a,b]$$

$$\beta_{\|,1/2} = \left(\mu\cos(\theta) \mp \sqrt{1-\mu\sin^2\theta}\right)\left(1+\mu\cos^2\theta\right)^{-1}$$

II: substitution

$$\alpha = \left(1-\beta_\|\cos\theta\right)^2 \Rightarrow \mathrm{d}\beta_\|/\mathrm{d}\alpha = -\left(2\sqrt{\alpha}\cos\theta\right)^{-1}$$

III: Dawson integral F

$$\int_{x_1}^{x_2}\mathrm{d}x x^{3/2}e^x = \left[x^{3/2}e^x\right]_{x_1}^{x_2} - 3/2\int_{x_1}^{x_2}\mathrm{d}x\sqrt{x}e^x = \left[\left(\sqrt{x}-F(\sqrt{x})e^x\right)\right]_{x_1}^{x_2}$$

IV: only higher orders in ϵ
$\epsilon^0 = 0$
$\cos^2\theta = (1-\sqrt{\alpha})^2/(1-\mu\alpha)$ (follows from $\epsilon^0 = 0$)

E List of abbreviations

CXRS Charge eXchange Recombination Spectroscopy

DCN Deuterium CyaNide interferometry

ECE Electron Cyclotron Emission

ECFM Electron Cyclotron radiation Forward Modelling

ECRH Electron Cyclotron Resonance Heating

ELM Edge Localized Mode

ETB Edge Transport Barrier

H-mode High confinement mode

ICRH Ion Cyclotron Resonance Heating

IDA Integrated Data Analysis

I-phase Intermediate phase

LIB LIthium Beam emission spectroscopy

L-mode Low confinement mode

LOS Lines Of Sight

MP Magnetic Perturbation

NBI Neutral Beam Injection

REF REFlectometry

SOL Scrape-Off Layer

TS Thomson Scattering spectroscopy

References

[1] International Energy Agency. Fusion Power Position Paper. Website, 2011. Online at http://www.iea.org/publications/freepublications/publication/name,3710,en.html; visited at 25th January 2013.

[2] International Energy Agency. World Energy Outlook. Website, 2011. Online at http://www.iea.org/publications/freepublications/publication/name,20549,en.html; visited at 25th January 2013.

[3] International Energy Agency. Energy Technology Perspectives 2012. Website, 2011. Online at http://www.iea.org/publications/freepublications/publication/name,27685,en.html; visited at 25th January 2013.

[4] Christina Steinlein. 20 Jahre Kernfusion — Mit Zuversicht ins Ungewisse. Website, 2011. Online at http://www.focus.de/wissen/technik/erfindungen/20-jahre-kernfusion-mit-zuversicht-ins-ungewisse_aid_682651.html; visited at 7th January 2013.

[5] Dux R. Plasmaphysik und Fusionsforschung: Teil II: Fusionsforschung, 2002. Vorlesungsskript.

[6] Keilhacker M and the ASDEX Team. The ASDEX divertor tokamak. Nucl. Fusion, **25**(9), 1985.

[7] Wagner F *et al.* Regime of Improved Confinement and High Beta in Neutral-Beam-Heated Divertor Discharges of the ASDEX Tokamak. Phys. Rev. Lett., **49**(19):1408–12, 1982.

[8] Wagner F. A quarter-century of H-mode studies. Plasma Phys. Control. Fusion, **49**:B1–33, 2007.

[9] Ryter F *et al.* Experimental studies of electron transport. Plasma Phys. Control. Fusion, **43**:A323–38, 2001.

[10] Zohm H. Edge localized modes (ELMs). Plasma Phys. Control. Fusion, **38**:105–28, 1996.

[11] Wilson H R, Connor J W, Field A R, Fielding S J, Miller R L, Lao L L, Ferron J R, and Turnbull A D. Ideal magnetohydrodynamic stability of the tokamak high-confinement edge region. Physics of Plasmas, **5**(5):1925–34, 1999.

[12] Loarte A *et al.* Characteristics of type I ELM energy and particles losses in existing devices and their extrapolation to ITER. Plasma Phys. Control. Fusion, **45**:1549–69, 2003.

[13] Leonard A W *el al.* Tolerable ELMs in Conventional and Advanced Scenarios at ASDEX Upgrade. J. Nucl. Mater., **266–269**:109–17, 1999.

[14] Hender T C *et al.* Effect of resonant magnetic perturbations on COMPASS-C tokamak discharges. Nucl. Fusion, **32**(12):2091–117, 1992.

[15] Miura Y *et al.* Studies of improved confinement on JFT-2M. In 13th International Conference on Plasma Physics and Controlled Nuclear Fusion Research (Washington, USA), volume **1**, pages 325–33, 1991.

[16] Evans T E *et al.* Suppression of large edge-localized modes in high-confinement DIII-D plasmas with a stochastic magnetic boundary. Phys. Rev. Lett., **92**(23):235003(4pp), 2004.

[17] Suttrop W *et al.* Studies of edge localized mode mitigation with new active in-vessel saddle coils in ASDEX Upgrade. Plasma Phys. Control. Fusion, **53**:124014(8pp), 2011.

[18] Kirk A *et al.* Magnetic perturbation experiments on MAST L and Hmode plasmas using internal coils. Plasma Phys. Control. Fusion, **53**(6):065011(18pp), 2011.

[19] Gohil P *et al.* L-H transition studies on DIII-D to determine H-mode access for operational scenarios in ITER. Nucl. Fusion, **51**(10):103020(9pp), 2011.

[20] Kaye S M *et al.* L-H threshold studies in NSTX. Nucl. Fusion, **51**(11):113019(10pp), 2011.

[21] Ryter F *et al.* L-H transition in the presence of magnetic perturbation in ASDEX Upgrade. Nucl. Fusion, **52**(11):114014(7pp), 2012.

[22] Luhmann N C Jr, Bindsley H, Park H, Sánchez J, Taylor G, and Yu C X. Microwave diagnostics. Fusion Sci. Technol., **53**:335–96, 2008.

[23] Schweinzer J, Wolfrum E, Aumayr F, Pöckl M, Winter H, Schorn R P, Hintz E, and Uterreiter A. Reconstruction of plasma edge density profiles from LiI(2s-2p) emission profiles. Plasma Phys. Control. Fusion, **34**(7):1173(11pp), 1992.

[24] Fischer R, Fuchs C J, Kurzan B, Suttrop W, Wolfrum E, and the ASDEX Upgrade Team. Integrated Data Analysis of profile diagnostics at ASDEX Upgrade. Fusion Sci. Technol., **58**(2):675–84, 2010.

[25] Hartfuss H J, Geist T, and Hirsch M. Heterodyne methods in millimetre wave plasma diagnostics with applications to ECE, interferometry and reflectometry. Plasma Phys. Control. Fusion, **39**:1693–769, 1997.

[26] Peeters A G, Suttrop W, and the ASDEX Upgrade Team. Nonthermal ECE at the plasma edge during the H-mode. In 10th Joint Workshop on Electron Cyclotron Emission and Electron Cyclotron Resonance Heating (Ameland, Netherlands), pages 403–10, 1997.

[27] de la Luna E, Sánchez J, Tribaldos V, and JET-EFDA contributors. Electron cyclotron emission radiometer upgrade on the Joint European Torus (JET) tokamak. Rev. Sci. Instrum., **75**(10):3831–3, 2004.

[28] Wang Z, Lohr J, Bell G L, Hsieh C, Luo J, Stockdale R E, Wilgen J B, and Zhang J. Study of electron temperature profile evolution during L-H transition with measurement of Electron cyclotron emission on DIII-D. In 9th Joint Workshop on Electron Cyclotron Emission and Electron Cyclotron Resonance Heating (Borrego Springs, California), pages GA–A22038, 1995.

[29] Wolfrum E. private communication.

[30] Evans T E *et al.* Suppression of large edge localized modes with edge resonant magnetic fields in high confinement DIII-D plasmas. Nucl. Fusion, **45**:595–607, 2005.

[31] Suttrop W *et al.* Mitigation of Edge Localized Modes with small non-axisymmetric magnetic perturbations in ASDEX Upgrade. submitted to IAEA.

[32] Wagner F *et al.* Development of an Edge Transport Barrier at the H-Mode Transition of ASDEX. Phys. Rev. Lett., **53**(15):1453–6, 1984.

[33] Martin Y R, Takizuka T, and ITPA CDBM H mode Threshold Database Working Group. Power requirement for accessing the H-mode in ITER. J. Phys.: Conf. Ser., **123**:012033(11pp), 2008.

[34] Ryter F *et al.* H-mode power threshold and transition in ASDEX Upgrade. Plasma Phys. Control. Fusion, **40**:725–9, 1998.

[35] Righi E *et al.* Isotope scaling of the H-mode power threshold on JET. Nucl. Fusion, **39**:309–19, 1999.

[36] Ida K. Experimental studies of the physical mechanism determining the radial electric field and its radial structure in a toroidal plasma. Plasma Phys. Control. Fusion, **40**:1429–88, 1998.

[37] Schirmer J. Plasma Turbulence Studies Using Correlation Doppler Reflectometry on the ASDEX Upgrade Tokamak. PhD thesis, Ludwig-Maximilians-Universität München, 2005.

[38] Viezzer E *et al.* High-accuracy characterization of the edge radial electric field at ASDEX Upgrade. 2012. to be published in Nucl. Fusion.

[39] Sauter P *et al.* L- to H-mode transition at low density in ASDEX Upgrade. Nucl. Fusion, **52**:012001(5pp), 2012.

[40] Biglari H, Diamond P H, and Terry P W. Influence of sheared poloidal rotation on edge turbulence. Phys. Fluids, **B2**:165004(4pp), 1990.

[41] Connor J W and Wilson H R. A review of theories of the L-H transition. Plasma Phys. Control. Fusion, **42**:R1–74, 2000.

[42] Manz P, Ramisch M, and Stroth U. Physical Mechanism behind Zonal-Flow Generation in Drift-Wave Turbulence. Phys. Rev Lett., **103**:165004(4pp), 2009.

[43] Estrada T, Happel T, Hidalgo C, Ascasíbar E, and Blanco E. Experimental observation of coupling between turbulence and sheared flows during L-H transitions in a toroidal plasma. Europhysics Letters, **92**(3):35001(6pp), 2010.

[44] Conway G D, Angioni C, Ryter F, Sauter P, Vicente J, and ASDEX Upgrade Team. Mean and Oscillating Plasma Flows and Turbulence Interactions across the L-H Confinement Transition. Phys. Rev Lett., **106**:065001(4pp), 2011.

[45] Greenwald M, Terry J L, Wolfe S M, Ejima S, Bell M G, Kaye S M, and Neilson G H. A new look in density limits in tokamaks. Nucl. Fusion, **28**(12):2199(10pp), 1988.

[46] Chirikov B V. A universal instability of many-dimensional oscillator systems. Physics Reports, **52**(5):263–379, 1979.

[47] Dux R, Neu R, Peeters A G, Pereverzev G, Mück A, Ryter F, Stober J, and the ASDEX Upgrade Team. Influence of the heating profile on impurity transport in ASDEX Upgrade. Europhysics Letters, **45**(9):1815–25, 2003.

[48] Suttrop W. The physics of large and small edge localized modes. Plasma Phys. Control. Fusion, **42**:A1–14, 2000.

[49] Wolfrum E *et al.* Characterization of edge profiles and fluctuations in discharges with type-II and nitrogen-mitigated edge localized modes in ASDEX Upgrade. Plasma Phys. Control. Fusion, **53**(8):085026(16pp), 2011.

[50] Kass T, Günter S, Maraschek M, Suttrop W, Zohm H, and the ASDEX Upgrade Team. Characteristics of type I and type III ELM precursors in ASDEX Upgrade. Nucl. Fusion, **38**(1):111–6, 1998.

[51] Federici G, Loarte A, and Strohmayer G. Assessment of erosion of the ITER divertor targets during type I ELMs. Plasma Phys. Control. Fusion, **45**:1523–47, 2003.

[52] Gruber O *et al.* The impact of ELMs on the ITER divertor. In 19th IAEA Conference on Fusion Energy (Lyon, France), volume **EX/C2-1**, 2002.

[53] Suttrop W. Studies of the 'Quiescent H-mode' regime in ASDEX Upgrade and JET. Nucl. Fusion, **45**(7):721–30, 2005.

[54] Urano H, Suttrop W, Lang P T, Horton L D, Herrmann A, and the ASDEX Upgrade Team. Fully pellet-controlled ELMs sustaining identical pedestal conditions of natural ELMy H-mode in ASDEX Upgrade. Plasma Phys. Control. Fusion, **46**:A315–21, 2004.

[55] Suttrop W *et al.* Identification of plasma-edge-related operational regime boundaries and the effect of edge instability on confinement in ASDEX Upgrade. Plasma Phys. Control. Fusion, **39**(12):2051–66, 1997.

[56] Suttrop W, Mertens V, Murmann H, Neuhauser J, Schweinzer J, and the ASDEX Upgrade Team. Operational limits for high edge density H-mode tokamak operation. J. Nucl. Mater., **266–269**:118–23, 1999.

[57] Bernstein I B, Frieman E A, Kruskal M D, and Kulsrud R M. An energy principle for hydromagnetic stability problems. In Proceedings of the Royal Society of London. Series A, Mathematical and Physical Sciences, volume **244**, pages 17–40, 1958.

[58] Laval G, Maschke E K, and Pellat R. Ballooning modes in axisymmetric toroidal configurations. Phys. Rev. Lett., **24**:1229–32, 1970.

[59] Connor J W. Edge-localized modes — physics and theory. Plasma Phys. Control. Fusion, **40**:531–42, 1998.

[60] Lortz D. The general "peeling" instability. Nucl. Fusion, **15**:40–54, 1975.

[61] Peeters A G. The bootstrap current and its consequences. Plasma Phys. Control. Fusion, **42**:B231–42, 2000.

[62] Burckhart A, Wolfrum E, Fischer R, Lackner K, Zohm H, and the ASDEX Upgrade Team. Inter-ELM behaviour of the electron density and temperature pedestal in ASDEX Upgrade. Plasma Phys. Control. Fusion, **52**(10):105010(19pp), 2010.

[63] Connor J W. A review of models for ELMs. Plasma Phys. Control. Fusion, **40**:191–213, 1998.

[64] Suttrop W *et al.* First observation of edge localized mode mitigation with resonant and nonresonant magnetic perturbation in ASDEX Upgrade. Phys. Rev. Lett., **106**(23):225004(4pp), 2011.

[65] Fischer R, Fuchs C J, McDermott R, Rathgeber S K, Suttrop W, Willensdorfer M, Wolfrum E, and the ASDEX Upgrade Team. Spatiotemporal response of plasma edge density and temperature to non-axisymmetric magnetic perturbations at ASDEX Upgrade. Plasma Phys. Control. Fusion, **54**(11):115008(12pp), 2012.

[66] Evans T E *et al.* RMP ELM suppression in DIII-D plasmas with ITER similar shapes and collisionalities. Nucl. Fusion, **48**:024002(10pp), 2008.

[67] Evans T E *et al.* Edge stability and transport control with resonant magnetic perturbations in collisionless tokamak plasmas. Nature Physics, **2**:419–23, 2006.

[68] Liang Y *et al.* Active Control of Type-I Edge-Localized Modes with n=1 Perturbation Fields in the JET Tokamak. Phys. Rev. Lett., **98**(26):265004(5pp), 2007.

[69] Liang Y *et al.* Active control of type-I edge localized modes with n = 1 and n = 2 fields on JET. Nucl. Fusion, **50**:025013(11pp), 2010.

[70] Canik J M *et al.* Progress in the development of ELM pace-making with non-axisymmetric magnetic perturbations in NSTX. Nucl. Fusion, **50**:064016(7pp), 2010.

[71] Bécoulet M *et al.* Screening of resonant magnetic perturbations by flows in tokamaks. Nucl. Fusion, **52**(5):54003(16pp), 2012.

[72] Lunt T *et al.* First EMC3-Eirene simulations of the edge magnetic perturbations at ASDEX Upgrade compared to the experiment. Nucl. Fusion, **52**(5):054013(7pp), 2012.

[73] Potzel S, Wischmeier M, Bernert M, Müller H W, Scarabosio A, and the ASDEX Upgrade Team. O-33 chracterization of the fluctuating detachment state in ASDEX Upgrade. to be published in J. Nucl. Mater.

[74] Hutchinson I H. Principles of Plasma Diagnostics. Cambridge University Press, 1987.

[75] Gurnett D A and Bhattacharjee A. Introduction to plasma physics. Cambridge University Press, 2005.

[76] Pitcher C S *et al.* Heat transport at the boundary of ASDEX Upgrade. Plasma Phys. Control. Fusion, **39**(7):1129–44, 1997.

[77] Suttrop W. private communication.

[78] Fischer R, Dinklage A, and Pasch E. Bayesian modelling of fusion diagnostics. Plasma Phys. Control. Fusion, **75**:1095–111, 2003.

[79] Dinklage A, Fischer R, and Svensson J. Bayesian Methods for Integrated Data Analysis. In International Conference on Research and Applications of Plasmas (Warsaw, Poland), page I1.1, 2003.

[80] Fischer R, Burckhart A, Hicks N, Kurzan B, Wolfrum E, and ASDEX Upgrade Team. Multiple diagnostic data analysis of density and temperature profiles in ASDEX Upgrade. In 36th EPS Conference on Plasma Physics (Sofia, Bulgaria), volume **33 E**, page P1.159, 2009.

[81] Dose V and von der Linden W. Outlier Tolerant Parameter Estimation. In Maximum Entropy and Bayesian Methods (Garching, Germany), pages 46–56, 1999.

[82] Fischer R, Wolfrum E, Schweinzer J, and the ASDEX Upgrade Team. Probalistic lithium beam data analysis. Plasma Phys. Control. Fusion, **50**(8):085009(26pp), 2008.

[83] Metropolis N and Ulam S. The Monte Carlo Methods. Journal of the American Statistical Association, **44**(247):335–41, 1949.

[84] Hastings K W. Monte Carlo Sampling Methods Using Markov Chains and Their Applications. Biometrika, **57**(1):97–109, 1970.

[85] Schneider P A *et al.* Differences in H-mode pedestal width of temperature and density. Plasma Phys. Control. Fusion, **54**(10):105009(19pp), 2012.

[86] Neuhauser J *et al.* Transport into and across the scrape-off layer in the ASDEX Upgrade divertor tokamak. Plasma Phys. Control. Fusion, **44**:855–69, 2002.

[87] Eich T, Sieglin B, Scarabosio A, Fundamenski W, Goldston R J, Herrmann A, and the ASDEX Upgrade Team. Inter-ELM Power Decay Length for JET and ASDEX Upgrade: Measurement and Comparison with Heuristic Drift-Based Model. Phys. Rev. Lett., **107**:215001(4pp), 2011.

[88] Stangeby P C, Canik J M, and Whyte D G. The relation between upstream density and temperature widths in the scrape-off layer and the power width in an attached divertor. Nucl. Fusion, **50**(12):125003(12pp), 2010.

[89] Nold B, Conway G D, Happel T, Müller H W, Ramisch M, Rohde V, Stroth U, and the ASDEX Upgrade Team. Generation of blobs and holes in the edge of the ASDEX Upgrade tokamak. Plasma Phys. Control. Fusion, **52**:065005(12pp), 2010.

[90] Barrera L *et al.* Inboard and outboard electron temperature profile measurements in JET using ECE diagnostic. Plasma Phys. Control. Fusion, **52**:085010(14pp), 2010.

[91] Fischer R *et al.* Effect of non-axisymmetric magnetic perturbations on profiles at ASDEX Upgrade. In 38th EPS Conference on Plasma Physics (Strasbourg, France), volume **35G**, page P1.072, 2011.

[92] Ferraro N M, Jardin S C, and Snyder P B. Ideal and resistive edge stability calculations with M3D-C. Physics of Plasmas, **17**(10):102508(10pp), 2010.

[93] Boom J. Characterization of edge localized modes in tokamak plasmas. PhD thesis, Technische Universiteit Eindhoven, 2012.

[94] Gohil P, Burrell K H, and Carlstrom T N. Parametric dependence of the edge radial electric field in the DIII-D tokamak. Nucl. Fusion, **38**(1):93(10pp), 1998.

[95] ASDEX Upgrade Team. ASDEX Upgrade — Machine Parameters. Website, 2012. Online at https://www.aug.ipp.mpg.de/wwwaug/documentation/physics/techdata.shtml; visited at 5th December 2012.

[96] ASDEX Upgrade Team. ASDEX Upgrade — Drawing and Picture Gallery. Website, 2012. Online at https://www.aug.ipp.mpg.de/wwwaug/; visited at 5th December 2012.

[97] Herrmann A and Gruber O. ASDEX Upgrade — Introduction and Overview. Fusion Sci. Technol., **44**(3):569–77, 2003.

[98] Neu R *et al.* Plasma wall interaction and its implication in an all tungsten divertor tokamak. Plasma Phys. Control. Fusion, **49**(12):B59–70, 2007.

[99] Kallenbach A *et al.* ASDEX Upgrade results and future plans. In 24th Symposium on Fusion Engineering (Chicago, USA), volume **SPL5**, pages 1–8, 2011.

[100] Mlynek A, Schramm G, Eixenberger H, Sips G, McCormick K, Zilker M, and Behler K Eheberg J. Design of a digital multiradian phase detector and its application in fusion plasma interferometry. Rev. Sci. Instrum., **81**(3):033507(5pp), 2010.

[101] Kurzan B and Murmann H D. Edge and core Thomson scattering systems and their calibration on the ASDEX Upgrade tokamak. Rev. Sci. Instrum., **82**(10):103501(6pp), 2011.

[102] Viezzer E, Pütterich T, Dux R, McDermott R M, and ASDEX Upgrade Team. High-resolution charge exchange measurements at ASDEX Upgrade. Rev. Sci. Instrum., **83**(10):103501(11pp), 2012.

[103] Happel T, Estrada T, Conway G D, Blanco E, the TJ-II, and ASDEX Upgrade Teams. Scale-resolved Turbulence Studies in L- and H-mode Plasmas of TJ-II and ASDEX Upgrade. In 37th EPS Conference on Plasma Physics (Dublin, Ireland), volume **34A**, page P1.1039, 2010.

[104] Wesson J. Tokamaks. Oxford University Press, 1997.

[105] Murmann H, Götsch S, Röhr H, Salzmann H, and Steuer K H. The Thomson scattering systems of the ASDEX Upgrade tokamak. Rev. Sci. Instrum., **63**(10):4941(3pp), 1992.

[106] Lasnier C J *et al.* First wall and operational diagnostics. Fusion Sci. Technol., **53**(2):640–66, 2008.

[107] Isler R C. A Review of Charge-Exchange Spectroscopy and Applications to Fusion Plasmas. Physica Scripta, **35**:650–61, 1987.

[108] Hirsch M, Holzhauer E, Baldzuhn J, Kurzan B, and Scott B. Doppler reflectometry for the investigation of propagating density perturbations. Plasma Phys. Control. Fusion, **43**(12):1641–60, 2001.

[109] Suttrop W *et al.* In-vessel saddle coils for MHD control in ASDEX Upgrade. Fus. Eng. Des., **84**:290–4, 2009.

[110] Suttrop W *et al.* Mitigation of Edge Localized Modes with magnetic perturbations in ASDEX Upgrade. to be published in Fus. Eng. Des.

[111] Willensdorfer M *et al.* Inproved chopping of a lithium beam for plasma edge diagnostics at ASDEX Upgrade. Rev. Sci. Instrum., **83**(2):023501(7pp), 2012.

Danksagung

Vielen Dank an meinen Betreuer Dr. Wolfgang Suttrop für die Begleitung meiner Arbeit, sein reges Interesse an meinen Ergebnissen, seine Bereitwilligkeit mich an seinem umfassenden Fachwissen teilhaben zu lassen und seine gründlichen Korrekturen, die zur Verbesserung meiner Arbeit beigetragen haben.

Ein großes Dankeschön an meinen Professor Dr. Hartmut Zohm, der trotz seiner vielen Doktoranden stets einen sehr guten Einblick in mein Thema und meine Fortschritte hatte, meine Arbeit unabhängig von ihrem Erfolg immer wertgeschätzt hat, auch kritische Punkte konstruktiv angegangen ist und mir damit vorgelebt hat, was eine gute Führungskraft ausmacht.

Mein ganz besonderer Dank gilt Dr. Rainer Fischer: Du hast mich ohne Einschränkung beim schwierigsten, langwierigsten und häufig auch frustrierenden Teil meiner Arbeit, der Vorwärtsmodellierung der ECE Daten, unterstützt. In vermeintlichen Sackgassen hast du mir einen möglichen Weg aufgezeigt und mich mit deiner Begeisterung auch für die kleinsten Erfolge immer motiviert. Es hat Spaß gemacht mit dir zu arbeiten.

Einen sehr herzlichen Dank auch an Dr. Laura Barrera für die angenehme Zusammenarbeit an der ECE, für ihre große Hilfe während des Schreibens der Arbeit und für viele anregende Diskussionen.

Einen lieben Dank möchte ich auch Dr. Francois Ryter aussprechen, der mich in die Untersuchung des L-H Übergangs mit Störspulen und die dazugehörige Experimentplanung einbezogen, mir damit zu guten Ergebnissen verholfen und mir viel beigebracht hat.

Außerdem danke ich Vladimir Vukovic für die gute Zusammenarbeit an der ECE Diagnostik, Matthias Willensdorfer und Dr. Gregor Birkenmeier für die Bereitstellung der Dichteprofile, Dr. Tim Happel und Dr. Garrard Conway für die Messungen des radialen elektrischen Feldes, Dr. Eleonora Viezzer für die Ionentemperaturdaten und Andreas Burckhart für lehrreiche Diskussionen über ELMs.

Natürlich haben auch weitere Mitglieder des ASDEX Upgrade Teams wertvolle Beiträge zu meiner Arbeit geliefert. Neben dieser guten Zusammenarbeit haben mir auch die angenehme Atmosphäre und viele interessante Gepräche, insbesondere mit den Teilnehmern unserer "lunch group", eine schöne Zeit am IPP beschert.

Zu guter Letzt möchte ich mich bei meiner persönlichen Lektorin, meiner Familie und meinen Freunden für ihren Feinschliff am Text, ihr Interesse an meiner Arbeit und ihre Unterstützung bedanken.